LUONG BAO BINH

Dissertation

COMBINED GRAVITY FIELD MODELING FROM SATELLITE GRAVITY AND TERRESTRIAL DATA SOURCES APPLYING MULTI-RESOLUTION ANALYSIS

2011

ACKNOWLEDGEMENTS

First and foremost, I would like to thank my supervisor, Professor Roland Pail, for his help and guidance. Regardless of his busy schedule, every one of my questions was responded to quickly, and it seems that he was always available whenever I needed support.

I would like to thank Professor Norbert Kuehtreiber whose critical comments help me to improve my thesis as well as change my thought.

I acknowledge the Austrian Exchange Service (OeAD) whose scholarship gave me an opportunity to study in Austria. I also wish to acknowledge Professor Fritz Brunner who taught me the first lessons in Austria.

I cordially acknowledge my colleagues who shared the room with me. They were always ready to help and gave me a friendly atmosphere when I lived in a different culture.

I wish to thank Grete Shelling for her help with proof-reading. Despite the generation gap, she is my real friend in Graz.

Last but not least, this thesis would not be completed without the encouragement from my wife and my parents. Especially, the good-humored laughter of my little boy kept me going during dispirited moments.

Luong Bao Binh

ABSTRACT

In this thesis, a combination scheme in the scene of the MRA (multi-resolution analysis) process is developed for a combined gravity field model. Based on the spherical wavelets and MRA principles, the local (terrestrial) and global (satellite gravity) data are combined using the spectral-stochastic weighting scheme for a regional geoid solution. This weighting scheme, on the one hand, ensures an appropriate contribution of the global and local data in different frequency ranges, and on the other hand, takes all stochastic information of input data into account. Beside the weighting method which is the key for a successful combination, other practical issues such as regularization and grid configuration are also concerned. The numerical study is based on high-accuracy terrestrial gravity data in Austria, and satellite data from the GRACE mission. The results show that the MRA process works correctly with real data, but the solutions are limited to decimeter differing from the reference Austrian Geoid 2007. Although having the essential advantage over the classical method least-squares collocation that it can deal with full signals (i.e. non-reduced data), it seems that the MRA process in the present state of this thesis is still not mature enough for a centimeter-accuracy regional geoid solution.

CONTENTS

CHAPTER 1

INTRODUCTION

The earth's gravity field is often represented by the geoid, a surface of equal gravity potential coinciding with the mean surface of the oceans at rest. Information about the geoid provides valuable insight into the earth as a complex dynamic system. Its knowledge offers a fundamental contribution to geodetic and earth-related applications. In geodesy and oceanography, the geoid serves as a height reference surface for describing continental and sea surface topography. Geophysics exploits the geoid as a gravity field representation revealing the distribution of deeper located masses (Torge 2001).

Globally, since the geoid represents a mean sea surface at rest, it is required for all applications that need to determine dynamic sea surface topography from the altimetry measurements. The orbit determination of satellites, particularly for the low-orbit satellites, also requires the accurate gravity field models. Moreover, the global gravity field reflects the internal structure of the Earth, and can help in the exploration for oil and mineral resources.

Locally, geoid determination is the basic geodetic work for the nations. Nowadays, with the more and more popular GPS measurement, the most directly important application is the possibility to transform the geometric heights observed by GPS to the orthometric/normal heights in the national height system. If a high precision geoid is known, the GPS measurement

can more or less replace the traditional leveling measurement, which is an expensive and time-consuming technique with increasing error over long distances.

The terrestrial observables are often collected for comparatively small regions, i.e. the territory of a country. The data distribution is also inhomogeneous with the existence of data gaps due to the terrain, e.g., the inaccessibility of certain areas. Compared to the satellite data, the terrestrial observables are much denser, and a gravity field with much higher resolution can be computed from them. However, as a drawback, the quality at long wavelengths is not as good as the quality of satellite data.

The satellite data are good at long wavelengths, but limited in its spatial resolution. A combination of both data sources is required for the computation of precise high-resolution regional gravity fields.

Nowadays, the terrestrial measurements, the airborne gravimetry, and the recent dedicated satellite gravity missions CHAMP (Challenging Minisatellite Payload, see webpage of GeoForschungsZentrum Potsdam at http://op.gfz-potsdam.de/champ), GRACE (Gravity Recovery and Climate Experiment, Flechtner 2005, Tapley et al. 2004), and GOCE (Gravity and Ocean Circulation Explorer, see ESA 1999 and Drinkwater et al. 2003) provide the gravity data with higher and higher quality and resolution as well as the opportunity for more and more precise geoid determination.

Traditionally, for each kind of data sets (satellite, airborne, terrestrial), the dedicated data processing schemes have been developed using different methods. The optimal combination for different kinds of data requires, at least, a methodology that can be used for any kind of data. Elements of this methodology comprise the estimation principle, the regularization, the data weighting scheme, the error propagation, and other practical configurations.

Generally, the data sets can be classified into the two main sources, the global data and the terrestrial observations. The combination of these two data sources has been achieved by a remove-restore technique using the least-squares collocation (Moritz 1989). Least-squares collocation, known as the standard approach so far, uses the covariance functions as the ker-

nel function; and the proper computation of these values is always the key challenge. Moreover, the remove-restore steps cause unavoidable errors by themselves. Thus there is always room for the development of a new method to overcome the disadvantages of this classical approach.

The use of spherical (radial) base functions in gravity field modeling is not new. Over the years, several attempts have been made. Freeden's group at Kaiserslautern university has investigated spherical base functions and wavelets for a long time, mostly focusing on multi-scale representations (Freeden 1999, Freeden et al. 2003, Freeden et al. 2004, Fengler et al. 2004, Freeden et al. 2009). A general description of the concept of wavelets and their applications in geodesy and geodynamics can be found in literature, for instance in Freeden et al. (1998) and Keller (2004). Spherical wavelets were applied to the analysis of CHAMP data by Fengler et al. (2004) and Schmidt et al. (2005). Fengler et al. (2007) used wavelets for the representation of time variable GRACE gravity fields; they made use of existing global spherical harmonics and applied wavelets to the spherical harmonic coefficients, in this way the spherical harmonic solutions were decomposed into different scales. And lately, Wittwer (2009) used radial basis functions in the parameterization for global and regional models of the mean and time-variable gravity field.

Moreover, Schmidt et al. (2007) also developed an approach and applied it to compute the regional potential field from CHAMP and terrestrial data, as well as the temporal variations from GRACE. The so-called unique reproducing kernel introduced in their paper will be applied in this thesis as a core for the functional model. And in the framework of the GEOnAUT (Austrian Geoid 2007) project, Pail (2006, 2007) has also investigated a local geoid processing method based on wavelets and multi-resolution analysis, from which this thesis inherits several valuable things.

However, no "standard" methodology for data combination has been established so far. So there is still room for innovative attempts to develop an approach for combining different data sources in the scheme of the wavelet process for the geoid determination purpose. It is also the main goal of this thesis.

Based on the principle of spherical wavelets and multi-resolution analysis (MRA) process, a solution for the combined gravity field model will be presented in this thesis. In principle, the application of this MRA process does not require the reductions; consequently we can skip some steps and reduce the data processing effort as well as avoid the errors propagated from them. Furthermore, different types of data sources can be combined thanks to an adequate weighting scheme, and the error estimates of the output model can be totally estimated according to the law of error propagation. Concerning the new aspects, this thesis develops an approach for combining different types of data using the combined spectral-stochastic weighting scheme in the scene of the MRA process and applies it to the real data for a local geoid solution.

It should be noticed that, in this thesis, though based on the multi-resolution analysis concept, the actual process is carried out at one resolution (of the output grid) for the simplicity as well as reducing the computation effort. In principle, the essence of MRA is still guaranteed; and a complete MRA process can possibly be the continuation after this thesis. For convenience and due to the habitual name of MRA, this term is also used in the whole thesis; and please keep in mind the note mentioned above.

The initially intended objective (for the case study) is a geoid solution for Vietnam (my country); however, the deficiency of Vietnamese terrestrial data did not allow doing that. Fortunately, Professor Roland Pail kindly provided the Austrian data; thus the case study result is about the Austrian geoid. This also helps to skip the data pre-processing step due to the given data which was already pre-processed for the previous project (Pail 2007). In addition, the use of the same terrestrial data set gives the chance to check and compare with the official result of that project (GEOnAUT).

With that purpose, the content of the thesis is organized as follow:

- Chapter 1 presents the background of the geoid determination work, the motivation for the wavelets and MRA-derived combination process using spherical base functions, the (restricted) objective and the outline.

- Chapter 2 is pure theoretical. After an overview of the gravity field and gravity data as well as the reference method least-squares collocation (LSC), the functional model is introduced, leads the way to apply the MRA-wavelets principles into the gravity field modeling using spherical base functions. Here the theoretical essence is the unique reproducing kernel (Schmidt et al. 2007), and the practically meaningful point is the scaling coefficient vector. At last, a comparison between LSC and MRA in a theoretical point of view is performed.

- Chapter 3 is concerned with regularization, a practically key issue to overcome the ill-posed problem when estimating parameters (the scaling coefficient vector). Here the Tikhonov regularization, which is simple and sufficient for the gravity potential modeling, is the baseline method. And to answer the question about the choice of regularization parameter which is the essence in Tikhonov regularization, several simulations in the scheme of gravity field modeling using the MRA process will be presented.

- Chapter 4 deals with the grid configuration including two main issues, the type of grid and the grid's resolution. For the former question, once again, the answer is the simplicity, i.e. the equiangular grid is chosen. The resolution depends on the input data, the set-up of the computation scheme, as well as the expected output. Simulations in this chapter will give a practical guidance to a certain degree.

- Chapter 5 is dedicated to the weighting problem which is the key for a successful combination. Concerning the spectral content, where the basic principle is that the long wavelengths are reserved for the global data and the short wavelengths are the domain of local data, the spectral weighting method is introduced. The other way is of using the stochastic information of input data to compute the weighting values. At last, the combination of those two, the so-called spectral-stochastic weighting method is proposed with the expectation that it will be adequate for the MRA process which implies the frequency-based analysis, as well as take the stochastic information of all input data sources into

account.

- Chapter 6 presents the implementation of the MRA process using real data for the case study of an Austrian geoid solution. After the description for the input data, a computation scheme is set up for the later approaches, which includes the choice for the scaling function, the number of levels will be used, regularization method, the set-up for grids and weighting schemes. An overview about the reference solution GEOnAUT is also given. Afterwards, five approaches using different combining schemes are presented. These approaches comprise the use of reduced and non-reduced data, including or excluding the GPS/leveling data as an input data source. This chapter ends with the summary and discussion for all approaches.

- At last, chapter 7 with the summary, conclusion and outlook will finish the content of this thesis.

CHAPTER 2

THEORIES

This chapter presents theories of gravity field models and the method using spherical wavelets and multi-resolution analysis (MRA) to construct a local geoid model. Besides, the classical standard method least-squares collocation are also presented as a reference. Before that, an introduction to the gravity data and gravity reductions is given.

2.1 GRAVITY DATA AND GRAVITY REDUCTIONS

In this section, the first part introduces some most basic surfaces in geodesy acting as the reference surfaces for gravity measurements. Then, the concept of observations in the geoid modeling issue as well as the computational relationship of them is briefly presented. Finally, the steps to refer the observations to the reference surface is given.

2.1.1 Gravity field and gravity data

Earth's surface is represented by the geoid, which is defined as the equal gravity potential surface that most closely approximates the mean sea level. It means that the gravity potential W of any point on the geoid is constant. Meanwhile, the ellipsoid is defined as the equipotential surface of normal gravity ($U = const$), and is considered as the mathematical figure of the

earth. The difference between the actual value W and the normal value U is called the disturbing potential T

$$T(x,y,z) = W(x,y,z) - U(x,y,z) \ . \tag{2.1}$$

Gradients of W and U are vectors of gravity and normal gravity, respectively. In figure 2.1, the gravity vector at P on the geoid in direction n (plumb-line) is denoted by g_P; the normal gravity vector at Q on the ellipsoid in direction n' (ellipsoidal normal) is denoted by γ_Q; Q is the projection of P in direction of the ellipsoidal normal. The difference in direction between two vectors g and γ (the angle made by n' and n) is called the deflection of the vertical, usually divided into two components: the north-south component ξ and the west-east component η. Two components of the deflections of the vertical can be calculated from astronomical coordinates (relate to the plumb-line) and geodetic coordinates (relate to the ellipsoidal normal) according to

$$\begin{aligned} \xi &= \Phi - \varphi \\ \eta &= (\Lambda - \lambda)\cos\varphi \end{aligned} \tag{2.2}$$

where Φ and Λ are astronomical latitude and longitude, φ and λ are geodetic latitude and longitude.

The difference in magnitude between the gravity (measured value g) and the normal gravity (computable value γ) is called the gravity anomaly Δg

$$\Delta g = g_p - \gamma_Q \ . \tag{2.3}$$

Gravity anomaly and the deflection of the vertical are two main types of terrestrial gravity data in the issue of (local) geoid modeling. In addition, the geoid height N (distance QP in figure 2.1) can be directly obtained by a combination of leveling and GPS measurement:

$$N = h - H \tag{2.4}$$

where h is the geodetic height (from GPS measurement) and H is the orthometric height (from leveling).

On a global scale, the gravity field models are usually provided by the fully normalized harmonic coefficients $\overline{C}_{nm}$ and $\overline{S}_{nm}$. The (disturbing) poten-

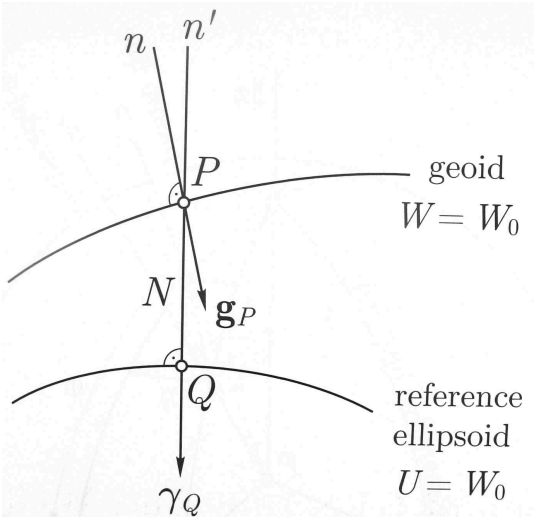

Figure 2.1: Geoid and reference ellipsoid (source: Hofmann-Wellenhof and Moritz 2005)

tial T can be determined in terms of spherical harmonics according to

$$T(r,\theta,\lambda) = \frac{GM}{R}\sum_{n=2}^{n_{max}}\left(\frac{R}{r}\right)^{n+1}\sum_{m=0}^{n}\overline{P}_{nm}(\cos\theta)\left(\overline{C}_{nm}\cos(m\lambda)+\overline{S}_{nm}\sin(m\lambda)\right) \tag{2.5}$$

where r is distance to the earth's center, θ and λ are co-latitude and longitude, respectively, R is the earth's reference radius, GM is the product of gravity constant G and the earth's mass M, n and m are harmonic degree and order, respectively, n_{max} is the maximum degree of the given model, and $\overline{P}_{nm}$ is the normalized Legendre function.

The relationship between the geoid height (also called geoidal undulation) N and the (disturbing) potential T is given by the Bruns formula

$$N_P = \frac{T}{\gamma_Q}\,. \tag{2.6}$$

The conversion between T and N is easily and directly, so the concept of gravity field models (provide T) and geoid models (provide N) can often be used interchangeably.

The relationship between gravity anomaly Δg and the potential T is pro-

vided via equation

$$\Delta g = -\frac{\partial T}{\partial h} + \frac{1}{\gamma}\frac{\partial \gamma}{\partial h} T \ . \tag{2.7}$$

In spherical approximation, equation (2.7) becomes

$$\Delta g = -\frac{\partial T}{\partial r} - \frac{2T}{r} \ . \tag{2.8}$$

For the deflection of the vertical quantities, equation (2.8) can be replaced by

$$\begin{aligned} \xi &= -\frac{1}{\gamma_Q r}\frac{\partial T}{\partial \varphi} \\ \eta &= -\frac{1}{\gamma_Q r \cos\varphi}\frac{\partial T}{\partial \lambda} \ . \end{aligned} \tag{2.9}$$

The most basic measurements and their relationship in the issue of (local) geoid modeling are briefly introduced above. However, these measurements cannot be used directly but require the gravity reduction step which is presenting in the next part.

2.1.2 Gravity reductions

The gravity observations are measured on the terrain surface. For the geoid determination purpose, these values need to refer to see level, so the reductions are required. Generally, the gravity reduction includes two main processes: remove the topographic masses outside the geoid, and lower the gravity stations from the earth's surface to the geoid.

Free-air reduction

In the assumption that there is no mass above the geoid, i.e. the gravity station is "in free air", the difference along the plumb-line between the gravity value at the height H (of the station) and one on geoid can be obtained according to

$$\Delta A = \frac{GM}{(R+H)^2} - \frac{GM}{R^2} \ . \tag{2.10}$$

This quantity is called the free-air reduction F and can be approximated by the Taylor expansion. Keep only the linear term of Taylor's series, equation (2.10) becomes

$$F = GM\left(\frac{1}{R^2} + \frac{-2H}{R^3} - \frac{1}{R^2}\right) = \frac{-2GM}{R^3}H\ . \tag{2.11}$$

Using the parameter values of WGS84, and converting to the unit of mGal, we get

$$F = -0.3086\,H \quad \text{[mGal]} \tag{2.12}$$

for H in meter.

Bouguer reduction

Now we consider the masses between the earth's surface and the geoid. Assume that these masses have a constant density ρ, and the area around the gravity station is completely flat, then the attraction of this so-called Bouguer plate is

$$A_B = 2\pi G\rho H\ . \tag{2.13}$$

With the gravity constant $G = 6.674\ .\ 10^{-11}$ m^3 kg^{-1} s^{-2} and standard density $\rho = 2.67$ g cm^{-3}, it becomes

$$A_B = 0.1119\,H \quad \text{[mGal]} \tag{2.14}$$

for H in meter.

Now applying the free-air reduction given in equation (2.12), the Bouguer gravity on the geoid may be finally obtained by

$$g_B = g - A_B - F\ . \tag{2.15}$$

Terrain correction

Unfortunately, the earth's surface is not completely flat as implied in the Bouguer reduction. Now we take into account the deviation of the actual topography from the Bouguer plate. Exemplarily, at A (figure 2.2), the topographic mass $\Delta m+$ (above the Bouguer plate) attracts P upward causing g

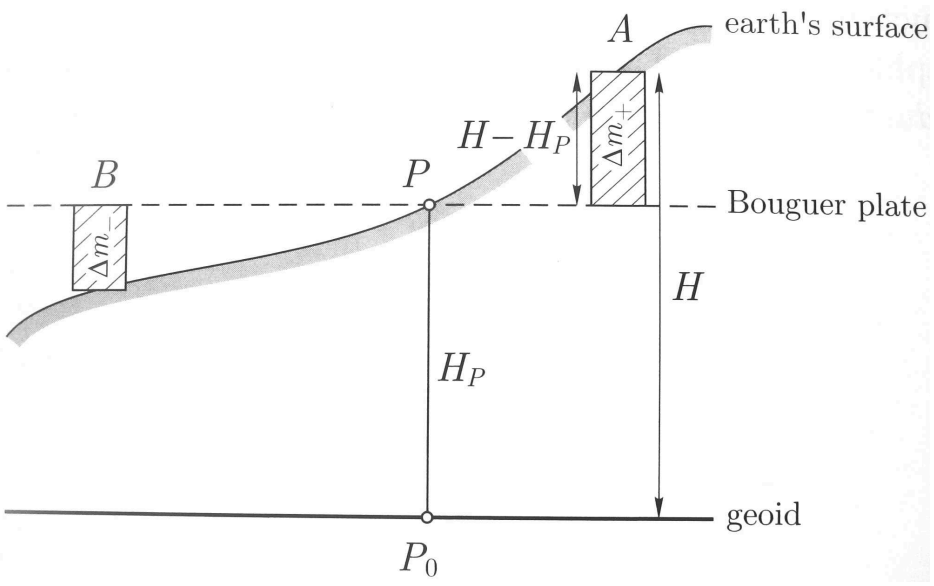

Figure 2.2: Terrain correction (source: Hofmann-Wellenhof and Moritz 2005)

at P to decrease. At B, the topographic mass should be removed, or equivalently, there is the mass $\Delta m-$ with negative value, which attracts P upward again. It means that the terrain always causes the gravity at P to decrease, or in other words, the terrain correction is always negative.

In practical computation, the topographic masses are subdivided into elementary bodies (like $\Delta m+$ and $\Delta m-$) in rectangular prism shape with the constant area ΔS and the height $\overline{h} = |H - H_P|$. By the law of gravitation, the attraction of the elementary body Δm onto P at the distance d can be calculated by

$$\begin{aligned} \Delta A_t &= -\frac{G\Delta m}{d^2}\frac{\overline{h}}{2d} \\ &= -\frac{G\rho}{2d^3}\Delta S\,\overline{h}^2 \,. \end{aligned} \tag{2.16}$$

The terrain correction at P can be obtained by summing the effects of the individual elementary bodies

$$A_t = \sum \Delta A_t \,. \tag{2.17}$$

By adding the terrain correction A_t to (2.15),

$$g_B^{refined} = g - A_B - A_t - F \tag{2.18}$$

called refined Bouguer gravity, is obtained.

It is also possible to compute the total effect of the topographic masses

$$\begin{aligned} A_T &= A_B + A_t \\ &= \sum \Delta A_T \end{aligned} \tag{2.19}$$

in one step by using elementary bodies with bases at sea level, i.e. equation (2.16) becomes

$$\Delta A_T = \frac{G\rho}{d^3}\,\Delta S\, H \left(H_P - \frac{H}{2} \right) . \tag{2.20}$$

Note that the sign of ΔA_T in (2.20) depends on whether H_P is larger or less than $H/2$ instead of being always negative as of ΔA_t in equation (2.16).

Note that the computation for the terrain reduction obviously requires a height model in the given area. A digital terrain model (DTM) can be used for this purpose as well as for the computation of topographic-isostatic reduction.

Topographic-isostatic reduction

With the assumption that the topographic masses are superposed on the homogeneous crust, the residual gravity field quantities after applying reductions would be very small and fluctuate randomly around zero. However, in reality, Bouguer anomalies in mountainous areas are systematically negative and may attain large values. The possible explanation is that the topographic masses are compensated by some kind of mass deficiency under the mountains. Therefore, the total reduction consists not only of the free-air reduction to the geoid and the removal of topography, but also the removal of this compensation effect. For this purpose, the Airy-Heiskanen isostasy model is applied (Hofmann-Wellenhof and Moritz 2005).

The principle of Airy-Heiskanen system is the floating equilibrium. The earth's crust is assumed around 30 km thick (denoted T in figure 2.3) and has the density $\rho_0 = 2.67$ g cm^{-3}. It "floats" on a denser under-layer having the density $\rho_1 = 3.27$ g cm^{-3}. If there exists a mountain with the height H (the

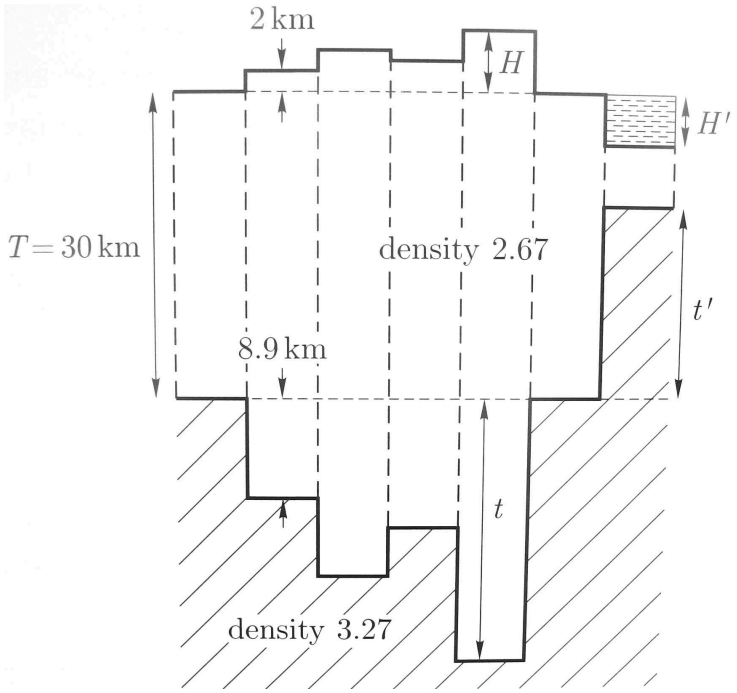

Figure 2.3: Airy-Heiskanen isostasy model (source: Hofmann-Wellenhof and Moritz 2005)

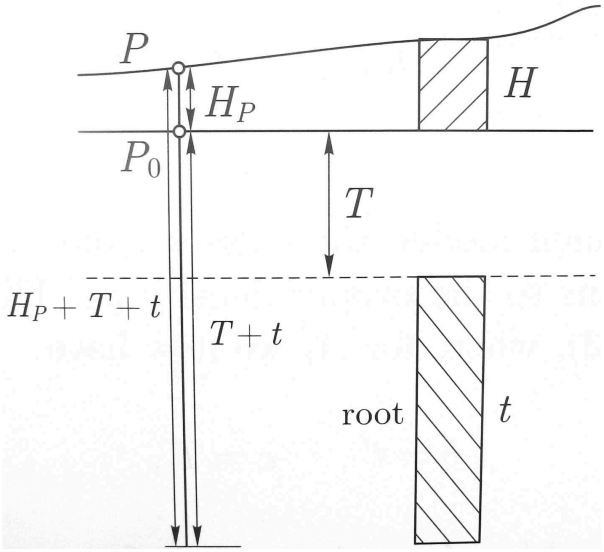

Figure 2.4: Topography and compensation – Airy-Heiskanen isostasy model (source: Hofmann-Wellenhof and Moritz 2005)

density of the mountain is also ρ_0), there should be a "root" of the mountain in the under-layer with the thickness t having the density ρ_0 instead of ρ_1 to compensate for the mass of the mountain. The higher the mountain, the deeper its root; and the relation between H and t satisfies the condition of the floating equilibrium

$$t(\rho_1 - \rho_0) = H\rho_0 \; . \tag{2.21}$$

So that

$$t = \frac{\rho_0}{\rho_1 - \rho_0} H = 4.45\, H \; . \tag{2.22}$$

Under the oceans (with density of sea water $\rho_w = 1.03$ g cm^{-3}), the "anti-roots" have density ρ_1 instead of ρ_0, then the corresponding floating equilibrium equations are

$$t'(\rho_1 - \rho_0) = H'(\rho_0 - \rho_w) \tag{2.23}$$

and

$$t' = \frac{\rho_0 - \rho_w}{\rho_1 - \rho_0} H' = 2.73\, H' \tag{2.24}$$

where H' is the depth of the ocean, t' is the thickness of the anti-root (figure 2.3).

In analogy with equation (2.16), replacing $\overline{h}$ by t, ρ by $\Delta\rho = \rho_1 - \rho_0$ and considering the thickness of the earth's crust $T = 30$ km when computing the distance d, the attraction of the root onto P (figure 2.4) can be calculated by

$$\Delta A_C = -\frac{G\Delta\rho}{d^3}\, \Delta S\, t(H_P + T + \frac{t}{2}) \; . \tag{2.25}$$

The sum of the effects of the individual elementary bodies gives the topographic-isostatic reduction

$$A_C = \sum \Delta A_C \; . \tag{2.26}$$

Adding A_C to equation (2.18) and considering equations (2.19), the topographic-isostatically reduced gravity on the geoid becomes

$$g_{TI} = g - A_T - A_C - F \; . \tag{2.27}$$

The indirect effect

The gravity reductions imply the removal or shifting of masses. This causes the change of the gravity potential and the geoid. The computed surface, called the co-geoid, is slightly different from the geoid. Denoting the undulation at the co-geoid by N^c, the actual undulation N at the geoid is obtained by

$$N = N^c + \delta N \tag{2.28}$$

where δN is the indirect effect on N

$$\delta N = \frac{\delta W}{\gamma} \,. \tag{2.29}$$

In above equation, ∂W is the change of potential on the geoid. In case of topographic-isostatic reduction,

$$\delta W_{TI} = U_T + U_C \,, \tag{2.30}$$

where U_T and U_C are the potentials corresponding to the attractions A_T and A_C in equations (2.19) and (2.26). By the same way as in equations (2.20), (2.19), (2.25) and (2.26), the numerical values of U_T and U_C can be obtained with a reminder that the potential $U = Gm/d$ instead of the attraction $A = Gm/d^2$, and the point U refers to is always P_0 at sea level. Note that exactly the same topographic-isostatic model as for the gravity reductions has to be used to compute U_C.

The indirect effect on gravity δ can be obtained from δN in the similar way of (2.12)

$$\delta = -0.3086\,\delta N \quad \text{[mGal]} \tag{2.31}$$

for δN in meter.

Derived from (2.9), the indirect effect on the deflection of the vertical is given by

$$\begin{aligned} \delta\xi &= -\frac{1}{r}\frac{\partial \delta N}{\partial \varphi} \\ \delta\eta &= -\frac{1}{r\cos\varphi}\frac{\partial \delta N}{\partial \lambda} \,. \end{aligned} \tag{2.32}$$

Free-air anomaly in Molodensky's sense

Conventionally, the gravity anomaly is defined by the difference between the gravity g_P at point P on the geoid and the normal gravity γ_Q at the corresponding point Q on ellipsoid (c.f. section 2.1.1). If we start with the actual gravity g at ground (the measured value), then the free-air anomaly can be obtained by applying the free-air reduction (section 2.1.2)

$$\Delta g^{FA} = g - F - \gamma_Q \, . \tag{2.33}$$

In the sense of Molodensky, instead of reducing the gravity g from ground to geoid, the normal gravity γ_Q is "reduced" from ellipsoid upward to the telluroid. Telluroid is defined as the surface whose normal potential U at every point is equal to the actual potential W at the corresponding point along the ellipsoidal normal. Now (i.e. in the Molodensky's sense), the gravity anomaly is defined as the difference between the measured gravity g on the ground and the normal gravity γ on the telluroid

$$\Delta g = g - \gamma \, . \tag{2.34}$$

The normal gravity γ on the telluroid can be obtained from the normal gravity γ_Q on the ellipsoid by the normal free-air reduction (but upward). For this reason, the gravity anomaly Δg in above equation is also called free-air anomaly. Applying Taylor expansion up to the second order, we get

$$\gamma = \gamma_Q + \frac{\partial \gamma}{\partial h} H^* + \frac{1}{2!} \frac{\partial^2 \gamma}{\partial h^2} H^{*2} \tag{2.35}$$

where h denotes the ellipsoidal height and H^* the normal height (i.e. distance from ellipsoid to telluroid).

In approximation (using only linear term of the flattening f in the first derivative and neglecting f in the second derivative), γ can be obtained by

$$\gamma = \gamma_Q \left[1 - 2(1 + f + m - 2f \sin^2 \varphi) \frac{H^*}{a} + 3 \left(\frac{H^*}{a} \right)^2 \right] \tag{2.36}$$

where φ is latitude of the target point and $m = \omega^2 a^2 b / (GM)$ with conventional parameters of the reference ellipsoid.

In summary, this section introduces the main types of gravity data and the reductions required to compute the geoid. Briefly, the principles of the computational process can be described as follows

- The gravity station is lowered from the ground to the geoid, then the free-air anomalies are computed. In Molodensky's sense, the normal gravity values are "raised" from ellipsoid to telluroid instead of "lowering" the measured gravity values from ground to geoid (equation (2.33) and equation (2.34)).
- The masses outside the geoid are computationally removed or shifted inside the geoid. The presently standard method (for geoid determination purpose) is the topographic-isostatic reduction (equation (2.27)). This step causes the change δN of geoid (equation (2.29)). It is called the indirect effect.
- The indirect effect is computationally excluded from data (equations (2.31) and (2.32)).
- Now the data refer to the co-geoid, being ready for the co-geoid computation. The classical standard method for computation here is least-squares collocation which is introduced in section 2.2.
- After getting the co-geoid, the geoid can be obtained by adding back the indirect effect δN.
- Finally, the inconsistency between the computed geoid and the (national) vertical datum is estimated using a low-order polynomial surface. After this validation step, the final geoid is obtained.

2.2 LEAST-SQUARES COLLOCATION

Least-squares collocation (LSC) is the classical geodetic method for the geoid computation from different gravity data types. It was originally introduced as a prediction and interpolation method, and was then extended to a method for determining the anomalous gravity field by a combination of

geodetic measurements of different types (Hofmann-Wellenhof and Moritz 2005, Moritz 1989). A fundamental role plays the (local or global) covariance function, describing the stochastic properties of the input and output quantities (Tscherning and Rapp 1974).

The expected gravity field output $\hat{s}$ can be estimated from the observation vector l using the basic formula

$$\hat{\boldsymbol{s}} = C_{sl}(C_{ll} + \Sigma)^{-1}\boldsymbol{l} \;, \tag{2.37}$$

where C_{ll} is the covariance matrix describing the statistical properties of the observations $\boldsymbol{l}$, whose measuring accuracy is expressed by the noise matrix Σ, and matrix C_{sl} describes the cross covariances between the observations $\boldsymbol{l}$ and the estimated quantities $\hat{\boldsymbol{s}}$.

One valuable feature of LSC is that the resulting quantities are complemented by their stochastic error estimates. By the covariance propagation, the statistical error estimation of the output $\hat{\boldsymbol{s}}$ can be obtained by

$$\sigma_{\hat{s}}^2 = \sigma_0^2 - C_{sl}(C_{ll} + \Sigma)^{-1}C_{sl}^T \tag{2.38}$$

where σ_0^2 denotes the a-priori variance, and the upper index T denotes the matrix transposition.

In principle, the observation vector $\boldsymbol{l}$ can contain arbitrary types of gravity observations. For example, if gravity observations consist of the gravity anomalies Δg and the deflections of the vertical $\{\xi, \eta\}$, then (2.37) becomes

$$\hat{s} = \begin{bmatrix} C_{s\Delta g} & C_{s\xi} & C_{s\eta} \end{bmatrix} \cdot \begin{bmatrix} C_{\Delta g\Delta g} & C_{\Delta g\xi} & C_{\Delta g\eta} \\ C_{\xi\Delta g} & C_{\xi\xi} & C_{\xi\eta} \\ C_{\eta\Delta g} & C_{\eta\xi} & C_{\eta\eta} \end{bmatrix}^{-1} \cdot \begin{bmatrix} \Delta g \\ \xi \\ \eta \end{bmatrix} \;, \tag{2.39}$$

herein the noise of the observations Δg, ξ, η are included in $C_{\Delta g\Delta g}$, $C_{\xi\xi}$, $C_{\eta\eta}$ implicitly.

The essence in LSC is the determination of covariance matrices. For gravity anomaly quantity which is exemplarily a representative of terrestrial gravity field observations, the element of covariance matrix $C_{\Delta g\Delta g}$ related to two observables Δg_i and Δg_j can be computed by

$$C_{\Delta g_i \Delta g_j} = \mathbf{cov}\left(\Delta g_i, \Delta g_j\right) = \sum_{n=0}^{\infty} c_n \left(\frac{R^2}{r_i r_j}\right)^{n+2} P_n\left(\cos\psi_{ij}\right) \;. \tag{2.40}$$

Here, the covariance depends on the Earth's radius R, the radii from the geocenter of the observables r_i, r_j, the Legendre polynomials P_n, and the spherical distance ψ_{ij} between the observation positions, which can be expressed by

$$\cos\psi_{ij} = \cos\theta_i \cos\theta_j + \sin\theta_i \sin\theta_j \cos(\lambda_i - \lambda_j) \tag{2.41}$$

where θ and λ are co-latitude and longitude, respectively.

The covariance function c_n can be computed using a covariance model, for example the Tscherning-Rapp model (Tscherning and Rapp 1974)

$$c_n = A\frac{n-1}{(n-2)(n+B)} \tag{2.42}$$

with globally or locally adapted parameters A, B. An overview of different global and local covariance models can be found, e.g., in Tscherning and Rapp (1974), Moritz (1989).

In LSC, a fundamental requirement is that the observations $\boldsymbol{l}$ have zero mean: $\mathrm{E}\{\boldsymbol{l}\} = 0$. If the observations contain a deterministic component such as a trend field, it has to be removed beforehand, and to be restored afterwards (the remove-restore technique). In the remove step, the reductions presented in section 2.1 have to be applied to the local gravity data, and additionally they have to be reduced by the global model complete to a specific maximum degree of harmonic expansion before applying LSC.

The trend field and global reductions in LSC, firstly, require the restore afterwards. This process causes an error at a certain degree. Secondly, the long-wavelength components (which are reduced) are not taken into account, i.e., more or less, we miss information of this part in the computation process. The next section will introduce the other method, called multiresolution analysis (MRA), which, in general, does not require the trend field and global reductions. As the result, at least in theory, the more propagated error can be avoided and the more information can be used in the computation process in comparison with LSC.

2.3 Combined gravity field model using spherical wavelets and MRA

The main idea of the multi-resolution analysis (MRA) is the splitting of a signal into a smoothed version and a number of detail signals by successive low-pass filtering. Applying to the gravity field modeling issue, the MRA is based on two main processes:

- the analysis: used to decompose the signal of each data type to the detail signals in individual levels, and
- the synthesis: used to (re-)construct the (output) signal by the combination of detail signals.

Figure 2.5 illustrates the flowchart of the MRA process. It comprises the following main steps:

- using an appropriate reproducing kernel, the scale coefficients for each data type can be computed by a least-squares adjustment,
- determining the detail signals using scale coefficients and spherical wavelets, and
- combining individual signals to obtain the synthetic output signal.

The next parts provide the more detail view into the MRA process. They give the necessary mathematical formulation and explanation, as well as an example for the better understanding.

2.3.1 Functional model

Spherical harmonics

Spherical harmonic is the classical representation for the (global) gravity field. In the following, some basic reminders are given as the materials for next issues. Any vector $x = (x_1, x_2, x_3)^T \in \mathbb{R}^3 \setminus \{0\}$ is uniquely represented as $x = r\xi$, where $r = |x|$ and $|\xi| = 1$. Call Ω_R a sphere with radius R and $L^2(\Omega_R)$

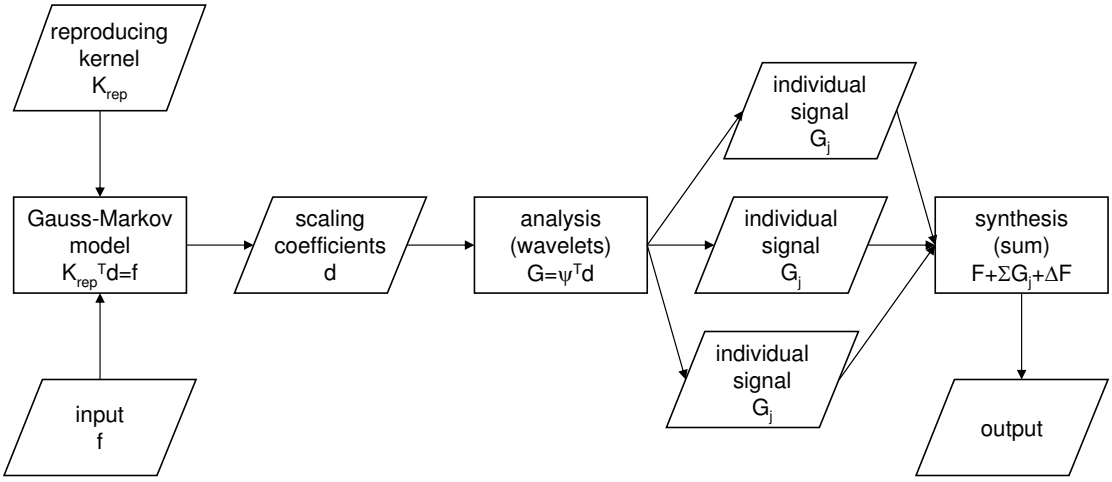

Figure 2.5: The flowchart of MRA

the space of all real square-integrable functions F on Ω_R, the spherical harmonics $Y_{n,m}(\boldsymbol{\xi})$ of degree n and order m form a complete orthonormal basis of $L^2(\Omega_R)$. The function $F \in L^2(\Omega_R)$ can be uniquely expressed as Fourier series

$$F(\boldsymbol{\xi}) = \sum_{n=0}^{\infty} \sum_{m=-n}^{n} F_{n,m} Y_{n,m}(\boldsymbol{\xi}) \tag{2.43}$$

with $\boldsymbol{\xi} \in \Omega$, $F_{n,m}$ are Stokes coefficients which can be computed via the spherical Fourier transform $F_{n,m} = \langle F, Y_{n,m} \rangle_{L^2(\Omega_R)}$.

Given the (disturbing) gravity potential F on the sphere Ω_R, the upward continuation can be written by

$$F(\boldsymbol{x}) = \sum_{n=0}^{\infty} \sum_{m=-n}^{n} F_{n,m} H_{n,m}^R(\boldsymbol{x}) \tag{2.44}$$

where the functions

$$H_{n,m}^R(\boldsymbol{x}) = \frac{1}{R} \left(\frac{R}{r} \right)^{n+1} Y_{n,m}(\boldsymbol{\xi}) \tag{2.45}$$

are the solid spherical harmonics.

Spherical base functions

The relation between the spherical harmonics and the Legendre polynomials is given by (Freeden et al. 1998)

$$\sum_{m=-n}^{n} Y_{n,m}(\boldsymbol{\xi}) Y_{n,m}(\boldsymbol{\eta}) = \frac{2n+1}{4\pi} P_n(\boldsymbol{\xi}^T \boldsymbol{\eta}) \; . \tag{2.46}$$

Note that $\boldsymbol{\xi}$ and $\boldsymbol{\eta}$ here are the unit vectors on the centripetal directions of the sphere Ω_R, not the components of the deflection of the vertical as in section 2.1. The misunderstanding is easily avoidable thanks to the context.

Equation (2.46) forms the foundation in formulating the spherical wavelets through the spherical base functions (with an approximation up to the given degree n_{max})

$$B(\boldsymbol{x}, \boldsymbol{x}_k) = \sum_{n=0}^{n_{max}} \frac{2n+1}{4\pi R^2} \left(\frac{R}{r}\right)^{n+1} B_n P_n(\boldsymbol{\xi}^T \boldsymbol{\xi}_k) \tag{2.47}$$

with $\boldsymbol{x} = r\boldsymbol{\xi} \in \Omega_{R^{ext}}$ ($\Omega_{R^{ext}}$ is the outer space including the sphere), $\boldsymbol{x}_k = R\boldsymbol{\xi}_k \in \Omega_R$, $P_n(\boldsymbol{\xi}^T \boldsymbol{\xi}_k)$ is the Legendre polynomial of degree n, and B_n are the Legendre coefficients reflecting the spectral behavior.

Now, the signal $F(\boldsymbol{x})$ can be represented by

$$F(\boldsymbol{x}) = \sum_{k=1}^{N} c_k B(\boldsymbol{x}, \boldsymbol{x}_k) \tag{2.48}$$

where N is the number of position $\boldsymbol{x}$ and the initially unknown coefficients c_k play a similar role as the Stokes coefficients $F_{n,m}$ of the spherical harmonics approach.

For $\boldsymbol{x} \in \Omega_R$, the spherical base function $B(\boldsymbol{x}, \boldsymbol{x}_k)$ depends only on the spherical distance $\alpha = \arccos(\boldsymbol{\xi}^T \boldsymbol{\xi}_k)$, i.e. the spatial positions, thus it may describe regional signals better than the spherical harmonics based on the degrees and orders, which would have to be expanded globally to large degree to achieve an equivalent representation.

Reproducing kernel

Schmidt et al. (2007) introduced the unique reproducing kernel

$$K_{rep}(\boldsymbol{x}, \boldsymbol{x}_k) = \sum_{n=0}^{n_{max}} \frac{2n+1}{4\pi R^2} \left(\frac{R}{r}\right)^{n+1} P_n(\boldsymbol{\xi}^T \boldsymbol{\xi}_k) \tag{2.49}$$

fulfilling the condition (Moritz 1989)

$$F(\boldsymbol{x}) = (K_{rep} * F)(\boldsymbol{x}) \; . \tag{2.50}$$

Rewriting the convolution $K_{rep} * F$ as a series expansion in spherical base functions K_{rep}, we can replace the original representation (2.48) by equation (2.51) in terms of the reproducing kernel

$$(K_{rep} * F)(\boldsymbol{x}) = \sum_{k=1}^{N} d_k K_{rep}(\boldsymbol{x}, \boldsymbol{x}_k) = \boldsymbol{k}_{rep}(\boldsymbol{x})^T \boldsymbol{d} \tag{2.51}$$

where $\boldsymbol{k}_{rep}$ and $\boldsymbol{d}$ are Nx1 vectors containing N values of the reproducing kernel function and scale coefficients, respectively.

2.3.2 Multi-resolution analysis

Equation (2.50) expresses the relation between spherical base functions and convolutions, i.e. the basic tool for filtering processes. The fundamental idea of the multi-resolution analysis is to split a given input signal into a smoothed version and a number of detail signals by successive low-pass filtering. In other words, the multi-resolution representation provides a sequence of signal approximations at different resolutions; the detail signals are the spectral components of multi-resolution analysis due to the fact that they are related to specific frequency bands (Schmidt et al. 2007).

Spherical scaling functions

Equation (2.52) introduces the spherical scaling function

$$\Phi_j(\boldsymbol{x}, \boldsymbol{x}_k) = \sum_{n=0}^{n_{jmax}} \frac{2n+1}{4\pi R^2} \left(\frac{R}{r}\right)^{n+1} \Phi_{j;n} P_n(\boldsymbol{\xi}^T \boldsymbol{\xi}_k) \tag{2.52}$$

of level j, with the Legendre coefficients $\Phi_{j;n} = 0$ for all $n > n_j$. This means that the scaling function works as a low-pass filter. Hence, a signal

$$F_{j+1}(\boldsymbol{x}) = (\Phi_{j+1} * F)(\boldsymbol{x}) \tag{2.53}$$

can be analyzed to the smoother version

$$F_j(\boldsymbol{x}) = (\Phi_j * F)(\boldsymbol{x}) \tag{2.54}$$

and the detail signal

$$G_j(\boldsymbol{x}) = (\Psi_j * F)(\boldsymbol{x}) \tag{2.55}$$

which contains the fine structures of $F_{j+1}(\boldsymbol{x})$ missing in $F_j(\boldsymbol{x})$.

Spherical wavelet functions

In comparison with spherical scaling functions working as low-pass filters, the spherical wavelet function

$$\Psi(\boldsymbol{x}, \boldsymbol{x}_k) = \sum_{n=0}^{n_{j+1\,max}} \frac{2n+1}{4\pi R^2} \left(\frac{R}{r}\right)^{n+1} \Psi_{j;n} P_n(\boldsymbol{\xi}^T \boldsymbol{\xi}_k) \tag{2.56}$$

can be interpreted as a band-pass filter defined by the Legendre coefficients

$$\Psi_{j;n} = \Phi_{j+1;n} - \Phi_{j;n} \; . \tag{2.57}$$

Finally, a (band-limited) signal $F(\boldsymbol{x})$ can be written as

$$F(\boldsymbol{x}) = F_{j'}(\boldsymbol{x}) + \sum_{j=j'}^{J} G_j(\boldsymbol{x}) + \Delta F_{J+1}(\boldsymbol{x}) \tag{2.58}$$

which includes the smoothed version (at a certain level j'), the detail signals at levels from j' to (maximum level) J, and the residuals

$$\begin{aligned} \Delta F_{J+1}(\boldsymbol{x}) &= F(\boldsymbol{x}) - F_{J+1}(\boldsymbol{x}) \\ &= (\Delta\Phi_{J+1} * F)(\boldsymbol{x}) \; . \end{aligned} \tag{2.59}$$

Figure (2.6) illustrates how $F(\boldsymbol{x})$, $G(\boldsymbol{x})$, and $\Delta F(\boldsymbol{x})$ look like in implementation using data modeled from the global model EGM2008 (Pavlis et al. 2008). The gravity anomaly input data are distributed on an equiangular grid whose indices of column and row are indicated on x and y axes. The z axis shows the amplitude of signal in meters (due to the application of the field transformation from gravity anomalies to geoid heights, c.f. section 2.3.4). The input signal is split to the smoothed version F6 and the detail signals G7 and G8. The higher level, the more detailed the signal; and visually, the residual ΔF contains a very high-frequency component of the signal.

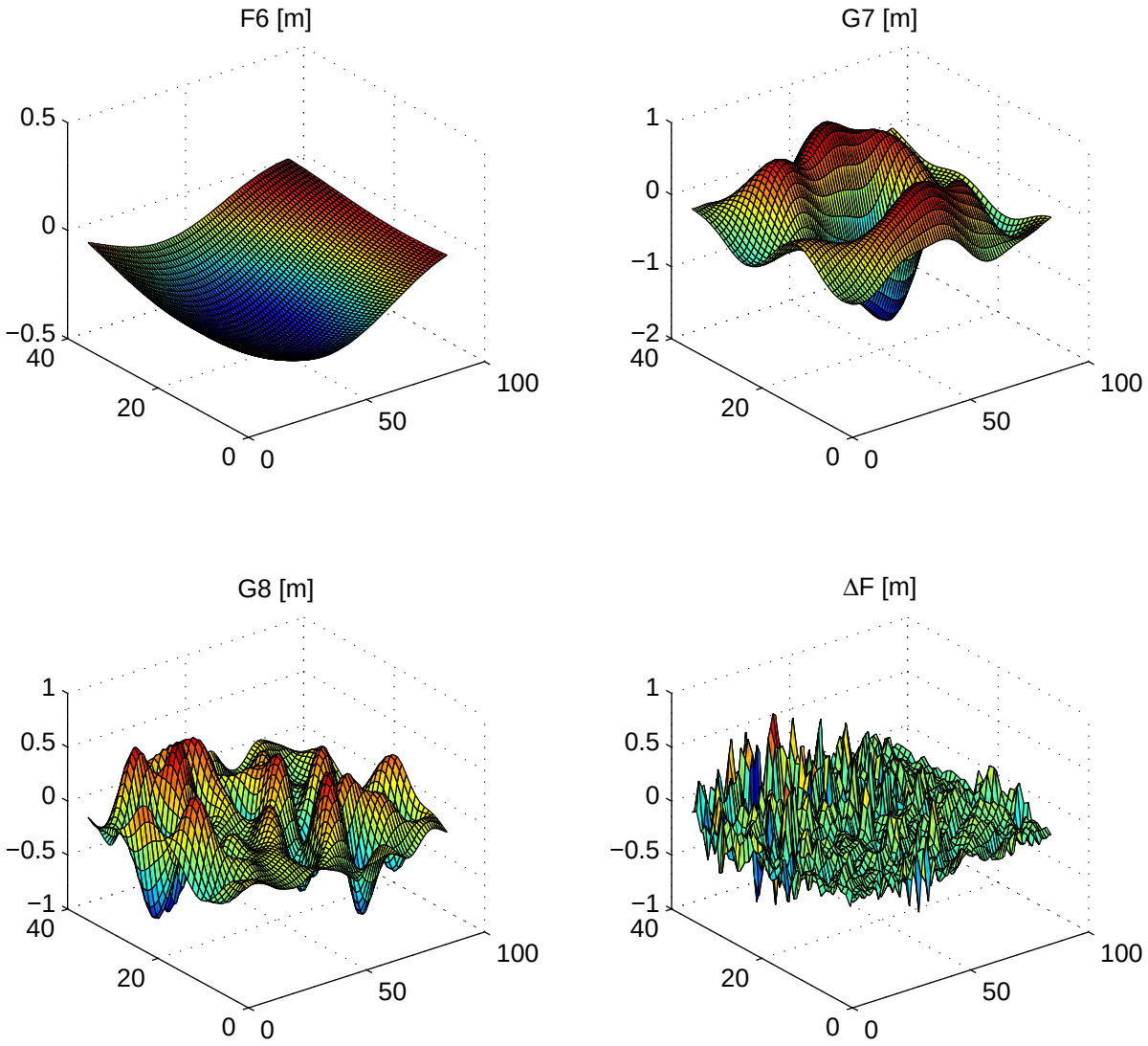

Figure 2.6: Illustration of the analysis using wavelets (left to right, top to bottom: smoothed signal at level 6, detail signals at level 7 and 8, and the residuals)

Dyadic wavelets

Several types of wavelets can be found in literature, e.g. Freeden 1999. We introduce here some dyadic wavelets because of the convenience in computation. These wavelets are represented by the Legendre coefficients of the scaling functions $\Phi_{j;n}$.

- Shannon function

$$\Phi_{j;n} = \begin{cases} 1 & \text{if } n \in [0, 2^j) \\ 0 & \text{elsewhere .} \end{cases} \tag{2.60}$$

- CuP (cubic polynomial) function

$$\Phi_{j;n} = \begin{cases} (1 - 2^{-j}n)^2(1 + 2^{-j+1}n) & \text{if } n \in [0, 2^j) \\ 0 & \text{elsewhere .} \end{cases} \tag{2.61}$$

- Blackman function

$$\Phi_{j;n} = \begin{cases} 1 & \text{if } n \in 0, 2^{j-1}) \\ A_j(n) & \text{if } n \in [2^{j-1}, 2^j) \\ 0 & \text{elsewhere} \end{cases} \tag{2.62}$$

  wherein

$$A_j(n) = \frac{21}{50} - \frac{1}{2}\cos\left(\frac{2\pi n}{2^j}\right) + \frac{2}{25}\cos\left(\frac{4\pi n}{2^j}\right) . \tag{2.63}$$

- Bernstein function

$$\Phi_{j;n} = \begin{cases} \dfrac{(2^j)!(2^j - 1)!}{(2^j - n - 1)!(2^j + n)!} & \text{if } n \in [0, 2^j) \\ 0 & \text{elsewhere .} \end{cases} \tag{2.64}$$

Figure 2.7 illustrates how the wavelets work by means of the scaling functions. The simplest case is the Shannon function which filters signals using, say, a "box". The width of box corresponds to which level (j) it filters, and can be easily calculated according to $2^j - 2^{j-1}$. Furthermore, its coefficients are clearly 1 or 0 (not any intermediate value); hence, it is convenient for monitoring and checking in simulations. In case of CuP function, the low-pass

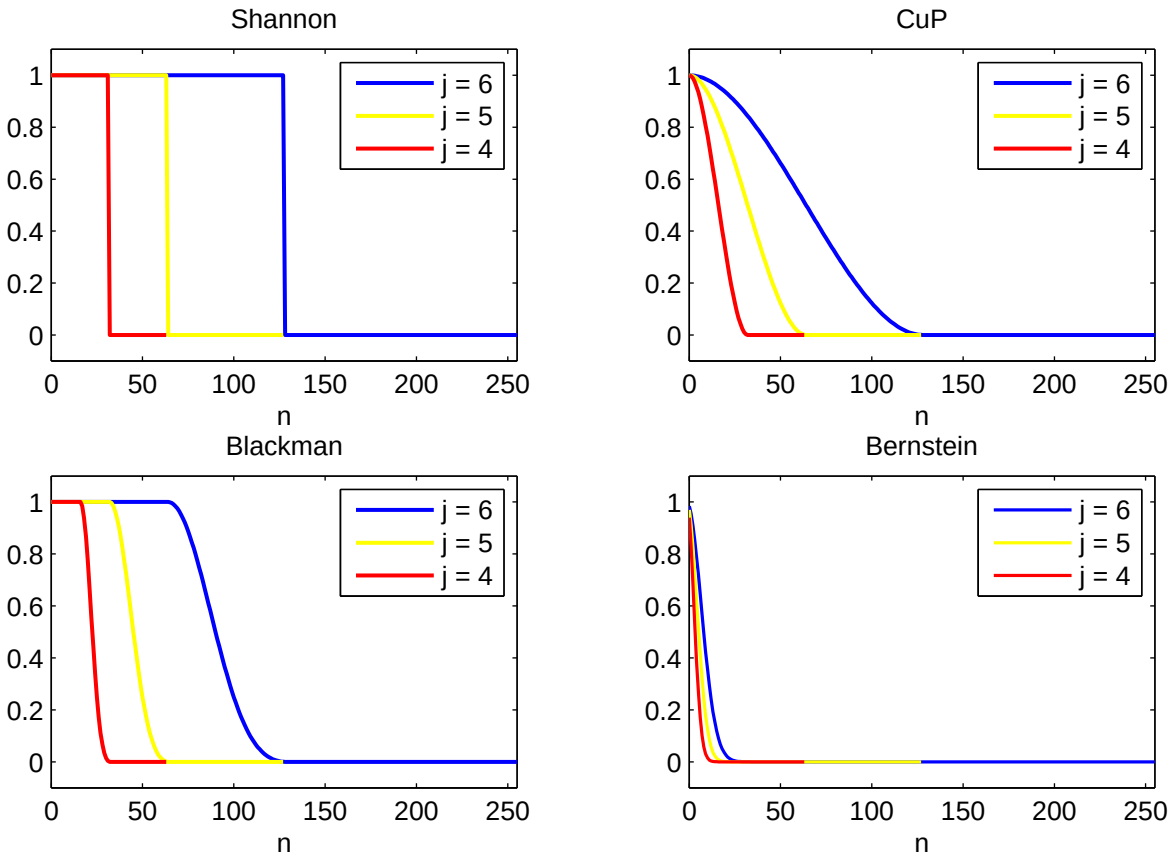

Figure 2.7: Dyadic wavelets

filter coefficients are always less than 1 for any level. Blackman function means some kind of compromise between Shannon and CuP function (figure 2.7), and in some literature (e.g. Freeden 1999, Schmidt et al. 2007), there adds a coefficient b deciding the width of band of filtered signal; $b = 2$ is equivalent to our case (dyadic).

2.3.3 Least-squares adjustment

First of all, we require a very important result through the below theorem, the proof of which can be found in Freeden et al. (1998).

Theorem

Theorem 2.1. *Let* $F \in L^2_{\Omega_R}$ *and*

$$K(\boldsymbol{x}, \boldsymbol{x}_k) = \sum_{n=0}^{\infty} \frac{2n+1}{4\pi R^2} \left(\frac{R}{r}\right)^{n+1} K_n P_n(\boldsymbol{\xi}^T \boldsymbol{\xi}_k) \tag{2.65}$$

be a kernel with

$$K_n \begin{cases} \neq 0 & \text{for } n = 0, \ldots, n_{max} \\ = 0 & \text{for } n > n_{max} \ . \end{cases} \tag{2.66}$$

Assume that

$$(K * F)(\boldsymbol{x}) = \sum_{k=1}^{N} d_k K(\boldsymbol{x}, \boldsymbol{x}_k) \tag{2.67}$$

holds. If

$$L(\boldsymbol{x}, \boldsymbol{x}_k) = \sum_{n=0}^{\infty} \frac{2n+1}{4\pi R^2} \left(\frac{R}{r}\right)^{n+1} L_n P_n(\boldsymbol{\xi}^T \boldsymbol{\xi}_k) \tag{2.68}$$

is another kernel with $L_n = 0$ *for* $n > n_{max}$*, then*

$$(L * F)(\boldsymbol{x}) = \sum_{k=1}^{N} d_k L(\boldsymbol{x}, \boldsymbol{x}_k) \ . \tag{2.69}$$

In practice, it means that we just need to determine the scaling coefficient vector $\boldsymbol{d}$ in equation (2.51) and apply it to equations (2.54), (2.55), (2.59) to

compute all components of the multi-resolution analysis according to

$$F_j(\boldsymbol{x}) = \boldsymbol{\phi}_j^T(\boldsymbol{x})\boldsymbol{d} \tag{2.70}$$

$$G_j(\boldsymbol{x}) = \boldsymbol{\psi}_j^T(\boldsymbol{x})\boldsymbol{d} \tag{2.71}$$

$$\Delta F_{J+1}(\boldsymbol{x}) = \Delta\boldsymbol{\phi}_{J+1}^T(\boldsymbol{x})\boldsymbol{d}\ . \tag{2.72}$$

Herein $\boldsymbol{\phi}_j(\boldsymbol{x})$, $\boldsymbol{\psi}_j(\boldsymbol{x})$, and $\Delta\boldsymbol{\phi}_{J+1}(\boldsymbol{x})$ are the Nx1 vectors containing values of scaling functions, wavelet functions and functions for residuals, respectively.

Parameter estimation for scaling coefficients

Rewriting equation (2.51) in the form of matrices

$$\boldsymbol{f} = K_{rep}^T\boldsymbol{d} \tag{2.73}$$

where $\boldsymbol{f}$ is the vector of input values $F(\boldsymbol{x})$, K_{rep} is the matrix containing values of the reproducing kernel function. The scaling coefficient vector $\boldsymbol{d}$ can be achieved using a standard Gauss-Markov model. The parameter estimation yields

$$\boldsymbol{d} = (A^TPA)^{-1}A^TP\boldsymbol{f} \tag{2.74}$$

where $A = K_{rep}^T$ is the design matrix, P is the weight matrix whose errors are described by $\Sigma(\boldsymbol{f}) = P^{-1}\sigma^2$ with σ^2 being the variance factor. The corresponding parameter covariance matrix can also be obtained using the error propagation

$$\Sigma(\boldsymbol{d}) = (A^TPA)^{-1}\sigma^2\ . \tag{2.75}$$

2.3.4 Field transformation

In LSC, it is implied that the field transformations underlay cross covariance matrices. In MRA, we need a particular treatment for this issue. Deriving from the relation (2.8) and expanding into the series of harmonics, we obtain (Hofmann-Wellenhof and Moritz 2005)

$$\Delta g = \frac{1}{r}\sum_{n=2}^{\infty}(n-1)T_n(\theta,\lambda)\ . \tag{2.76}$$

Equations (2.6) and (2.76) yield the degree-dependent conversion factors (Pail 2007)

$$N_n = \frac{1}{\gamma} T_n \tag{2.77}$$

and

$$\Delta g_n = -\frac{n-1}{r} T_n \ . \tag{2.78}$$

Introducing these factors into the MRA process, equation (2.49) including the Δg-to-N transformation becomes

$$K_{rep}(\boldsymbol{x}, \boldsymbol{x}_k) = \sum_{n=0}^{n_{max}} \frac{2n+1}{4\pi R^2} \left(\frac{R}{r}\right)^{n+1} \gamma \frac{n-1}{r} P_n(\boldsymbol{\xi}^T \boldsymbol{\xi}_k) \ . \tag{2.79}$$

2.3.5 Numerical example

For illustrating step by step how the MRA process works, a simplified simulation using global data is given as an example. The flowchart in figure 2.5 should be referred to for a better understanding.

The input data are gravity anomalies generated from the global model EGM2008 using harmonic coefficients up to the degree and order (D/O) 10, represented by a (globally) equiangular input grid 30×60 (equivalently, the resolution is $6^\circ \times 6^\circ$ in latitude and longitude, respectively). It means that the size of input vector $\boldsymbol{f}$ is $(30 \times 60 =)\ 1800 \times 1$. The base grid where the input data is projected onto is also globally equiangular with the resolution of $6^\circ \times 12^\circ$. Consequently, the scaling coefficient vector $\boldsymbol{d}$ is a column of $(30 \times 30 =)\ 900$ elements. Note that the input grid has to be denser (or larger) than the base grid at a certain degree to guarantee the solvability of equation (2.73), see chapter 4 for more details. The output grid representing the output signal is chosen the same as the input grid for the sake of convenience; hence the output vector is also a column of 1800 elements.

Using the reproducing kernel (2.79) which includes the field transformation, the design matrix A can be obtained; note that $A = K_{rep}^T$ has a size of 1800×900 here.

Now, the scaling coefficients can be estimated by least-squares adjustment according to equation (2.74).

The next step is the analysis of the signal to the smoothed version and detail signals at individual levels. Due to the fact that we use dyadic wavelets and the maximum harmonic D/O of input data is 10, we have three levels here: the smoothed signal F2 corresponds to harmonic D/O from 2 to 3, the detail signals G2 and G3 contain the components corresponding to harmonic D/O from 4 to 7 and from 8 to 10, respectively (figure 2.8). The computation is carried out using equations (2.52), (2.56), (2.70), and (2.71). Note that we do not consider the residual ΔF due to the very low harmonic D/O of input data which can be completely represented by three levels F2, G2, and G3.

Finally, the output signal is obtained by the synthesis by means of summing the individual signals. Here the result (the "total" in figure 2.8) are global geoidal undulations (up to D/O 10) in meters.

For an evaluation, a comparison between the computed result and the "origin" is carried out. The origin here are the global geoidal undulations generated from the global model EGM2008 using harmonic coefficients up to D/O 10, which is plotted in figure 2.8 (bottom, left) as the reference. The bottom-right plot shows that the difference between the computed signal and the original one is absolutely negligible (about 10^{-12} m). It proves that the MRA process (including the field transformation) presented above works correctly.

2.3.6 Key issues in MRA implementation

The example above shows that the MRA process works perfectly in a simplified simulation, i.e. with a small amount of data, in global scale, and at low resolution (by means of harmonic D/O). For applying to a sophisticated situation in reality, some key problems have to be solved.

Recalling the flowchart of MRA (figure 2.5) and presenting in a more animated way (also means less strictly), figure 2.9 gives us an overview about key issues in the implementation of the MRA process.

Firstly, when using a large amount of input data at high resolution, equation (2.73) becomes unstable due to the rank deficiency, and an ill-posed problem occurs. To improve the condition of normal equations, a stabilization by means of regularization is required. This issue will be presented in

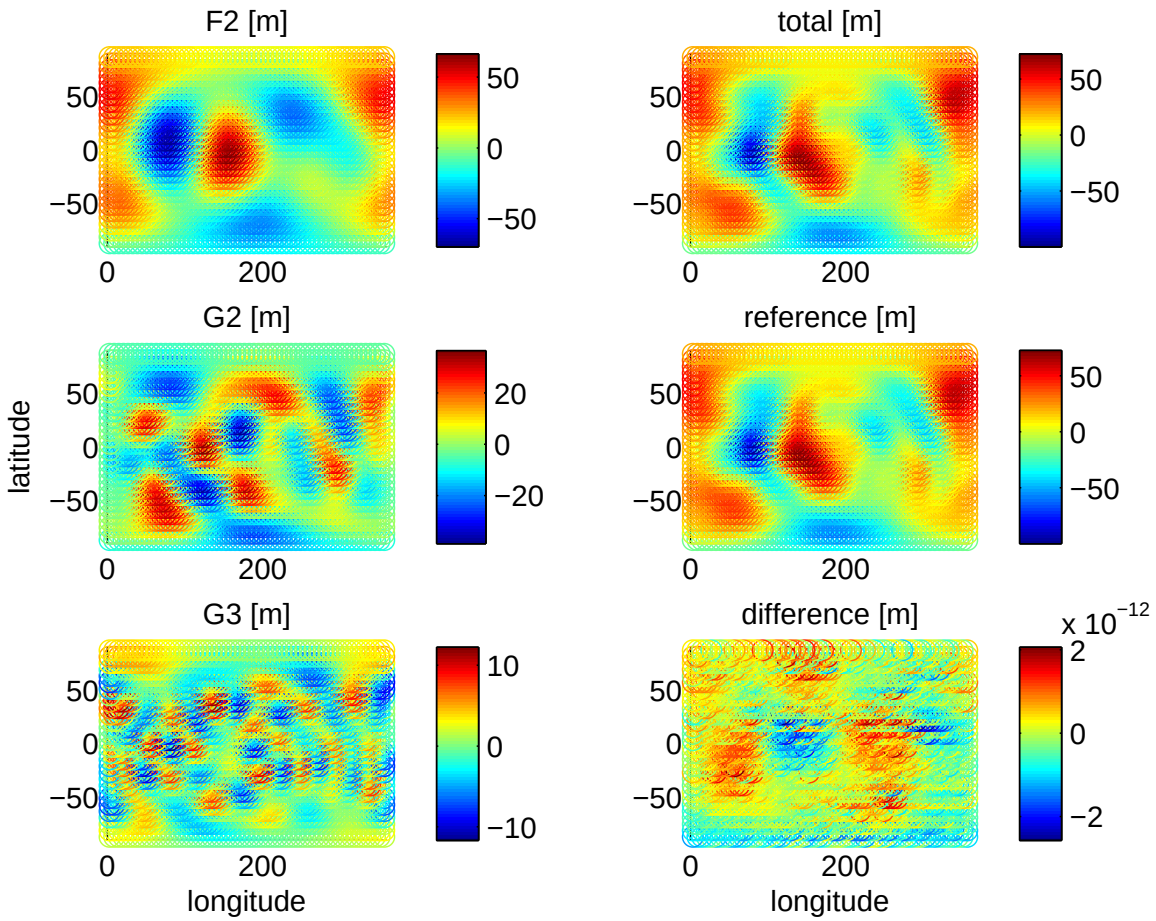

Figure 2.8: Example: top to bottom, left: the smoothed signal and detail signals at levels 2 and 3, right: output signal, the reference, and the difference between them

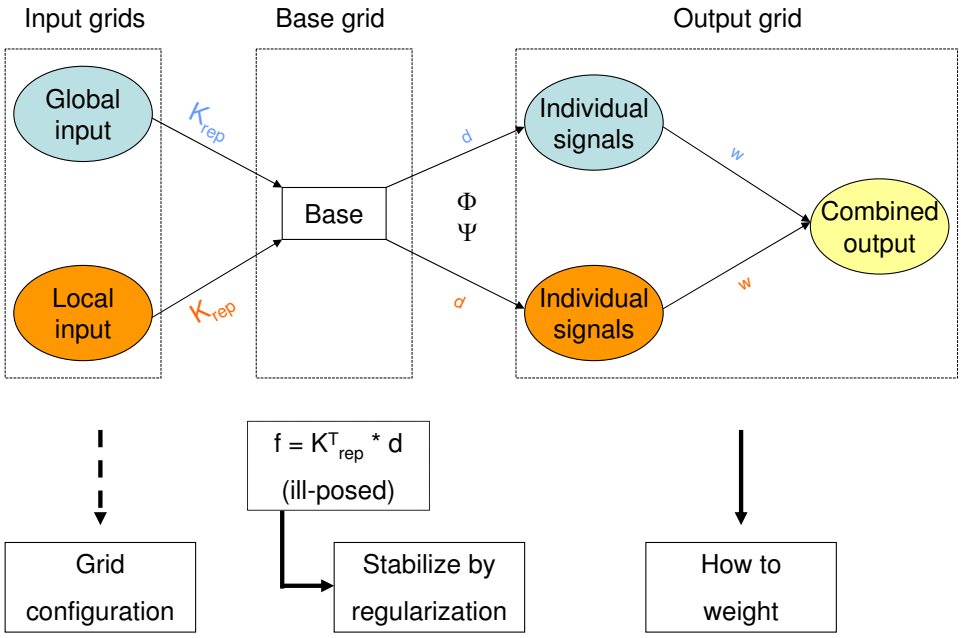

Figure 2.9: MRA process: the principle and key issues

chapter 3.

Secondly, the gravity field quantities are (discretely) represented by some kind of grids. In the scene of the MRA process, we need the input, base, and output grid. These grids have to properly represent the signals in terms of the harmonic D/O, as well as guarantee for the solvability of normal equations by means of the data sufficiency. The configuration of grids will be the content of chapter 4.

Finally, when combining signals of different types of input data at the synthesis step, the adequate weight for each component is essential. Chapter 5 will be dedicated to the weighting issue.

2.3.7 A comparison between LSC and MRA in the theoretical point of view

To complete this theoretical chapter, a comparison between LSC and MRA from a theoretical point of view is performed.

- Both of LSC and MRA are based on the linear approximation using a reproducing kernel which relates the estimated parameters to the observations; and in principle, the observations can comprise different types of (gravity field) data. In LSC, the covariance matrices, for example equation (2.40), play the role of the kernel corresponding to equation (2.49) in MRA. However; in MRA, equation (2.49) can be applied separately for each type of data sources, while in LSC, all covariance matrices have to be dealt with in the same equation (2.39) leading the huge size of the normal equations. Furthermore, the determination of covariance matrices (Moritz 1989) by itself is much more sophisticated than the computation of equation (2.49) and related equations (2.52) and (2.56).

- In both approaches, the resulting gravity field quantities are complemented by stochastic error estimates which can be computed by equations (2.38) for LSC and (2.75) for MRA. Note that equation (2.75) gives the error estimates of the scale coefficients. To obtain the final ones,

the error propagation has to be continuously applied for the following steps (figure 2.5).

- In LSC, cross-covariance matrices relate an observation quantity to each others (and to the estimated parameter), while MRA requires a particular field transformation step (c.f. section 2.3.4). However; in essence, both are derived from relations (2.6), (2.8) and (2.9).

- LSC requires the trend field (systematic components) and the global reductions while MRA does not, except the reduction of the very long-wavelength component of input data to ensure the proper representation for a local area. It would be an important advantage of MRA due to the fact that: what has been removed has to be restored again. So that the less reduction carried out, the less error propagates into the computational process.

CHAPTER 3

REGULARIZATION

In order to solve ill-posed problems numerically, regularization can be applied. An improvement of the condition of the normal equations system is achieved because some additional information about the solution is introduced. Such information can be assumptions on the smoothness or a bound on the norm.

There exist several methods for the computation of numerically stable solutions, e.g. Tikhonov regularization (Tikhonov and Arsenin 1977), biased estimation or ridge regression (Marquardt and Snee 1975), and methods based on singular value decomposition (Xu 1998). Here, Tikhonov regularization is applied. The theoretical part in this chapter is mainly based on Bouman (2000).

3.1 TIKHONOV REGULARIZATION

By minimizing the functional

$$J(\boldsymbol{d}) = \|A\boldsymbol{d} - \boldsymbol{f}\|^2 \,, \tag{3.1}$$

the solution of the linear model $A\boldsymbol{d} = \boldsymbol{f}$ can be obtained using the least square estimator

$$\boldsymbol{d} = (A^T A)^{-1} A^T \boldsymbol{f} \,. \tag{3.2}$$

However, if the model is rank-deficient, a so-called ill-posed problem occurs, i.e., a small change or error in $\boldsymbol{f}$ may cause a large change in the solution $\boldsymbol{d}$. Here regularization can be applied to improve the condition of normal equations A^TA by introducing a penalty term from some additional information (e.g. the smoothness or a bound on the norm of $\boldsymbol{f}$ or $\boldsymbol{d}$). Respectively, equations (3.1) and (3.2) become

$$J(\boldsymbol{d}_\alpha) = \|A\boldsymbol{d} - \boldsymbol{f}\|^2 + \alpha\|\boldsymbol{d}\|^2 \tag{3.3}$$

and

$$\boldsymbol{d}_\alpha = (A^TA + M)^{-1}A^T\boldsymbol{f} \tag{3.4}$$

where α is the regularization parameter, and M is the regularization matrix.

The introduction of M to the normal equations causes an error

$$\boldsymbol{d}_\alpha - \boldsymbol{d} = (A_\alpha^+ - A^+)\boldsymbol{f} \tag{3.5}$$

called regularization error or bias; herein, $A^+ = (A^TA)^{-1}A^T$ and $A_\alpha^+ = (A^TA + M)^{-1}A^T$.

In the spectral form, the solutions without and with regularization, respectively, are

$$\begin{aligned} \boldsymbol{d} &= \sum_{n=1}^{\infty} \frac{<\boldsymbol{f}, \boldsymbol{u}_n>}{\sigma_n}\boldsymbol{v}_n \\ \boldsymbol{d}_\alpha &= \sum_{n=1}^{\infty} \frac{\sigma_n}{{\sigma_n}^2 + \alpha} <\boldsymbol{f}, \boldsymbol{u}_n> \end{aligned} \tag{3.6}$$

where σ_n is the singular value of A, $\boldsymbol{v}_n$ and $\boldsymbol{u}_n$ are eigenvectors of A^TA and AA^T, respectively.

For a specific degree n, the regularized solution is written by

$$\boldsymbol{d}_{\alpha,n} = \delta_n\boldsymbol{d}_n + \delta_n\frac{\boldsymbol{\epsilon}_n}{\sigma_n}\text{ , with } \delta_n = \frac{{\sigma_n}^2}{{\sigma_n}^2 + \alpha} \tag{3.7}$$

where δ_n is the filter stabilizing the system, $\boldsymbol{d}_n$ is the exact solution from exact data, and $\boldsymbol{\epsilon}_n$ represents the data error.

The first part of the right-hand side of equation (3.7) shows that α should be as small as possible ($\delta_n \to 1$) to obtain the solution close to the exact one $\boldsymbol{d}_n$, whereas it also should be as large as possible ($\delta_n \to 0$) to reduce the

influence from data error (the second part of the right-hand side). Thus, how to choose a optimal parameter is the essence in regularization.

In equation (3.4), M can be a diagonal matrix whose diagonal contains parameters according to the number of unknowns in the normal equations; in this case, it is called multiple parameter regularization. One representative of multiple parameter regularization is the Generalized Biased Estimation (GBE) method (Bouman 2000), of which the minimizing function is

$$J(\boldsymbol{d}) = \|A\boldsymbol{d} - f\|^2 + L\|f\|^2 \text{ , with } M = L^T L \,. \tag{3.8}$$

In the simpler version, $M = \alpha I$ with α is a scalar, it is called single parameter regularization or Tikhonov regularization.

Theoretically, the multiple parameter regularization is more flexible and adequate to the inhomogeneous data (i.e., it can eliminate unnecessary regularization for some unknowns and reduce the regularization error consequently). However, in practice, the result of multiple parameter regularization is not really improved in comparison with single parameter regularization in the determination of geopotential models (Xu et al. 2006). Thus the next section is dedicated to the single parameter regularization, or so-called Tikhonov regularization, of which the essence is how to choose the optimal parameter α.

3.2 CHOICE OF REGULARIZATION PARAMETER

There exist several methods to determine the optimal parameter α in Tikhonov regularization. In principle, it is an attempt to balance the data error with the regularization error, for the goal to find a solution close to the exact one, but simultaneously with a regularization error which is as small as possible.

The L-curve method (Hansen 1992), with its visual advantage, will be presented in detail. Afterwards, also other methods are being introduced.

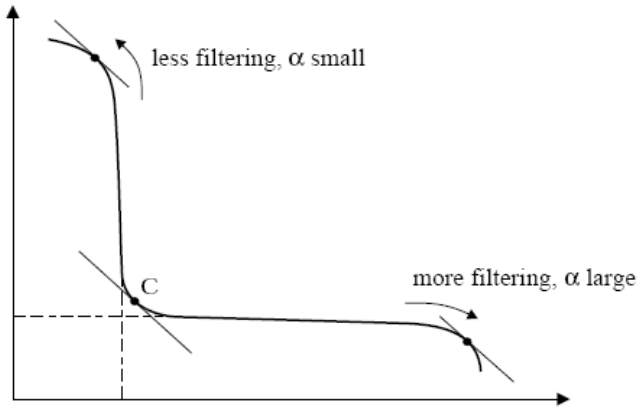

Figure 3.1: Illustration of L-curve in log-log scale (source: Hansen 1997)

3.2.1 L-curve

L-curve is the plot of the norm of regularized solution vs. the corresponding residual norm, for valid values of regularization parameter. Its L shape can be explained by considering two error components, the perturbation error and the regularization error. Referring to equation (3.7), the perturbation error caused by the erroneous data, and the regularization error caused by the regularization itself can be described in the spectral form at a specific degree n by $\frac{\epsilon_n \sigma_n}{\sigma_n^2 + \alpha}$ and $\left(\frac{\sigma_n^2}{\sigma_n^2 + \alpha} - 1 \right) \boldsymbol{d}_n$, respectively.

The vertical part of the L-curve corresponds to solutions which are very sensitive to changes in the regularization parameter because of the dominance of the perturbation error (i.e., small values of α). The horizontal part of the L-curve corresponds to solutions where the residual norm is sensitive to the regularization parameter due to the dominance of the regularization error (i.e., large values of α). Therefore, the corner of the L-curve should be expected as the balance point representing to the optimum value of regularization parameter.

The exact location of the corner can be found by the maximum value of curvature or equivalently, by using two conditions: the concavity, and that the tangent has slope -1. In practice, we can get these conditions by minimizing the function

$$\Psi(\alpha) = \|\boldsymbol{d}_\alpha\| \cdot \|A\boldsymbol{d}_\alpha - \boldsymbol{f}\| \,. \tag{3.9}$$

The key problem of this method is that the range (and the interval) of α values should be scanned. From an initial value, the range (surrounding this value) should be large enough to cover the corner, but as small as possible to get the result fast.

3.2.2 Quasi-solutions and Discrepancy principle

Quasi-solutions (Ivanov 1962) and Discrepancy principle (Morozov 1984) are a-posteriori methods finding the regularization parameter satisfying the a-priori bound of certain known information, i.e., the norm of the exact solution for Quasi-solutions or the error level for Discrepancy principle method.

Numerically, α can be obtained by solving the equation (3.10) for Quasi-solutions or equation (3.11) for Discrepancy principle method

$$Z(\alpha) = \|\boldsymbol{d}_\alpha\|^2 - c^2 = 0 \tag{3.10}$$

$$Z(\alpha) = \|\boldsymbol{f}\|^2 - < \boldsymbol{d}_\alpha, A^T\boldsymbol{f} > -\alpha\|\boldsymbol{d}_\alpha\|^2 - e^2 = 0 \tag{3.11}$$

where c is the a-priori bound of the exact solution, e is the known error level, and $<,>$ represents the inner product.

Essentially, Quasi-solutions and Discrepancy principle are two methods on the same way:

- For given $c > 0$, minimize the defect $\|A\boldsymbol{d} - \boldsymbol{f}\|$ under the constraint that the norm is bounded by $\|\boldsymbol{d}\| \leq c$;
- For given $e > 0$, minimize the norm $\|\boldsymbol{d}\|$ under the constraint that the defect is bounded by $\|A\boldsymbol{d} - \boldsymbol{f}\| \leq e$.

Which method should be chosen depends on which a-priori knowledge we have: the bound of the norm of the solution, or the data error level.

3.2.3 Generalized cross validation (GCV)

GVC method (Wahba 1990) is based on the leave-out-one idea: omitting the k^{th} observation y_k, the corresponding leave-out-one solution vector $(\boldsymbol{x})_k$ can be used to predict the "missing" observation. A good regularization parameter will product the solution where $|(A\boldsymbol{x})_k - y_k|$ is small in average over all possible y_k.

In practice, the optimal regularization parameter can be found by minimizing

$$J(\alpha) = \frac{\|A\boldsymbol{d}_\alpha - \boldsymbol{f}\|}{(\text{trace}(I-Q))^2} \text{ , with } Q = A(A^TA + \alpha I)^{-1}A^T \text{ .} \tag{3.12}$$

3.2.4 Quasi-optimality

Like the L-curve method, Quasi-optimality (Morozov 1984) also tries to compromise between the data error and the regularization error by minimizing the change in the regularized solution with respect to the regularization parameter. The optimal value is obtained when both errors are equal. Numerically one can get it by minimizing

$$J(\boldsymbol{d}, \boldsymbol{d}_{\alpha i}) = \|A\boldsymbol{d} - \boldsymbol{f}\|^2 + \alpha\|\boldsymbol{d} - \boldsymbol{d}_{\alpha i}\|^2 \text{ .} \tag{3.13}$$

3.3 SIMULATIONS

3.3.1 Simulation 1: spatial resolution and system stability

In principle, the higher the degrees and orders of the model are, the more unstable the normal equations become. The first simulation will investigate the effect of high harmonic D/O on the system stability.

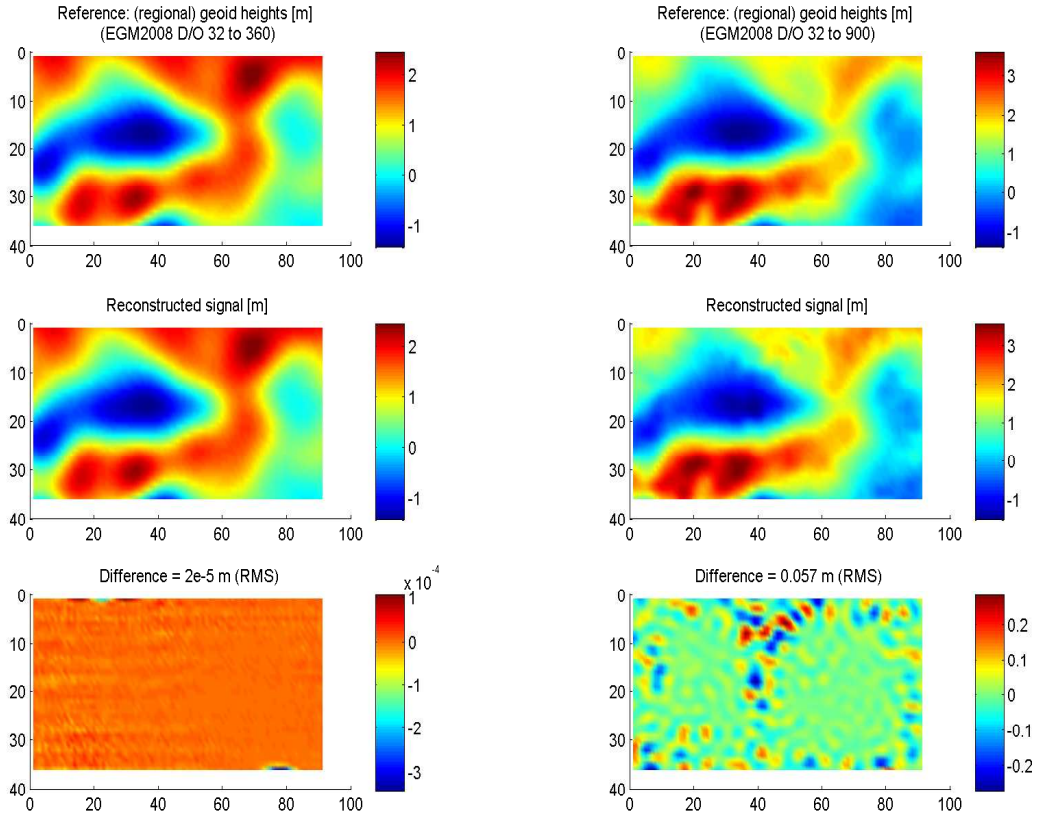

Figure 3.2: Effect of high harmonic degrees and orders on the system stability in MRA process: D/O 360 (left) vs. D/O 900 (right) (From top: the original geoidal undulations, the reconstructed signals, and their errors)

The input data are local geoidal undulations represented by an equiangular grid with the interval of $6'$ covering the Austrian territory. In the rest of this thesis, the local area implied this region (about from 46°N to 49°N in latitude and from 9°E to 18°E in longitude), unless specific notes. Due to the size of the local area, long-wavelength components of the input (under D/O 32 in terms of harmonics) have to be reduced to guarantee the proper representation of signals.

The MRA process is used to reconstruct the geoidal undulations at two different maximum degrees and orders, with no regularization applied. The two original models are generated using EGM2008 harmonic coefficients up to D/O 360 and 900, plotted in the top of figure 3.2, the middle row shows the reconstructed signals, and the errors of the MRA process (no regularization applied) are in the bottom, where we can see the obvious difference between two cases (20 micrometers vs. 6 centimeters).

Moreover, the irregular distribution and the error of input measurements also increase the instability of system (see simulation and figure 3.3 below). Hence, in practice, with the irregular and noisy observables at very high D/O (in principle infinity), regularization is one key issue requiring proper treatment.

3.3.2 Simulation 2: regularization error

The purpose of the second simulation is the investigation for regularization error. The methods mentioned above (section 3.2) will be applied to a well-posed system, where input f is the geoidal undulations computed from the model EGM96 (Lemoine et al. 1998) up to D/O 10, represented by a global equiangular grid $6^\circ \times 12^\circ$, solution $\boldsymbol{d}$ is the scale coefficient vector, and the matrix A is K_{rep}^T in the notation of chapter 2. Table 3.1 gives a comparison for several methods. The error in this scene means the root mean squares of the residuals $A\boldsymbol{d} - \boldsymbol{f}$. Note that in Tikhonov regularization applied here, the regularization matrix is $M = \alpha I$.

Obviously, regularization causes an error as a price for the stabilization. In this simulation, the error changes from micrometer level (absolutely negligible) to several centimeters. It shows that the heuristic methods (L-

Table 3.1: Errors of regularization methods

Method	Quasi-solutions	Discrepancy principle	L-curve	GCV	Quasi-optimality	No regularization
α	3.54e-27	4.54e-27	2.31e-31	1.70e-31	1.10e-31	0
Error (m)	0.05	0.07	4e-6	4e-6	6e-6	3e-11

curve, GCV, Quasi-optimality) perform much better than the a-posteriori ones (Quasi-solutions and Principle discrepancy) in the scene of MRA.

Among the heuristic methods, Quasi-optimality will be chosen for the next simulation, where a seriously ill-posed problem occurs, because of its highly automatic operation (i.e., it does not require the initial value of α as L-curve or GCV does). Furthermore, a representative of the multiple parameter regularization method, called Generalized Bias Estimation (GBE), will be also applied for a comparison.

3.3.3 Simulation 3: effect of regularization in case of noisy data with irregular distribution

In this third simulation, input data are the geoidal undulations generated from the model EGM2008 (D/O 900) and represented by 5796 points which are irregularly distributed inside the Austrian territory. These points are realistic positions of gravity measurement stations in Austria. Moreover, a white noise with amplitude of 5 cm (rms) is added to the input. The output are geoidal undulations represented by an equiangular grid with the interval of $6'$ covering the Austrian territory.

In this scenario, regularization shows its important role: without regularization, one cannot obtain a solution due to the fact that the error rises up to 1.55 m. However, this error is significantly reduced by applying regularization methods. Figure 3.3 shows that the differences between regular-

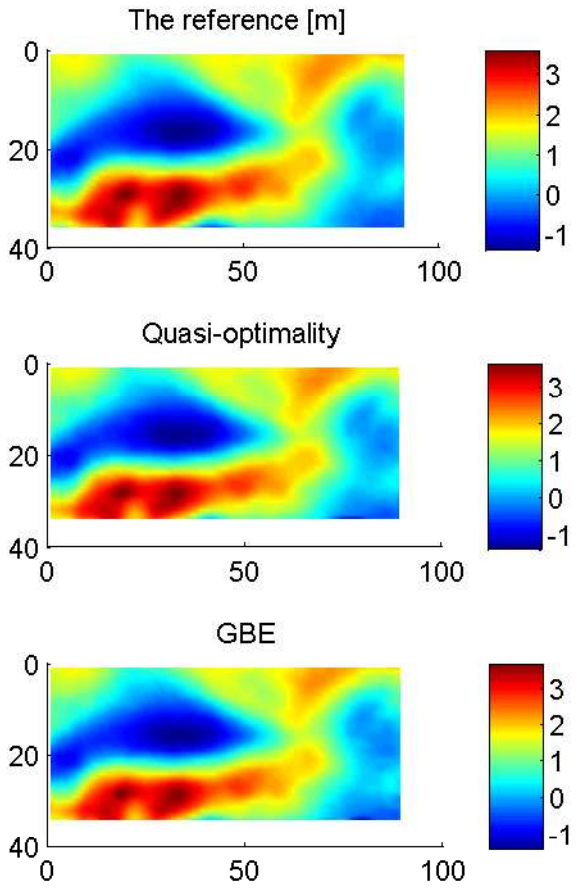

Figure 3.3: Regularized solutions and the reference (From top: the reference geoidal undulations generated from EGM2008 D/O 900, solution with Quasi-optimality, and solution with GBE regularization)

ized solutions (middle row corresponds to Quasi-optimality and bottom row corresponds to GBE) and the ”true” one (top row) which is generated from EGM2008 (D/O 900) are visually unrecognizable. In numerical values, these differences are about 5 cm rms, which is the level of white noise of the input data.

In summary, the simulations show that the irregularly distributed input data at high resolution (by means of harmonic degrees and orders) cause a seriously ill-posed problem which can be solved by regularization. Among several methods, Quasi-optimality proves to be effective one both in the aspect of regularization bias and in implementation in the scene of the MRA process. Therefore, it will be used for all simulations later on.

CHAPTER 4

GRID CONFIGURATION

Gravity field quantities are (discretely) presented by grids; they play the role of either input observations or output results. Moreover, in the scene of MRA, it requires an intermediate grid called base grid which defines the size of scale coefficient vector $\boldsymbol{d}$. Beside the type of grids which has to be defined firstly, the resolution and size require an adequate configuration to guarantee the proper representation of frequency bands contained in signals during the process.

4.1 GRID TYPE

A natural choice is a grid with equiangular intervals (along longitudinal and latitudinal directions). This popular type of grid is very convenient and easy for computing and displaying. However, at high latitudes, the grid becomes increasingly dense in longitudinal direction. Due to this disadvantage, the use of an equiangular grid should be avoided for high-latitude areas.

One solution to this problem is using a grid derived from subdividing a polyhedron (Freeden, 1999), e.g., icosahedron grid. The icosahedron grid shows an almost equidistant point distribution at high latitudes. A disadvantage is the fast increase in the number of points n from level to level γ

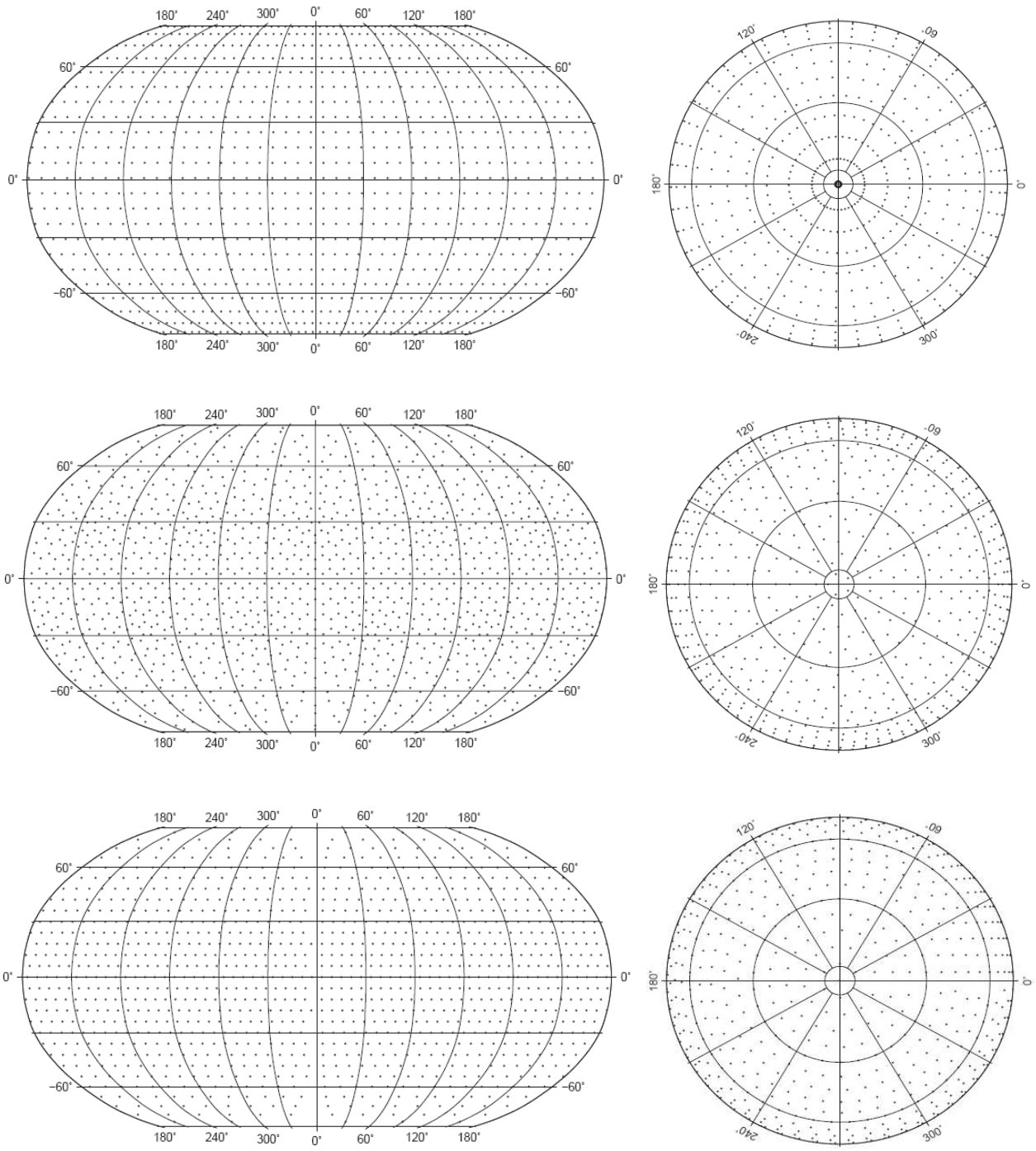

Figure 4.1: Grid types (source: Wittwer 2009) (Top to bottom: equiangular grid, icosahedron grid at level 4, Reuter grid at level 30; left to right: global scale and at high latitudes)

$$n = 20 \cdot 4^{\gamma-1} \,. \tag{4.1}$$

The Reuter grid also provides an almost equidistant point distribution, but has a slower increase of n. Compared with equation (4.1), this advantage can be observed in equation (4.2)

$$n \cong 2 + 4\frac{\gamma^2}{\pi} \tag{4.2}$$

which gives an estimate for the number of points at level γ of Reuter grid. See Driscoll and Healey (1994) for further details about Reuter grids.

For the Austrian territory (latitude is about from 46.4°N to 49°N), the disadvantage of an equiangular grid is not remarkable compared with its convenience. Moreover, Pail (2006) has also shown that there is almost no difference between using equiangular and Reuter grid for Austria. Thus, equiangular grids are preferred in this thesis.

4.2 Grid size and resolution

In the MRA process, summarily, input signals (represented by discrete data points on input grids) are projected onto a base grid via the scale coefficients d (equation (2.73)), analyzed to individual levels afterwards through wavelet functions (2.56), and finally synthesized to the output signal on an appropriate output grid (2.58). These grids (input, base, output) have the spatial correlation through the factor $\cos\psi$ (ψ is the spherical distance between two points on the sphere) and, in principle, cover the same target area. Hence, the sizes of grids are almost predefined by the limited area where we determine the local geoid. However, in practice, the input grid is usually expanded a bit due to the requirement of data redundancy (see the simulation below), and in order to reduce the boundary effects (i.e. peaks of error caused by the discontinuity of data distribution at the boundary).

The limited size of the input grid leads to the requirement of low harmonic degree reduction in order to properly represent the frequency bands. With the Austrian territory, as the test field area covers about 5 degrees in

latitude and 10 degrees in longitude, harmonic degrees lower than 32 will be reduced for all following computations.

Beside the issue of grid size, the grid resolution is also a key to ensure that the grids (input, base, and output) properly represent high-frequency bands contained in the signals. In practice, the number of local input data points is known; the output points are also given or chosen with the largest number in order to appropriately represent the output signal (by means of the frequency bandwidth following the approximation: the spatial wavelength = $180^\circ / n_{max}$). The number of base grid points, on the one hand, should be small for reducing the computation effort, on the other hand, has to be sufficiently large corresponding to the frequency bandwidth.

4.2.1 Simulation 1: grid resolution and harmonic D/O

This simulation illustrates the effect of base grid resolution onto the accuracy of the solution (scale coefficient vector $\boldsymbol{d}$) of the normal equations. The harmonic coefficients of the model EGM2008 (up to D/O 900) are used to compute the local geoidal undulations, represented by an irregular distribution of realistic positions of 5796 stations in Austria. These input signals are projected onto base grids with different resolutions (152, 555, and 3276 points, corresponds to $\Delta\theta = \Delta\lambda = 0.5^\circ$, 0.25°, and 0.1° respectively) using the MRA process. Table 4.1 shows the accuracies of solutions of scale coefficient vector $\boldsymbol{d}$ corresponding to the different base grid resolutions. It is clear that the grid resolution has to be sufficiently high in order to correspond to the frequency bandwidth to represent signals in a proper way.

4.2.2 Simulation 2: data sufficiency

Apparently, sufficient redundancy is necessary for solving the normal equations. This simulation will show the requirement of (sufficiently) redundant observables, or in other words, the number of input grid points must be sufficiently larger than that of the base grid points. The simulation will reconstruct two data sets of geoidal undulations (EGM2008 up to D/O 360)

Table 4.1: Errors of solution $\boldsymbol{d}$ correspond to different resolutions of the base grid

Case	1	2	3
Number of base grid points	152	555	3276
$\Delta\theta = \Delta\lambda$ [degree]	0.5	0.25	0.1
Error of solution $\boldsymbol{d}$ [m]	1.081	0.427	3e-7

with the base grid and output grid are the same and similar to the above simulation ($40.5^\circ \leq \theta \leq 44^\circ$, $9^\circ \leq \lambda \leq 18^\circ$, $\Delta\theta = \Delta\lambda = 0.1^\circ$). The number of base grid point is 3276, being equal to the number of unknowns (elements of scale coefficient vector $\boldsymbol{d}$). Theoretically, the number of input data has to be equal to or larger than 3276. In this simulation, two regular input grids, which differ in data density, are used to illustrate the effect of redundancy. In the first case, there are 3321 input data points ($38^\circ \leq \theta \leq 46^\circ$, $6^\circ \leq \lambda \leq 22^\circ$, $\Delta\theta = \Delta\lambda = 0.2^\circ$), where the redundancy is only 45; in the second case, 6216 input points are used ($39.5^\circ \leq \theta \leq 45^\circ$, $8^\circ \leq \lambda \leq 19^\circ$, $\Delta\theta = \Delta\lambda = 0.1^\circ$), and the redundancy now is larger. The difference between two cases is shown in figure 4.2.

The output signal in the first case (middle row) is unacceptable, when compared to the good result in the second case (bottom row) whose error is less than a millimeter in comparison with the ”true” one (top row) generated from model EGM2008 (up to D/O 360). Obviously, sufficient redundancy is required to guarantee a stable and correct solution. However, in practice, this condition does not always hold. In those situations, regularization methods should be applied to stabilize the solution and improve the final result as presented above (chapter 3).

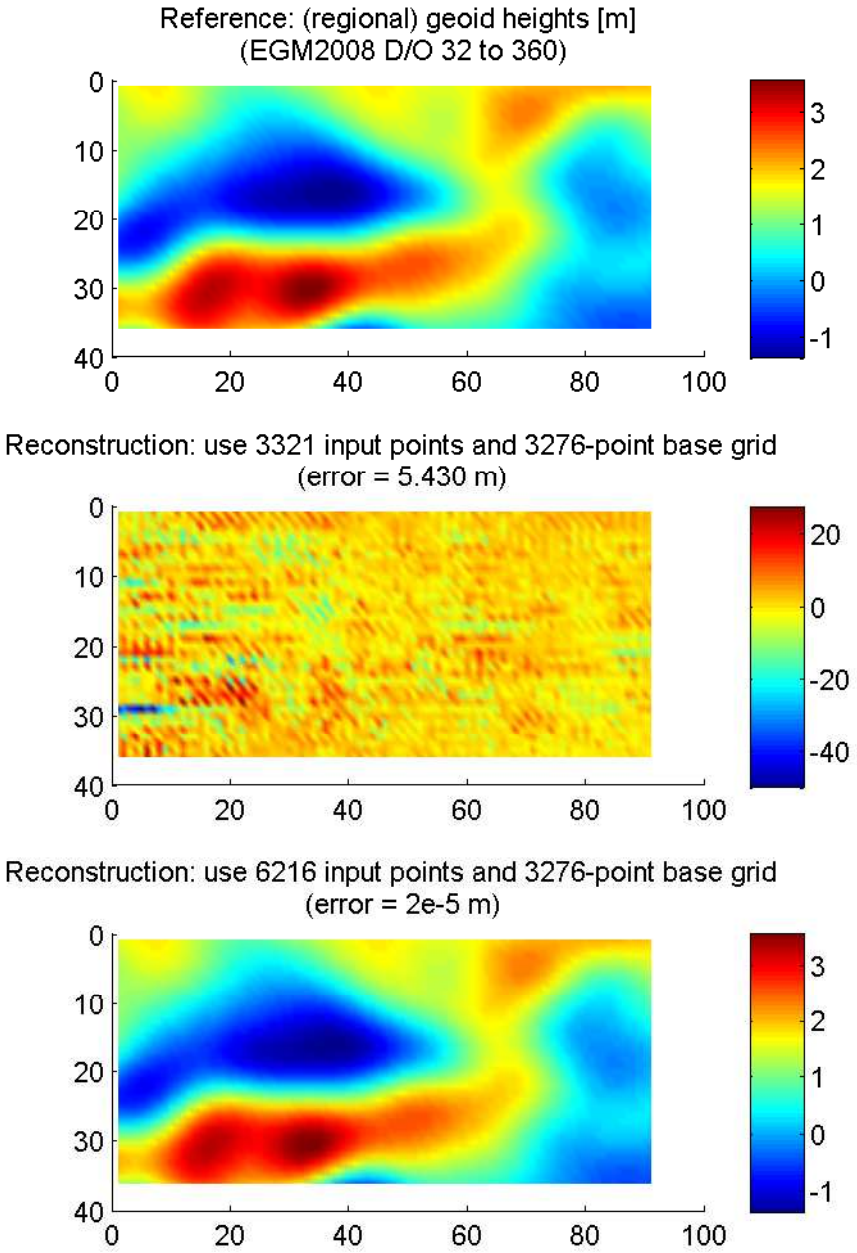

Figure 4.2: Effect of redundancy: reconstructed geoidal undulations using a 3321 (middle) and a 6216 (bottom) point input grid (base grid consists of 3276 points) in comparison with the ”true” one (top)

CHAPTER 5

GRAVITY DATA COMBINATION

In principle, data combination can be performed using the spectral weighting (i.e., only dependent on the harmonic degree), or the stochastic solution derived from the error propagation. In the scheme of the MRA process, the combination can be done right after computing the scale coefficient vector $\boldsymbol{d}$, or later with the decomposed signals in individual levels.

Generally, there is an acknowledged assumption to premise that the information from global gravity models (or satellite missions, i.e., at global scale) is reliable and properly represents the Earth gravity field at the long-wavelength part; the high-frequency part on the spectrum would be reflected by the terrestrial observation which is accurately measured in a small area. In this point of view, the weighting methods for combining global and local data are usually based on the information derived from the harmonic degree, so-called spectral weighting or deterministic method.

On the other hand, if the stochastic information of both data sources is available, and the error propagation is properly performed during the computation process, we can weight data using solely this covariance information. In this way, the weighting methods are denoted as stochastic methods.

Next, both kinds of weighting method (in the scheme of the MRA process) are presented. After that, a combined spectral-stochastic weighting method will be proposed.

5.1 STOCHASTIC WEIGHTING

The weights for global and local components of the detail signals can be determined by means of error propagation through the computation process. Together with the estimation of the scale coefficient vector $\boldsymbol{d}$, also its variance-covariance matrix can be computed

$$\boldsymbol{d} = (A^T P A)^{-1} A^T P \boldsymbol{f} \,, \tag{5.1}$$

$$\Sigma(\boldsymbol{d}) = (A^T P A)^{-1} \sigma^2 \tag{5.2}$$

where σ^2 is the variance factor of input data, of which the error described by $\Sigma(\boldsymbol{f}) = P^{-1}\sigma^2$ propagates to the covariance matrix $\Sigma(\boldsymbol{d})$ of the scale coefficient vector $\boldsymbol{d}$.

In case of applying regularization methods, equations (5.1) and (5.2), respectively, become

$$\boldsymbol{d} = (A^T P A + M)^{-1} A^T P \boldsymbol{f} \tag{5.3}$$

and

$$\Sigma(\boldsymbol{d}) = N^{-1} A^T P A N^{-1} \sigma^2 \tag{5.4}$$

where M is the regularization matrix and $N = (A^T P A + M)$.

Based on the definition $G = \boldsymbol{\psi}^T \boldsymbol{d}$, the covariance matrix of the detail signal G can be estimated at each individual level j by

$$\Sigma(G) = \boldsymbol{\psi} \Sigma(\boldsymbol{d}) \boldsymbol{\psi}^T \,. \tag{5.5}$$

Similarly, for the residual signal

$$\Delta F = \Delta \boldsymbol{\phi}^T \boldsymbol{d} \,, \tag{5.6}$$

the corresponding covariance matrix can be obtained according to

$$\Sigma(\Delta F) = \Delta \boldsymbol{\phi} \Sigma(\boldsymbol{d}) \Delta \boldsymbol{\phi}^T \,. \tag{5.7}$$

Finally, the weights for detail signals G at each level j can be determined as the inverse of variance values extracted from covariance matrices

$$w_G = \frac{1}{\sigma_G^2} \tag{5.8}$$

with the boundary condition: $w^{glo} + w^{loc} = 1$.

With the full covariance matrices propagated through the computational process, this weighting method can reflect the stochastic characteristic of input data, and also the spatial relation of local observations. Another major advantage is that we can estimate the error of the output model.

However, the weighting values based on stochastic-only approach indicate the non-negligible role of local data in low levels (by means of low harmonics or long wavelengths in the spectral domain) where the dominance of (the long-wavelength part of) global data is assumed.

5.2 SPECTRAL WEIGHTING

The degree variance which expresses how much energy is contained in a certain frequency can be computed using the fully normalized harmonic coefficients $\overline{C}_{nm}$ and $\overline{S}_{nm}$

$$\sigma_n{}^2 = \sum_{m=0}^{n} (\overline{C}_{nm}^2 + \overline{S}_{nm}^2) \ . \tag{5.9}$$

Its "error", the error degree variance, is similarly computed from the variances of $\overline{C}_{nm}$ and $\overline{S}_{nm}$

$$\epsilon_n^2 = \sum_{m=0}^{n} (\delta\overline{C}_{nm}^2 + \delta\overline{S}_{nm}^2) \tag{5.10}$$

where $\delta\overline{C}_{nm}$ and $\delta\overline{S}_{nm}$ are the standard deviation of $\overline{C}_{nm}$ and $\overline{S}_{nm}$, respectively.

Like the measurement error in the stochastic approach, this kind of "error" in spectral domain will be used for weighting. Firstly, the ratio between the error degree variance (edv) ϵ_n^2 and the degree variance (dv) σ_n^2 expressing the percentage of error in the spectral domain of the harmonics at each degree is computed. Figure 5.1 illustrates this information for about first 900 degrees of EGM 2008.

The higher the degree is, the larger the relative error $\dfrac{\epsilon_n^2}{\sigma_n^2}$ is, or in other words, the lower the reliability of information extracted from the harmonics is. The weights of the global data are proportional to this reliability

$$w_n = 1 - \frac{\epsilon_n^2}{\sigma_n^2} \ . \tag{5.11}$$

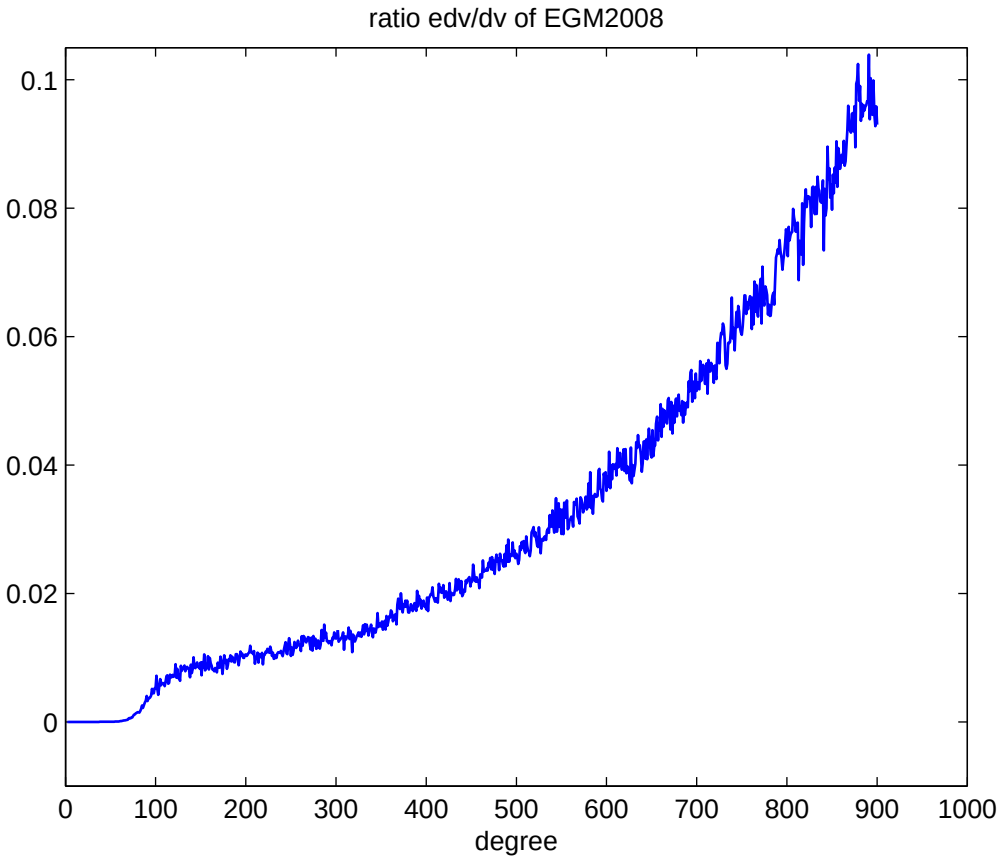

Figure 5.1: The ratio $\frac{\epsilon_n^2}{\sigma_n^2}$ of EGM2008 (D/O 900)

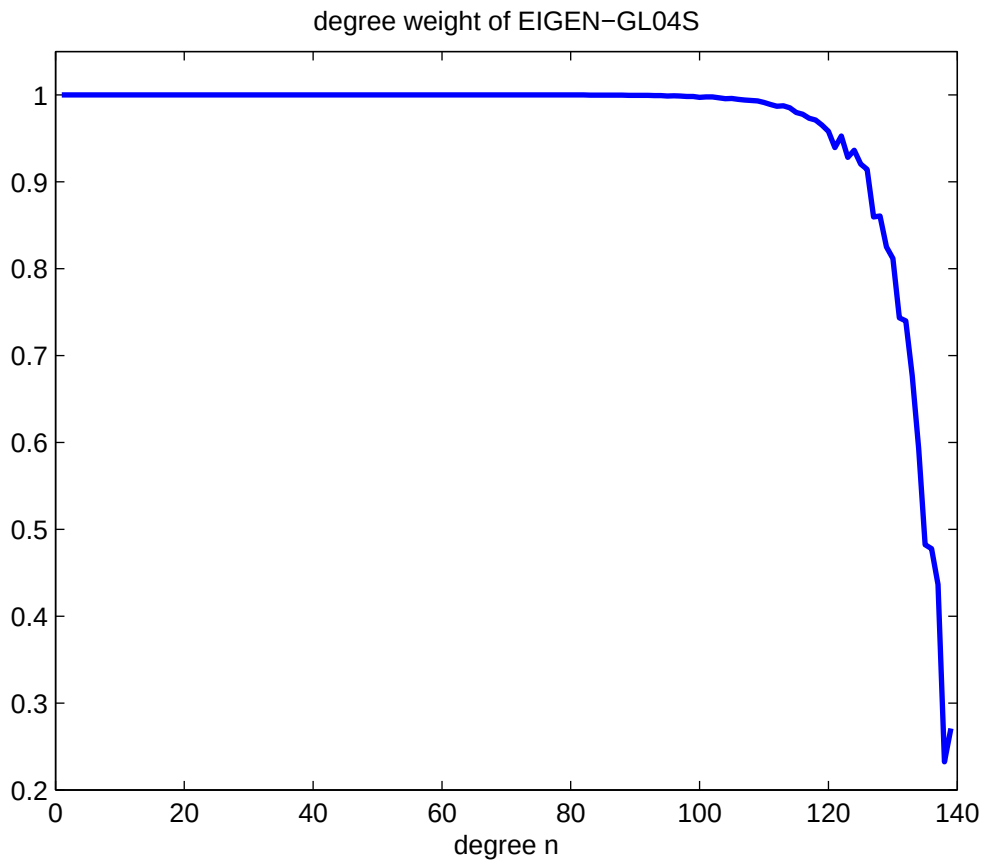

Figure 5.2: The degree-weight values of EIGEN-GL04S (D/O 140)

Figure 5.2 illustrates the weight (with respect to degree n) of the global model EIGEN-GL04S (D/O 140).

Finally, this weighting is introduced to the MRA process by computing the weight values for each level j according to

$$w_{n,j} = \frac{\sum_{n=0}^{n'} w_n \Phi_{n,j}}{\sum_{n=0}^{n'} \Phi_{n,j}} \tag{5.12}$$

where $\Phi_{n,j}$ is the coefficient of the kernel function in equations (2.60) or (2.61), (2.62), (2.64), and ($n' = 2^{j-1} - 1$). The weights for local data also agree with the boundary condition: $w^{loc} = 1 - w^{glo}$.

In the MRA process, the input data is decomposed into individual levels

separated by frequency intervals in the spectral domain; thus the spectral weighting seems to be a proper method for combining the detail signals of both global and local sources. However, this deterministic method neglects all possible stochastic a-priori information about the data. It also does not take the spatial relationship of the observables into account, or in other words, there is only one weighting value for each level, not for each point. Moreover, this method cannot estimate the output error by itself.

5.3 Combined spectral-stochastic weighting

Generally, the spectral method works well for weighting the detail signals in the wavelet process; however, for taking full advantage of the stochastic information of input data, a combined spectral-stochastic weighting method is proposed.

From equations (5.8) and (5.12), the combined weights can be determined according to

$$w_j = w_{n,j} \cdot w_{G,j} \,, \tag{5.13}$$

with the boundary condition

$$w_j^{glo} + w_j^{loc} = 1 \,. \tag{5.14}$$

Using this weighting method, all advantages of both spectral and stochastic weighting are taken into account. Every point (of output grid) at every level has a weighting value satisfying the premise that the global information dominates at the long-wavelength part in the spectral domain but gradually decreases according to the increase of the frequency.

Figure 5.3 illustrates the (mean of) weight values for all levels when combining the global component from the model EIGEN-GL04S and the local gravity anomalies in Austria (see chapter 6). Analyzing each level in more detail, the weights for every point in level 6 are plotted in figure 5.4. These values are the weight applied in the simulation at section 6.8.

One more key advantage is that the error of the output model can be

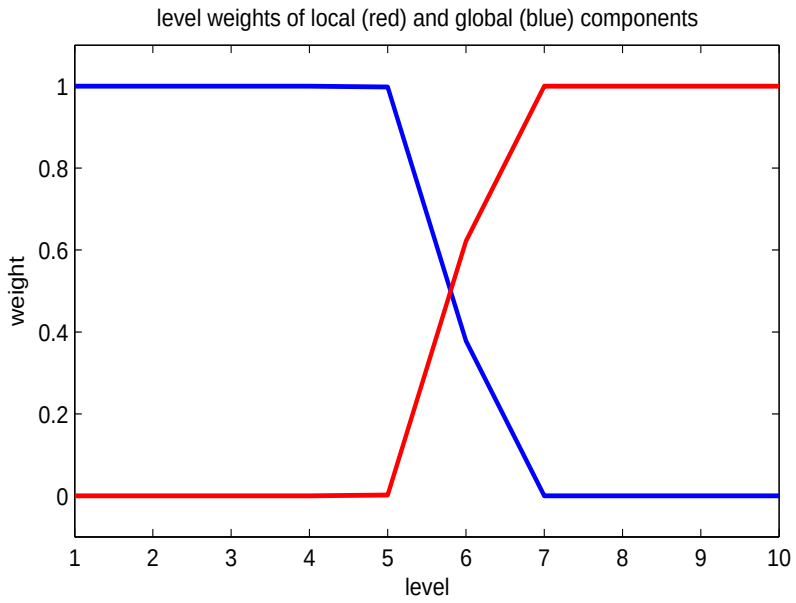

Figure 5.3: Combined weights of levels (blue for global and red for local component)

estimated according to

$$\sigma_j^2 = w_j^{glo} \cdot (\sigma_j^{glo})^2 + w_j^{loc} \cdot (\sigma_j^{loc})^2 \tag{5.15}$$

and

$$\sigma^2 = \sum_{j=1}^{J} \sigma_j^2 \,, \tag{5.16}$$

where $(\sigma_j^{glo})^2$ and $(\sigma_j^{loc})^2$ are the variance factors extracted from the corresponding covariance matrices $\Sigma(G)$ (of the global and local data).

When should we make the combination?

One important question is raised in the process: When should we make the combination? In principle, we can combine either at the step when the scale coefficient vector d is computed, or after getting all detail signals at the very end of the process. The combination right after getting the scale vector d will reduce the computation effort; however, the spectral weighting cannot

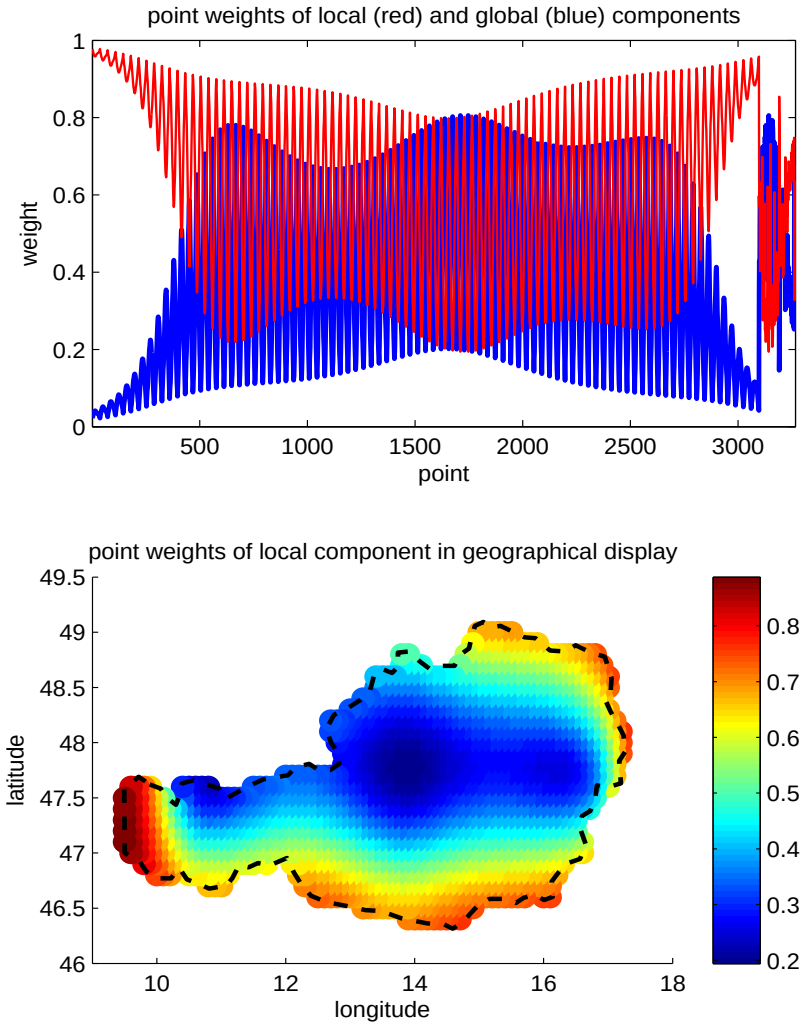

Figure 5.4: Combined weights of points at level 6, blue for global and red for local component (top), and weights of local component in geographical display (bottom)

be applied to the scale coefficient vector $\boldsymbol{d}$ due to the algorithm used in this MRA process (we have only one set of scale coefficients for all levels). Therefore, the weighting methods are applied at the level of the detail signals in the computation.

CHAPTER 6

NUMERICAL RESULTS

The main content of this chapter is the computation for a geoid solution for the case study of Austria. At first, the data sources and the set-up for the computations are described. After that, several computation approaches are presented, as well as an overview about the reference solution will be given.

6.1 DATA SOURCES

In principle, there are two main data sources: the global and the local data. The local data, in this scene, are the terrestrial observables, while the global data can be extracted from the earth gravity models. In the view of frequency characteristic, it is presumed that the global models represent properly the long-wavelength part, while the short-wavelength information should be found in the terrestrial observables.

6.1.1 Global data

There exist several global gravity models. In the following, a short introduction of the models EGM96 (Lemoine et al. 1998), EGM2008 (Pavlis et al. 2008), and EIGEN-GL04S (ESA website) used in this thesis is given.

The EGM96 model is based on the WGS84 ellipsoid, and the coefficients are calculated from a worldwide database of 30 minute mean free-air gravity

anomalies plus the satellite tracking data and the direct altimetry. EGM96 is a composite solution for a geopotential model of the earth. The NASA Goddard Space Flight Center (GSFC), the National Imagery and Mapping Agency (NIMA), and the Ohio State University (OSU) have collaborated to develop an improved spherical harmonic model of the Earth's gravitational potential to degree 360. The final solution blends a low-degree combination model to degree 70, a block-diagonal solution from degree 71 to 359, and a quadrature solution at degree 360. The model was used to compute the Geoid undulations with the accuracy better than one meter (with the exception of areas void of dense and accurate surface gravity data) and realize WGS84 as a true three-dimensional reference system. A detail description can be found in Lemoine et al. (1998). This very classical and popular model is used in this thesis for some beginning simulations which do not require a high D/O model.

The Earth Gravitational Model EGM2008 was publicly released by the US National Geospatial-Intelligence Agency (NGA) EGM Development Team. This gravitational model is complete to spherical harmonic degree and order 2159, and contains additional coefficients extending to degree 2190 and order 2159 (see Pavlis et al. 2008 for more details). This is the recently highest resolution model and is used for several simulations in this thesis.

In contrast to the two above composite models, EIGEN-GL04S is a pure satellite data model, complete to degree and order 150 from GRACE and LAGEOS data only. It is given in normalized spherical harmonic coefficients in ITRF2000, and uses exactly 2 years of GRACE plus LAGEOS data (73 ten-day periods between 2003/02/24 and 2005/02/23). Its reference date is 2004.0. This field does not include time-variable terms. This model and its relatives on the series of GL04 models can be found at the website of ESA. EIGEN-GL04S is used as the main global data for the final computations in this thesis.

6.1.2 Local data

For local data, the acquisition and pre-processing of the terrestrial observables are not easy, and very time consuming. In this thesis, we use the

same terrestrial data sources as in the project GEOnAUT (Pail 2007), see section 6.3 for an overview about this project, whose results play a role as the reference solution for this thesis.

The main characteristics and key statistical parameters of the local data are extracted from Pail et al. 2008 as follow:

Derived from a quite inhomogeneous data set of about 122 000 gravity anomaly points, all data is classified by its height and position errors (using a DTM) and reduced to a smaller but more homogeneous data set with the approximate distance between observables is about 4 km. The distribution of this reduced data set of 14001 points is shown in figure 6.1. While the distribution in the Austrian territory is very homogeneous, the distribution in Czech as well as Slovakia is too sparse, the distribution in the regions near the border could be denser, and there is a gap in the North of Slovenia where accurate data are missing. The internal consistency of this gravity anomaly data set has been validated by separating this data set into two sub-sets, using one of them as the input of a LSC procedure, predicting gravity anomalies at the stations of the complementary data set, and, finally, comparing the residuals between predicted and measured values. It can be summarized that the gravity data set is (partly) homogeneous, but improvements along the Austrian border are desirable.

The (free-air) anomalies here are computed in Molodensky's sense, i.e. by subtracting the normal gravities on telluroid from the measured gravities on the ground. For using in least-squares collocation approach, the topographic-isostatic reduction and the global reduction up to harmonic D/O 70 (using the model EIGEN-GL04S), as well as the indirect effect are computed for this data set. This reduction procedure leads to a significantly smoother signal, as shown in figure 6.2 (reduced anomalies) in comparison with the free-air anomalies (no reduction) in figure 6.3. The effect of the reductions is also numerically expressed throw the statistical parameters in table 6.1.

In brief, we have both the original observables, i.e. the (free-air) gravity anomalies, and the reduced gravity anomalies (global reduction, topographic-isostatic reduction, and indirect effect) data being ready for several computation approaches later on.

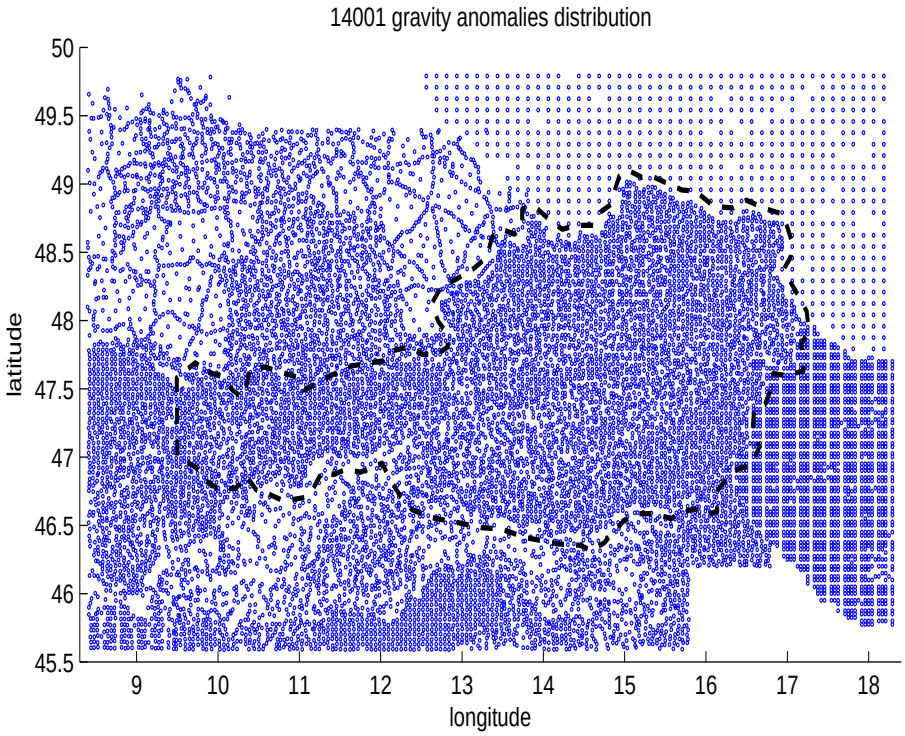

Figure 6.1: Distribution of 14001 gravity anomalies

Table 6.1: Key statistical parameters of local data

Gravity anomalies [mGal]	min [mGal]	max [mGal]	std. dev. [mGal]
Free-air	−155.60	200.86	42.32
Reduced	−75.29	21.47	19.60

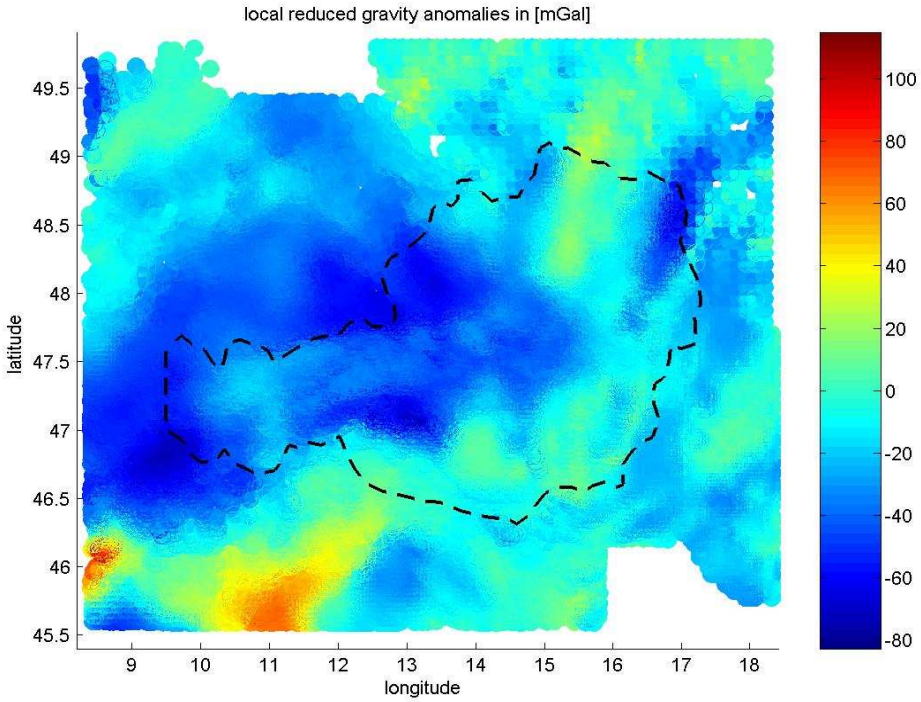

Figure 6.2: 14001 reduced gravity anomalies (reductions: global, topographic-isostatic, and indirect effect)

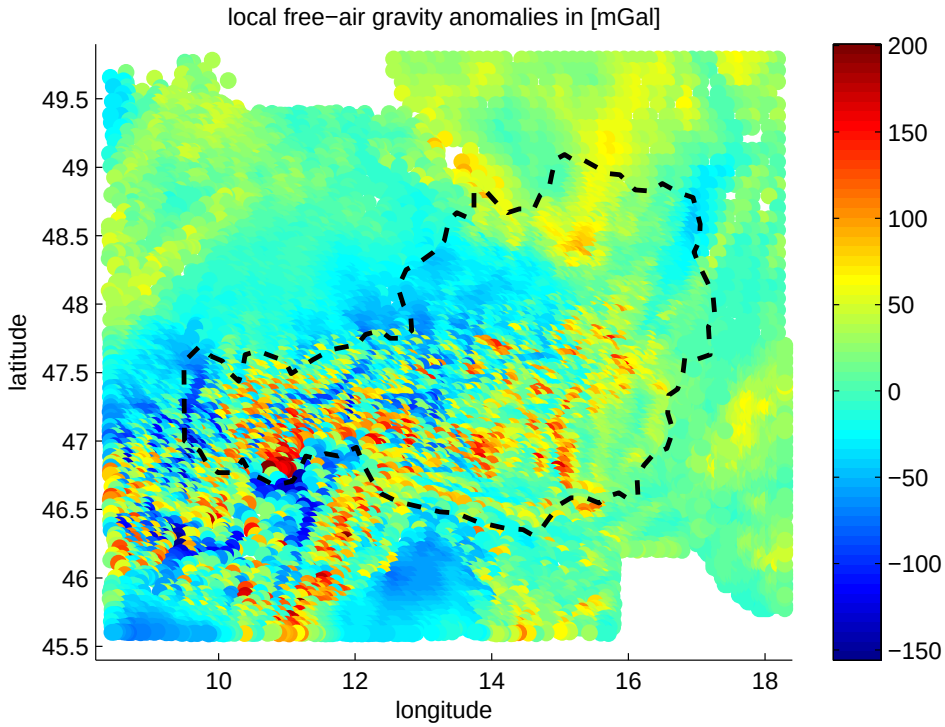

Figure 6.3: 14001 free-air gravity anomalies (no reduction)

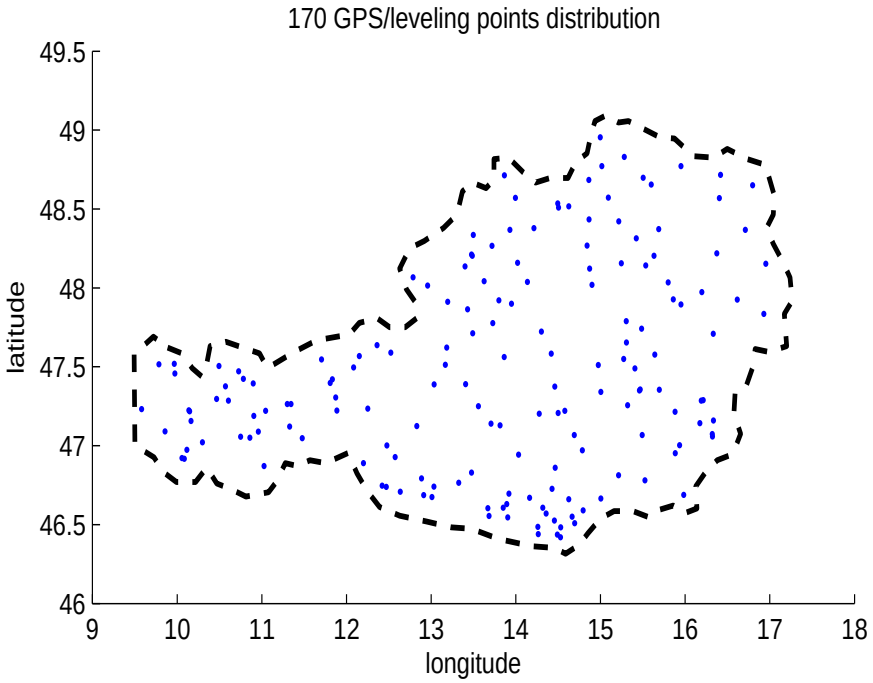

Figure 6.4: Distribution of 170 GPS/leveling points

The other important type of terrestrial observables is the GPS/leveling measurement. It is usually used for validating (fitting) and evaluating (checking) the computed geoid heights, or sometime included in the computation. It should be mentioned that if the GPS/leveling data set is used as an input data source, the resulting surface is more or less forced to the GPS/leveling points, and thereby mapping all the systematic errors from the height system and GPS measurements. Moreover, the combination with the other data sources requires appropriate weighting solutions (see next sections). In this thesis, 170 GPS/leveling points covering the Austrian territory will be used for combining, fitting, and checking as well. The distribution of these points can be seen in figure 6.4.

Furthermore, there are about 670 deflections of the vertical, which entered the GEOnAUT solution. However, due to their limited impact on the final combined solution, they are not used in the computation process here.

6.2 SET-UP OF COMPUTATION SCHEME

The set-up for a computation scheme comprises the choice and definition for several parameters such as the scaling function and the highest level used (in the scene of MRA), regularization method, grid resolution, the degree of global reduction, weighting schemes, and data sets. Based on the fundamentals and simulations presented in previous chapters, the set-up for later computations is described in the following.

6.2.1 Choice of scaling function and j_{max}

Among several dyadic kernels introduced in chapter 2, the Shannon function is the simplest one. Its response consists only of zero and one, so it is very convenient and easy for monitoring and checking in small beginning simulations. Consequently, due to its simplicity and reliability, it was used for all later simulations as well as the final computations.

When using a dyadic kernel, the signal is analyzed into individual levels; a level j corresponds to the frequency bandwidth of, in terms of harmonic degree and order, from 2^j to $2^{j+1}-1$. Now the question is: how many levels should we use, or equivalently, what is the highest level j_{max}? Generally, the answer is: the higher the better, due to the fact that the highest harmonic D/O of terrestrial observations is, in principle, infinity. If j_{max} is too small, the high-frequency component of the signal will be missing. On the contrary, the too large j_{max} will increase the computational effort and require the corresponding amount of input data. The simulation below will give a specific answer for the real data set of Austrian gravity anomalies.

From the 14001 topographic-isostatic reduced gravity anomalies described above, a set of 5667 values inside the Austrian territory is extracted. This data set will be reconstructed using the MRA process with different values of j_{max} (6, 8, and 10, respectively). The differences between the reconstructed signals and the original one will point out how much information is missing during the process using 6, 8, and 10 levels.

Figures 6.5, 6.6, and 6.7 illustrate for cases $j_{max} = 6$, $j_{max} = 8$, and $j_{max} = 10$, respectively. Each figure comprises the individual signals (left),

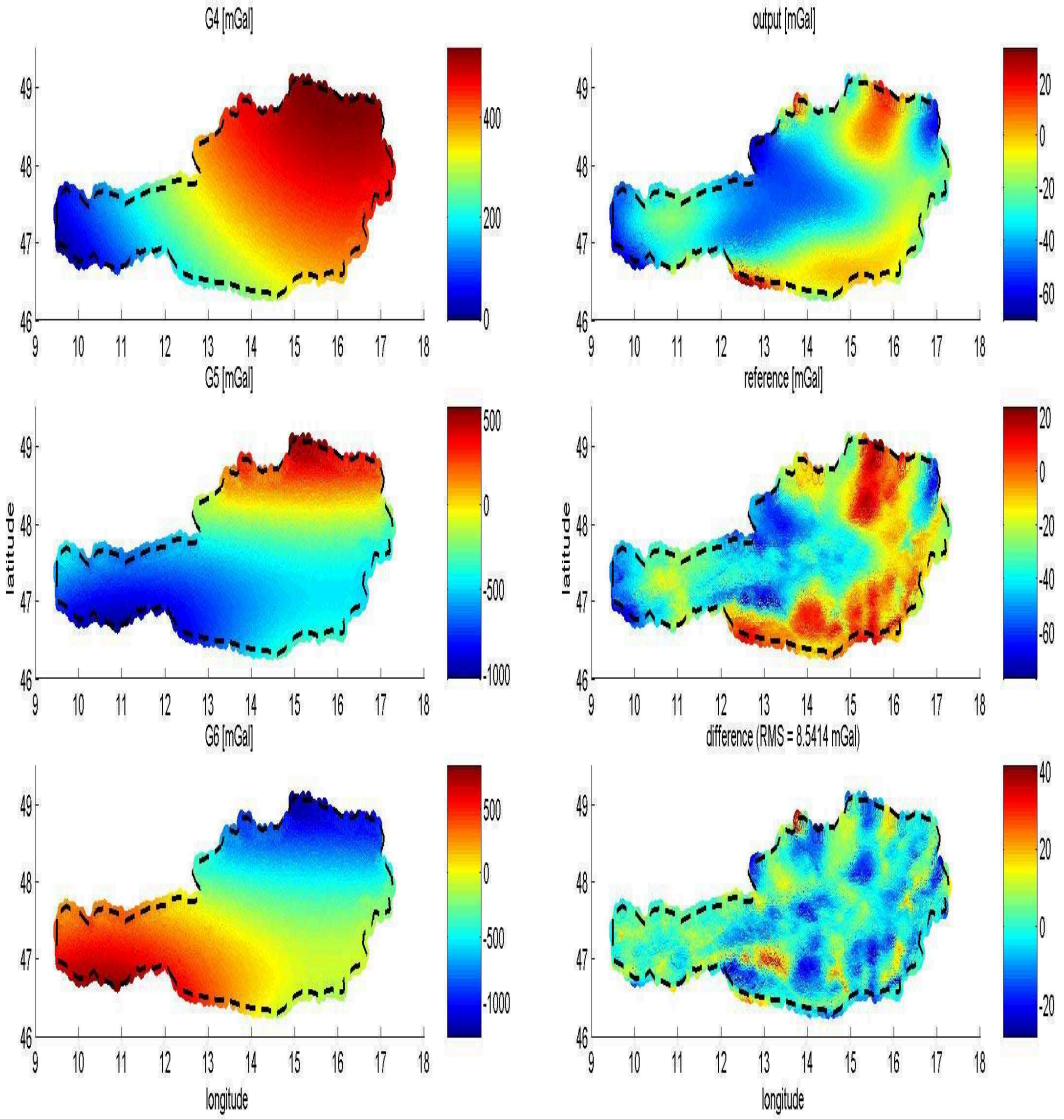

Figure 6.5: Signal reconstruction using 6 levels. Left: detail signals at levels 4, 5, 6; right: reconstructed signal, the reference, and their difference (top to bottom)

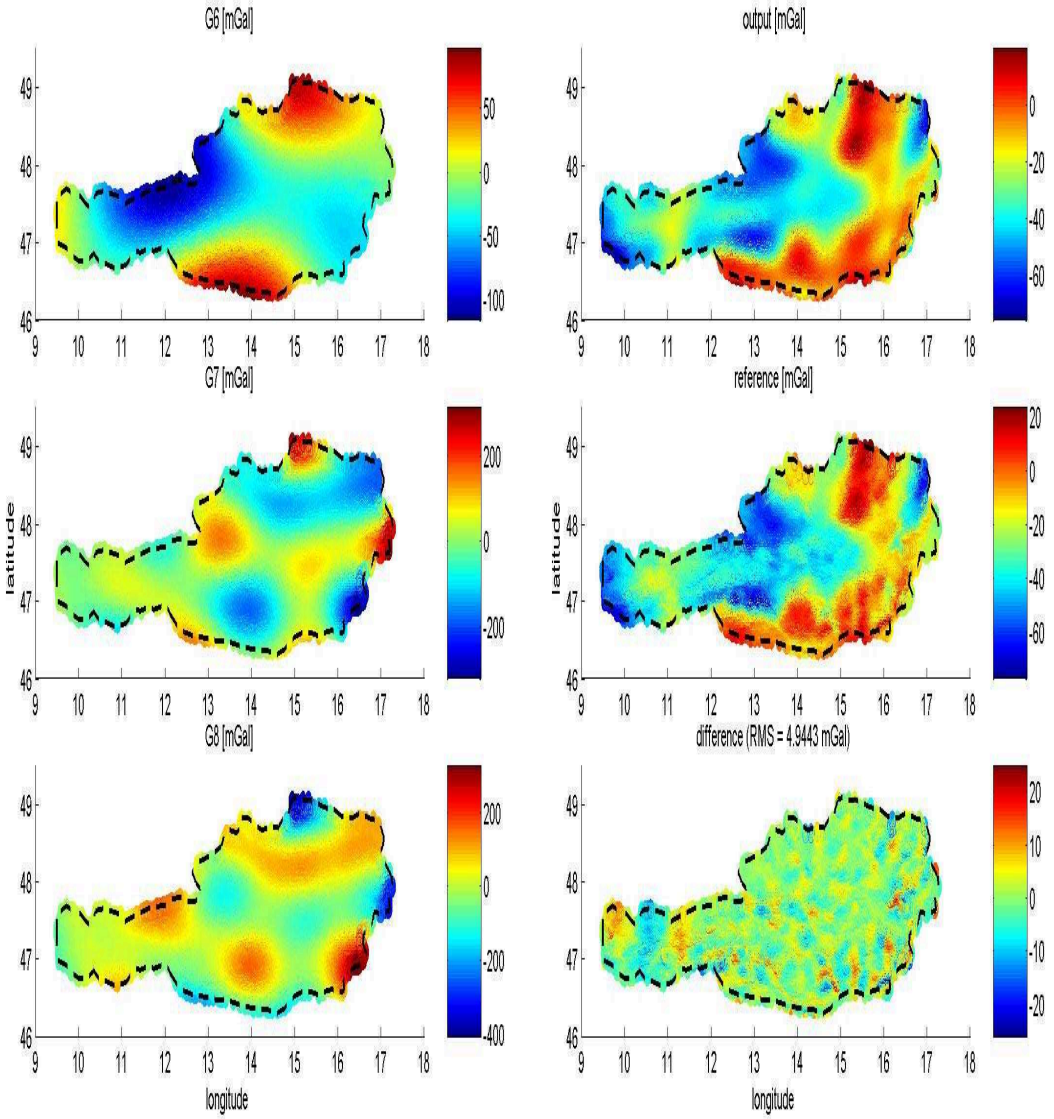

Figure 6.6: Signal reconstruction using 8 levels. Left: detail signals at levels 6, 7, 8; right: reconstructed signal, the reference, and their difference (top to bottom)

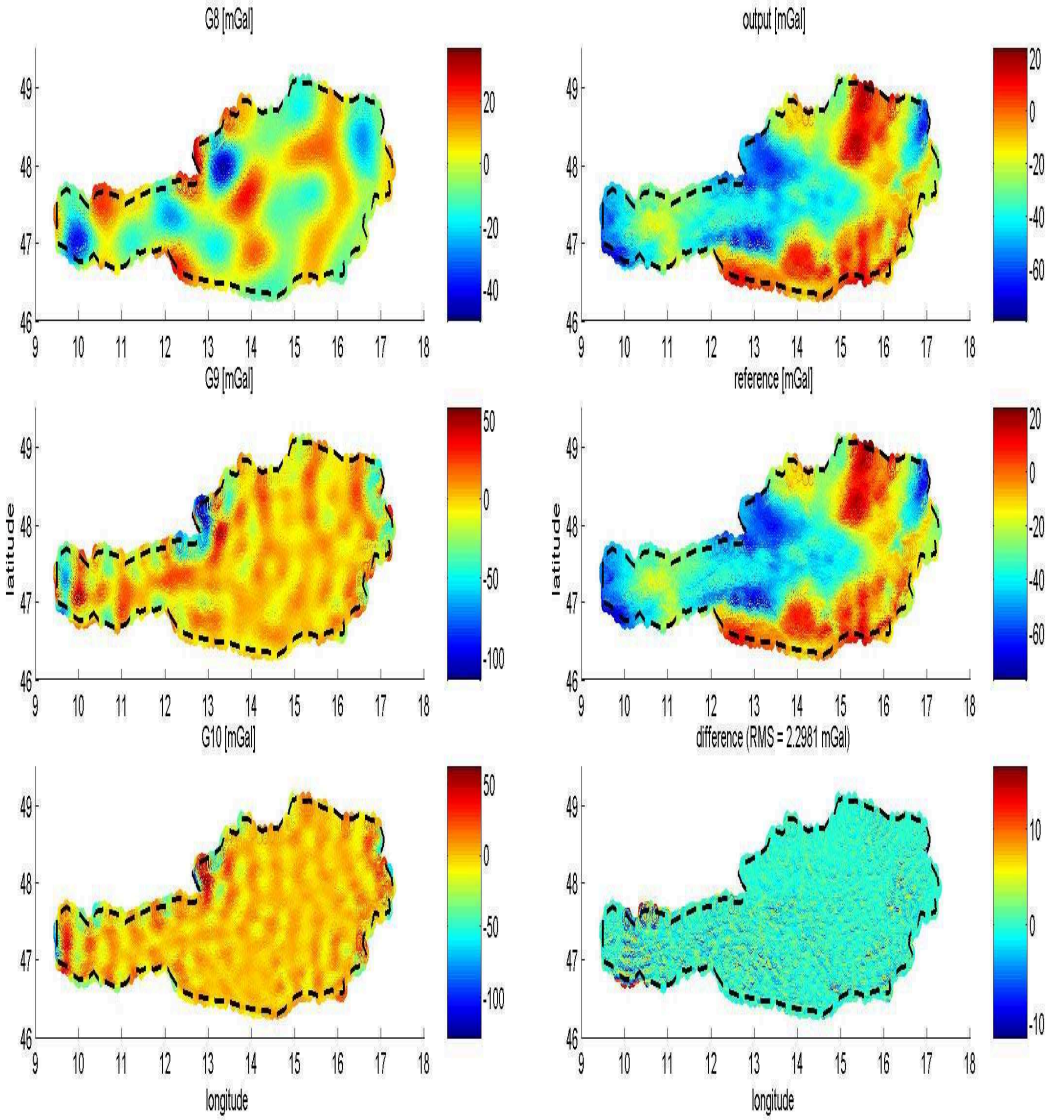

Figure 6.7: Signal reconstruction using 10 levels. Left: detail signals at levels 8, 9, 10; right: reconstructed signal, the reference, and their difference (top to bottom)

Table 6.2: Errors of reconstructed signals (gravity anomalies) when using 6, 8, and 10 levels

Number of levels	Error (rms) in [mGal]
6	8.5
8	4.9
10	2.3

and the reconstructed signal, the original one, and the difference between them (right, top to bottom). Obviously, the more levels are used, the better a reconstructed signal can be obtained. The results summarized in table 6.2 show that the difference between the reconstructed signal and the original one decreases to about 2 mGal when using 10 levels, compared with 5 and 9 mGal in cases of 8 and 6 levels were used.

Regarding to the accuracy of gravity anomaly observations which is conventionally assumed of 1 mGal, the error about 2 mGal (included the error of the MRA process) when using 10 levels is acceptable. Furthermore, the use of 10 levels is also the limit which a standard PC (i.e., 1 GB memory) can handle in this computation scheme due to the fact that the size of the normal equations is proportional to the resolution of the base grid, and in its turn, the grid resolution has to be sufficiently high corresponding to the bandwidth of the signal it represents. Moreover, the amount of gravity anomaly observables in the given data set is barely sufficient for representing signals up to level 11, but does not guarantee the solvability of the normal equations (see the simulation about the data sufficiency in section 4.2.2). Consequently, the set-up of maximum 10 levels is used for the later computations.

Concerning the stabilization of the normal equations, the Tikhonov regularization using Quasi-optimality method is applied for all computations below. Its convenience and reliability were shown in several simulations in chapter 3 as well as during the whole implementation.

6.2.2 Set-up for grids and the long-wavelength component reduction

As mentioned in chapter 4, equiangular grids are the choice for this thesis. Now, what we need is the set up for grid's size and resolution. Because we use 10 levels (harmonic D/O up to 2047 equivalently) for the analysis, the resolution of, at least, $(180^\circ/2047 =)\ 5'16''$ is required for the base grid; and due to the fact that the geographic coordinates of Austria are about from 46.4°N to 49.0°N in latitude and from 9.5°E to 17.2°E in longitude, the base grid is set up as follow:

- Base grid: $37 \times 97 = 3589$ points
  - Latitude: $46.25^\circ\text{N} : 5' : 49.25^\circ\text{N}$
  - Longitude: $9.25^\circ\text{E} : 5' : 17.25^\circ\text{E}$

The input grid (for global data) is a bit extended in comparison with the base grid, and is required to satisfy the condition of data sufficiency (to solve the normal equations). The set up for the input grid is:

- Input grid: $56 \times 111 = 6216$ points
  - Latitude: $45^\circ\text{N} : 6' : 50.5^\circ\text{N}$
  - Longitude: $8^\circ\text{E} : 6' : 19^\circ\text{E}$

For the sake of convenience, the resolution of $6'$ $(= 0.1^\circ)$ is chosen for the output grid. This resolution is also sufficient to display the output signal smoothly. The illustration for this grid is given in figure 6.8.

- Output grid: $36 \times 86 = 3096$ points
  - Latitude: $46^\circ\text{N} : 6' : 49.5^\circ\text{N}$
  - Longitude: $9^\circ\text{E} : 6' : 17.5^\circ\text{E}$

Figure 6.8: 0.1° equiangular output grid

Table 6.3: Errors of reconstructed signals (gravity anomalies) when using global reductions up to D/O 55, 63, and 70

Global reduction up to	Error (rms) in [mGal]
D/O 55	2.3
D/O 63	2.3
D/O 70	2.3

Moreover, for the fitting and checking steps using GPS/leveling data, the 170 positions of GPS/leveling observations are added to the output grid. Hence, the set of output positions actually comprises 3266 points instead of 3096 regular points (of the output grid).

Concerning the long-wavelength components, which should be reduced from data to ensure the appropriate representation of the signal on a local area, the maximum degree of the reduced component can be approximated by $180^\circ/d\varphi$ where $d\varphi$ is the smaller size of the target area. With the base grid set up above ($d\varphi = 3^\circ$), the long-wavelength component up to about D/O 60 should be removed. This number (sixty) is just an approximation. An investigation for three values around 60, which are 55, 63, and 70, is carried out. The third case of the simulation about j_{max} (i.e. $j_{max} = 10$) above is repeated, however, not only D/O 70 but also D/O 55 and 63 are applied. The differences between the reconstructed signals and the original ones for three cases (global reductions up to D/O 55, 63, and 70) are listed in table 6.3. It shows that the errors are the same for all cases, i.e. we can chose any number in that range (from 55 to 70) without considering. For later computations, the value D/O 63 is chosen (partly because of the convenience when using dyadic kernel).

6.2.3 Set-up for data sets and corrections

Here we have three data sources including the (modeled) global geoidal undulations, the gravity anomaly observables, and the GPS/leveling measurements which also are the three major data types in the geoid determi-

nation. Note that the data set of deflections of the vertical, which entered the GEOnAUT solution, was not used due to its limited impact on the final combined solution.

The terrestrial gravity anomaly is the main observation type forming the (regional) geoid as well as contributing to the physical characteristic of this surface. However, the disadvantage of this data source is the lack of high quality information of the earth gravity field in long wavelengths, which requires the complementary information from the global data. This is also one of the main reasons causing the difference between the resulting geoid and the existing set of GPS/leveling points.

The set of GPS/leveling data, due to the fact that it sticks on both geometric coordinate reference system and (physically-derived) national height system, is often used to fit the systematic difference between the computed geoid and the national height system as well as for evaluating the quality of the resulting geoid. Moreover, in the scene of the MRA process, it can be also used as an input data source.

Concerning the global data, in reality, most of EGMs are composite models also including terrestrial data. Therefore, we use the pure satellite model EIGEN-GL04S as the main global input data. EIGEN-GL04S is available up to harmonic D/O 150, we used the maximum D/O of 127 ($= 2^7 - 1$) for the convenience when applying dyadic kernel. Furthermore, due to the limited size of the target region, long wavelengths below harmonic D/O 64 are reduced for all types of data using EIGEN-GL04S.

In summary, we have the following data sets:

- The set of 6216 global geoidal undulations generated from model EIGEN-GL04S using harmonic D/O from 64 to 127, which is represented by the input grid described above.

- The set of 14001 terrestrial gravity anomalies which is global (up to D/O 63) and topographic-isostatic reduced.

- The set of 170 GPS/leveling points is separated into two subsets of 85 points, one for fitting (validating) and one for checking (evaluating) the resulting geoid. Figure 6.9 shows that the scattering distribution (over

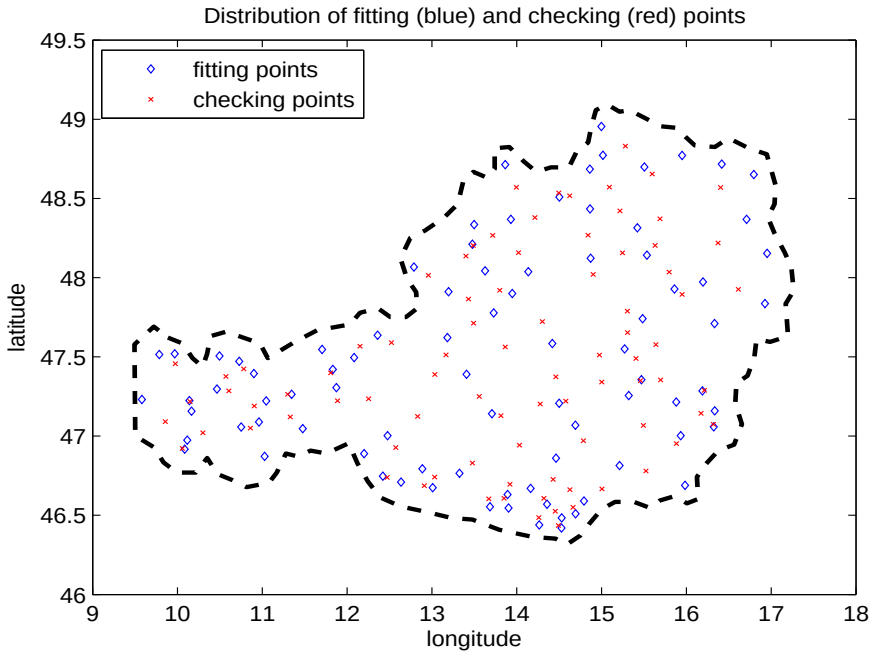

Figure 6.9: Distribution of 85 GPS/leveling fitting points (blue $\diamond$) and 85 GPS/leveling checking points (red $\times$)

Austria) of those two data sets is ensured. Moreover, the whole data set of 170 measurements is used as an input data source in approaches 2, 3, and 4. In analogy to the case of gravity anomaly data, the GPS/leveling data are global (up to D/O 63) and topographic-isostatic reduced.

Concerning the difference between the resulting geoid and the national height system represented by the GPS/leveling observations (so-called the "direct" geoid height measurements), it is attributed to

- the datum inconsistencies, different tidal systems, long-wavelength geoid errors, GPS errors, distortions in the vertical network, and
- the intrinsic non-unique problem of the operator mapping the gravity anomalies into the geoid heights within a local area and vice versa (Prutkin and Klees 2008).

Generally, the first error sources are systematic or long-wavelength characteristic, and can be parameterized by a low-order polynomial (here we call it fitting surface). The second one, caused by the field transformation, has a more sophisticated property. In the scene of the MRA process, a simulation described below shows that, for signals up to harmonic D/O 511, the error of the field transformation has also a long-wavelength characteristic, hence can be implicitly included in a low-order polynomial which is used for the fitting correction. For signals at very high frequency bands, an idea is to construct a non-trivial function which is harmonic in the neighborhood of the target area and has an almost zero gravity anomaly signal over the target data, then its non-zero potential signal is the correction for the field transformation error, see Prutkin and Klees (2008) for more details.

Simulation: The harmonic coefficients of model EGM2008 up to D/O 511 are used to generate the values of gravity anomalies as well as geoidal undulations for 14001 positions of the local input data set (see above). The MRA process is applied for these gravity anomalies to compute the geoidal undulations for the same 14001 positions. The differences between these computed values and the generated ones indicate the error of the field transformation. Afterwards, these differences (14001 values) are projected onto the output grid (3096 points) also using the MRA process (without field transformation). The result is plotted in figure 6.10. These values can be used as a simple model for the field-transformation correction in the MRA process. Figure 6.10 shows the long-wavelength characteristic of this simple correction model, so it may be also included in the low-order polynomial used for the fitting surface. However, in the computation of all approaches below, this field-transformation correction is applied separately with the fitting surface due to the intrinsic difference between them. See figure 6.16 for the illustration about the field-transformation correction for each level. Note that this correction is applied for all approaches but exemplarily mentioned in approach 1.

Concerning the fitting correction, this is the required step to fit the computed geoid to the nation height system represented by GPS/leveling points. Here we use a set of 85 GPS/leveling points (figure 6.9) for this purpose. The

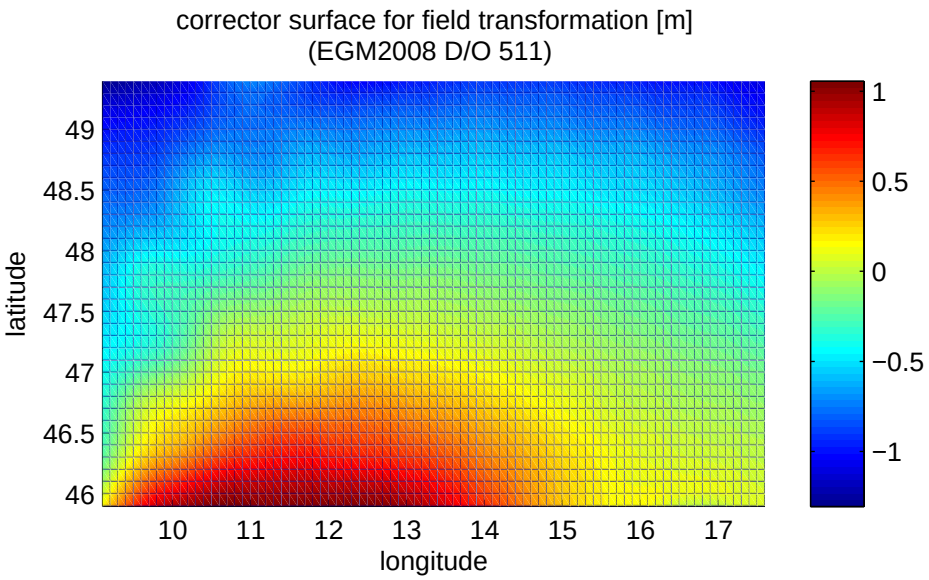

Figure 6.10: Correction for Δg-to-N transformation (EGM2008 D/O 511)

85 values of differences between this fitting data set and the computed geoid are used to estimate the coefficients of a third-order polynomial using the least-squares adjustment

$$\boldsymbol{f} = (A^T A)^{-1} A^T \boldsymbol{y}_{85} \tag{6.1}$$

where $\boldsymbol{f}$ is the vector of 10 coefficients of the polynomial, $\boldsymbol{y}_{85}$ is the vector of 85 values of differences, and A is the design matrix.

The covariance matrix of $\boldsymbol{f}$ is also obtained by

$$\Sigma(\boldsymbol{f}) = (A^T A)^{-1} \sigma^2 \tag{6.2}$$

where σ^2 is the variance factor of $\boldsymbol{y}_{85}$.

Then all correction values for the output-grid points and their corresponding estimated errors can be computed according to

$$\boldsymbol{y} = A\boldsymbol{f} \tag{6.3}$$

and

$$\Sigma(\boldsymbol{y}) = A\Sigma(\boldsymbol{f})A^T \ . \tag{6.4}$$

Recalling equation (5.16), the final estimated error of the output signal σ_{out} now can be obtained by

$$\sigma_{out}^2 = \sigma^2 + \sigma_{fit}^2 \tag{6.5}$$

where σ_{fit}^2 are the main diagonal elements of $\Sigma(\boldsymbol{y})$.

For the evaluation, a set of 85 GPS/leveling checking points is used. The root mean square (rms) value of 85 differences indicates the inconsistency between the resulting geoid and the "direct" geoid represented by GPS/leveling measurements. Remind that these 85 checking points and the 85 fitting points mentioned above are two subsets of the given set of 170 GPS/leveling observations. Moreover, for a comparison with the reference solution GEOnAUT, the 164 mutual points (inside Austria) of two output grids are picked up, and the rms of these 164 differences represents the inconsistency between two geoid solutions. The 164 checking points used to compare with GEOnAUT are the mutual points between the output grid set up at section 6.2.2) and the output grid of GEOnAUT. After excluding points on (or very close to) the border, we get 164 mutual points of those two output grids inside Austria. The distribution of these 164 positions is displayed in figure 6.11. The comparison between the solutions of approaches and GEOnAUT is present in section 6.9.

6.2.4 Set-up for the combination scheme

As mentioned before, the local data (terrestrial gravity anomalies) are the main effort in the regional geoid determination work; however, in order to take full advantage of the long-wavelength information of global data, a global-local data combination should be carried out.

For the global-local data combination, the simplest way is choosing a turning point (e.g., a certain degree and order when using harmonic coefficients) where the upper part is the domain of local components and the lower one purely uses the global data. This separating point usually belongs to the long-to-medium wavelengths; however, it is not easy to define exactly where the border should be. Any answer is more or less forced. So, instead of an exact border separating areas of global and local components, a (buffer-

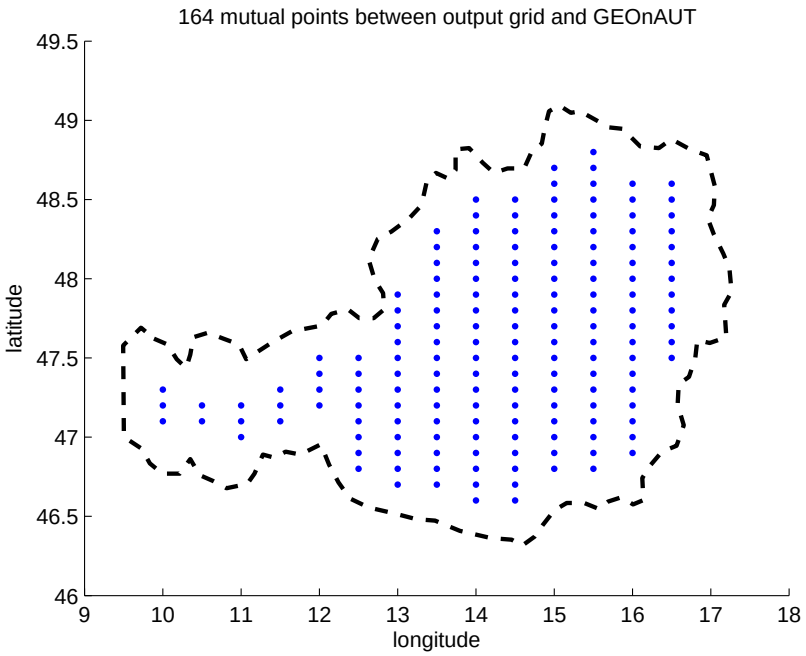

Figure 6.11: Distribution of 164 mutual points between output grid and GEOnAUT for checking

ing) combination zone where the impact of the global component gradually decreases corresponding to the increase of the local component's contribution seems to be more flexible and reasonable. The frequency band of the combination also should belong to the long-to-medium wavelengths. In this thesis, the combination is carried out for the frequency range of 64 to 127 harmonic degrees. The key problem in this solution is the adequate (combination) weighting for the global and local components; see chapter 5 for more details about this issue.

The GPS/leveling data, beside their role of the reference set for fitting and checking the computed geoid, can theoretically be used as an independent input data source. However, the very strong requirement in the frame of MRA is that the number of GPS/leveling measurements have to be dense enough (i.e. equivalent to the resolution of the base grid, at least) which is almost never satisfied in practice because of the expensive cost for the GPS/leveling measurement. Hence, in order to use this type of data as input data, the GPS/leveling points have to be merged into a larger input data set, i.e. the 6216 global undulations or the 14001 terrestrial gravity anomalies. The latter approach is impossible, at least in the scene of this MRA process, due to the different types of data (height vs. gravity); so the possible way is to merge the GPS/leveling data into the global data set. The problem here is the inconsistency of the frequency band; i.e., while the global data contain only the long to medium wavelength information, the GPS/leveling data include the shorter wavelength components. When putting them into the same basket, we have to use the same (wavelet) functions. Due to the maximum harmonic degree and order of the global data is up to 127 (equivalent to level 6), we have two choices here: process all (the global and GPS/leveling data) up to level 6 (i.e. ignore the frequency part higher than D/O 127 of the GPS/leveling data), or up to the higher levels (in this thesis is level 10, equivalent to D/O 2047) to use the more detail information of the GPS/leveling data with the assumption that the lack of information of many global data points in this frequency range (from level 7 to level 10) does not effect to the MRA process.

In summary, we have the following combination schemes:

- Using the reduced data of 14001 gravity anomalies and 170 GPS/leveling observables (topographic-isostatic reduced including indirect effect, and global up to D/O 63 reduced), and 6216 global geoidal undulations (D/O from 64 to 127):
  - 14001 gravity anomalies analyzed to 10 levels combine with 6216 global geoidal undulations analyzed to 6 levels;
  - 14001 gravity anomalies analyzed to 10 levels combine with a set of 6216 global geoidal undulations and 170 GPS/leveling points analyzed to 6 levels;
  - 14001 gravity anomalies analyzed to 10 levels combine with a set of 6216 global geoidal undulations and 170 GPS/leveling points analyzed to 10 levels:
    - using the combined spectral-stochastic weighting as all other approaches, and
    - no weighting (i.e. using level 6 as the ”turning point”).
- Free-air data without topographic-isostatic reduction, only global reduction up to D/O 63: 14001 gravity anomalies analyzed to 10 levels combine with 6216 global geoidal undulations (D/O from 64 to 127) analyzed to 6 levels.

Table 6.4 summarizes all computation schemes which will be carried out later on. The first four are the different approaches of data combination for a geoid solution. The last one which uses the non-reduced data should be counted as an investigation into how MRA deals with extremely high-frequency signals more than a geoid solution, since it is not completely correct from a theoretical point of view if one computes geoidal undulations disregarding masses between the terrain surface and geoid.

Before presenting these approaches, an overview of the reference solution, the Austrian Geoid 2007 (GEOnAUT), will be given in the next section.

6.3 Reference solution: GEOnAUT

This section consists of parts from the paper of Pail et al. (2008).

Table 6.4: Computation approaches

No	Global data (EIGEN-GL04S)	GPS/leveling as input data	j_{max} global	Reductions for Δg and GPS/leveling	Weighting method
1	D/O 64 to 127	no	6	global up to D/O 63 topographic-isostatic indirect effect	spectral-stochastic
2	D/O 64 to 127	yes	6	global up to D/O 63 topographic-isostatic indirect effect	spectral-stochastic
3	D/O 64 to 127	yes	10	global up to D/O 63 topographic-isostatic indirect effect	spectral-stochastic
4	D/O 64 to 127	yes	10	global up to D/O 63 topographic-isostatic indirect effect	none
5	D/O 64 to 127	no	6	global up to D/O 63	spectral-stochastic

Overview

In the framework of the project "The Austrian Geoid 2007" (GEOnAUT), funded by the Austrian Research Promotion Agency, a new Austrian geoid solution has been computed (Pail et al. 2008). Compared to the existing Austrian geoid model, the accuracy could be significantly improved mainly due to the substantially enhanced quality of the input data. A new digital terrain model (DTM) has been assembled as a combination of highly accurate regional DTMs of Austria and Switzerland, complemented by data of the Shuttle Radar Topography Mission (SRTM) in the neighboring countries. Since SRTM reflects the surface heights, a correction using Corine Land Cover (CLC90) data has to be applied to transform to terrain heights. In addition to a thoroughly validated database of gravity anomalies and deflections of the vertical, new measurements of deflections of the vertical in the South-East of Austria as well as GPS/leveling information have been incorporated. Finally, these terrestrial data have been combined with global gravity field information represented by a recent GRACE gravity field model, leading to a significantly improved representation of the long to medium wavelength of the solution. Several strategies for the optimum combination of different (global and local) data types, including optimum weighting issues, have been investigated. For the final geoid solution, the least-squares collocation (LSC) technique, representing the most frequently used approach, has been selected. The new geoid solution, including covariance information, has been thoroughly validated both internally and externally.

The first steps were the pre-processing of the terrestrial gravity data, the assembling of an enhanced digital terrain model. In parallel, several methods for the optimum combination of these different data types have been investigated, analyzed, assessed, and compared:

- tailored series expansions (based on spherical harmonic base functions,
- multi-resolution analysis and spherical wavelet techniques,
- least-squares collocation,
- fast multipoles approach and algebraic approximation methods.

After a thorough assessment of these methods, finally the LSC approach turned out to be the currently most mature technique to be applied for the final Austrian geoid solution. The final output product, a new Austrian geoid solution, is complemented by corresponding error estimates.

Input data

Summarily, the input data consist of:

- gravity anomalies (14001 stations, approximate 4×4 km average distance),
- deflections of the vertical (672 stations),
- GPS/leveling observations (161 stations),
- global gravity field EIGEN-GL04S (complete to D/O 70), and
- a highly accuracy DTM with the resolution of 44×49 m for Austria and Switzerland, complemented by data of SRTM (applied a correction using CLC90) in neighboring countries.

Geoid computation

The final geoid solution was computed using the remove-restore technique. The basic idea is to remove the long-wavelength gravity field effect represented by the global gravity field model (EIGEN-GL04S), and the high frequency signals, which are mainly related to topography, by a topographic-isostatic reduction (Airy-Heiskanen model with a density of $2670\,\mathrm{kg/m^3}$).

The remove step results in smoother signals of the form

$$\beta_{red} = \beta - \beta_{glo} - \beta_{TI} - \beta_{ind} \tag{6.6}$$

where β can be any derived quantity of the gravity potential, e.g., gravity anomalies, deflections of the vertical, or geoid heights. Starting from the free-air quantity β, the following reductions are applied: global gravity field model reduction β_{glo}, topographic-isostatic reduction β_{TI}, including the indirect effect β_{ind}, which copes with the change in the potential due to the mass

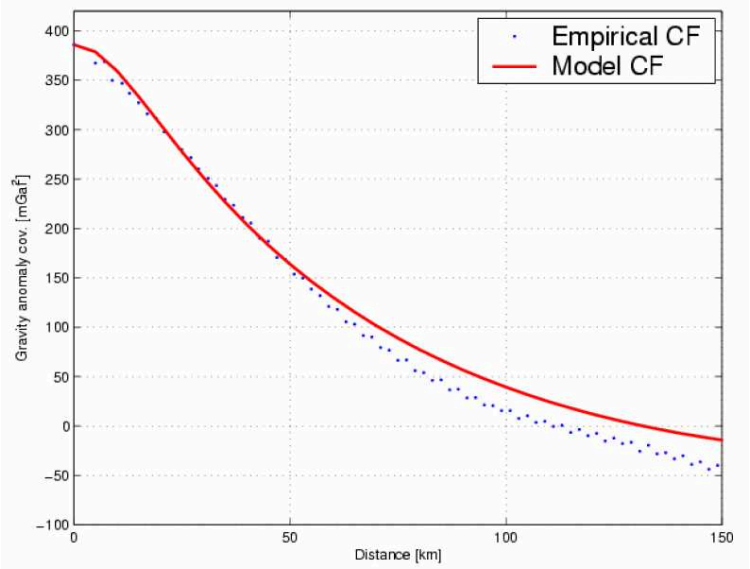

Figure 6.12: Empirical covariance function (blue dots) and model covariance function (red solid line) (source: Pail 2007)

redistribution related to the topographic reduction β_{TI}. After the reduction procedure, β_{red} refers to the co-geoid.

The reduced gravity anomalies have been used to derive an empirical covariance function (ECF) and to adapt the parameters of the analytical Tscherning-Rapp covariance function model. The locally adapted parameters here are $A = 332.453\,\mathrm{mGal}^2$, $B = 24$, $s = \left(\frac{R^2}{r_i r_j}\right) = 0.998724$, and n starts from 71 (refer to equations (2.40) and (2.42) in chapter 2). Figure 6.12 shows the empirical covariance function (blue dots) as well as the adapted local Tscherning-Rapp model (red solid line). Herein the variance of the residual gravity anomaly field is $385\,\mathrm{mGal}^2$, the correlation length is about 42.6 km.

Concerning the restore procedure, the correction terms of equation (6.6) were evaluated for the predicted geoidal undulations, defined on a regular

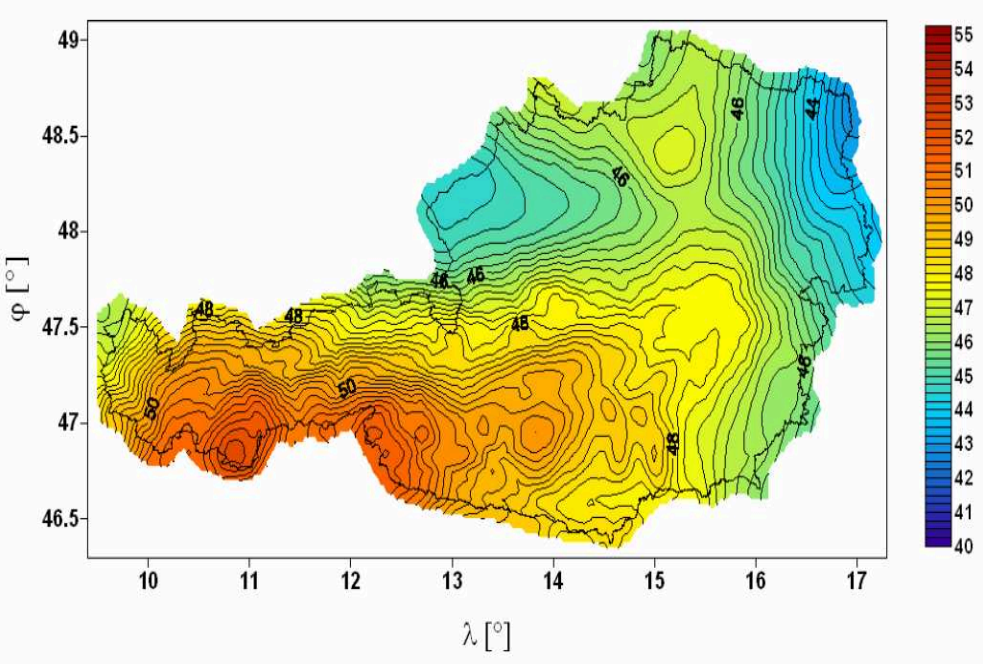

Figure 6.13: The Austrian Geoid 2007 (source: Pail 2007)

$3' \times 3'$ grid, and finally they were added to the LSC output.

Final result

The final solution for the Austrian Geoid 2007 is shown in figure 6.13; and figure 6.14 displays its corresponding error estimates being of the order of 2 to 3 cm.

Due to the fact that the data used for following approaches of MRA method are almost the same with data of GEOnAUT, so the result of each approach will be compared to the GEOnAUT solution as a reference, beside the main

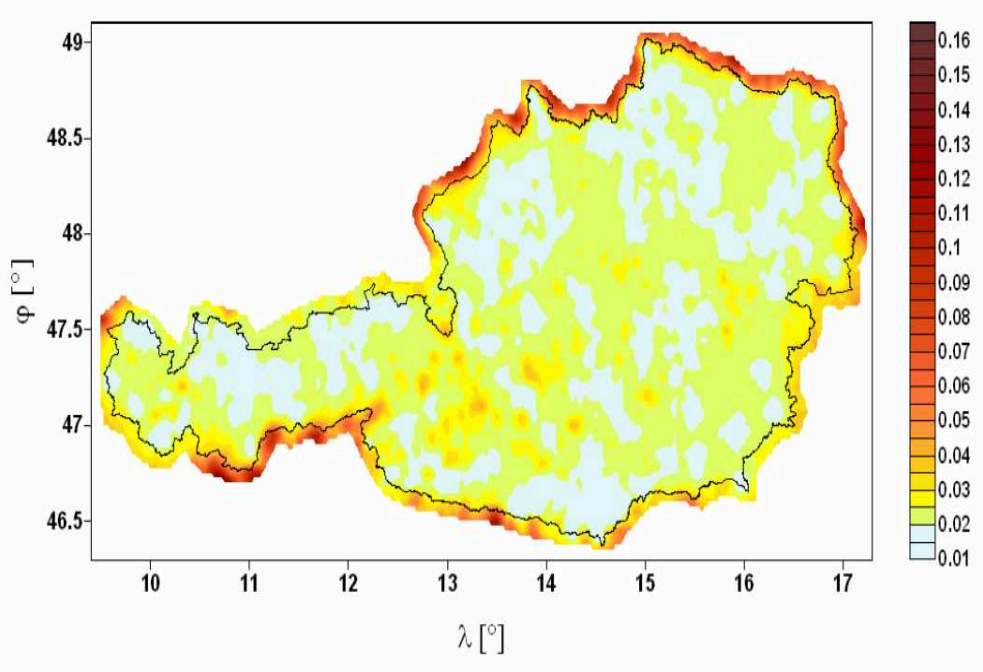

Figure 6.14: The Austrian Geoid 2007: error estimates (source: Pail 2007)

evaluation using the set of 85 GPS/leveling checking points.

6.4 APPROACH 1

For all five approaches, the complete procedure, in which, the MRA process plays the core, is carried out to obtain the geoid solution from the gravity data sources. The main steps comprise:

- The scale coefficients are computed for the global and local data.
- Thanks to scale coefficients, each data source is analyzed into individual levels (of detail signals).
- The individual signals are combined according to the combined weighting method, then the output signal is synthesized. In this step, the field-transformation correction is also applied.
- The validation is performed using the set of 85 GPS/leveling fitting points.
- After the validation step, the solution is obtained in accompany with the error estimation.
- The evaluation is performed using the set of 85 GPS/leveling checking points. Besides, the solution is also compared with GEOnAUT as a reference.

It is should be noted that the solutions of all approaches (except approach 5) do not include the reduction restore. It does not mater due to the fact that all reductions are the same for data sources as well as the sets of fitting and checking points.

In this first approach, the procedure is presented step by step, the related equations are also referred to. For remaining approaches, the description is briefed due to the similarity of the computation steps.

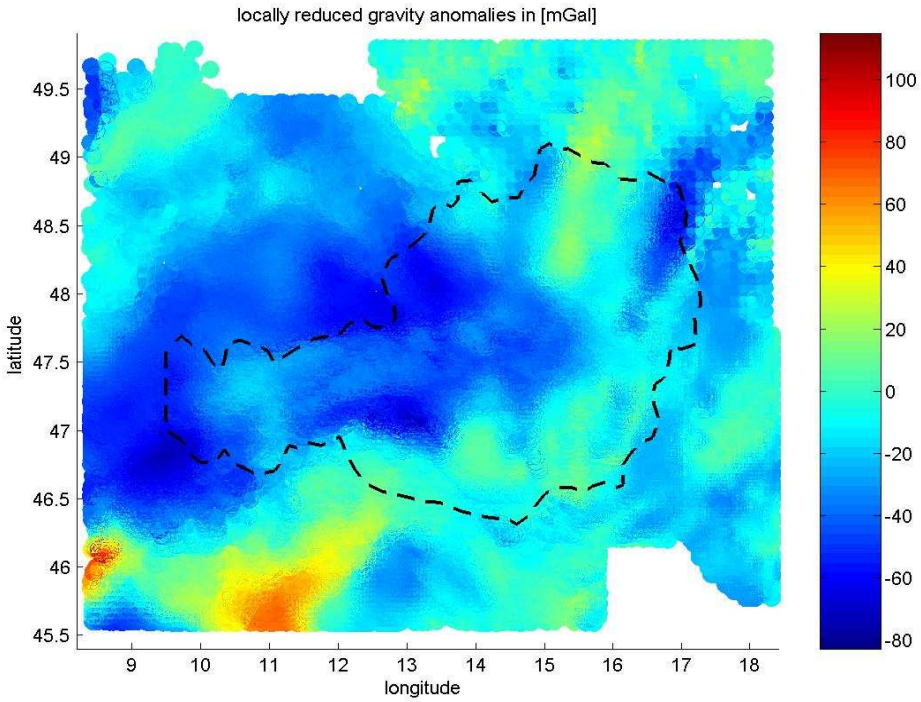

Figure 6.15: 14001 reduced gravity anomalies (reductions: global, topographic-isostatic, and indirect effect)

Local data The local input data consist of the 14001 gravity anomalies (including reductions: global reduction up to D/O 63 using EIGEN-GL04S, topographic-isostatic reduction and the indirect effect) displayed in figure 6.15.

The MRA process introduced in chapter 2 is applied to the local data. At first, the scale coefficient vector is estimated according to equation (2.74). Afterwards, the analysis step is performed using the value $j_{max} = 10$. As figured out in section 6.2, 10 levels are quite sufficient to represent this reduced data set. The individual signals are obtained using equation 2.71. Here the field transformation (Δg to N) is required, so the design matrix in equation (2.74) is computed according to equation (2.79) instead of (2.49).

Figure 6.16 illustrates the individual signals (after field transformation) at levels 6, 7, 8 (left), and their field-transformation corrections (right), re-

spectively. The computation of field transformation correction is described in section 6.2.3.

Global data The global data is the geoidal undulations using harmonic coefficients from D/O 64 to 127 of the model EIGEN-GL04S. It is illustrated in figure 6.17. Due to the frequency band limit of the input signal (D/O up to 127), the value $j_{max} = 6$ is used. After estimating the scale coefficients, the global data are analyzed to six levels. Figure 6.18 displays the global signal at level 6 where the combination of globally and locally detail signals is performed.

Combination and solution The combination is performed using the spectral-stochastic weighting method (c.f. chapter 5). The value of 1 mGal is assumed for the accuracy of terrestrial gravity anomalies. The stochastic property of the (modeled) global geoidal undulations, which are generated from equation (2.5), can be obtained according to

$$N = R \sum_{n=2}^{n_{max}} \left(\frac{R}{r}\right)^{n+1} \sum_{m=0}^{n} \overline{P}_{nm}(\cos\theta) \left(\overline{C}_{nm}\cos(m\lambda) + \overline{S}_{nm}\sin(m\lambda)\right) = AX \quad (6.7)$$

$$\Rightarrow \; \Sigma(N) = A\Sigma(X)A^T \quad (6.8)$$

where X and $\Sigma(X)$ are harmonic coefficients $\left\{\overline{C}_{nm}, \overline{S}_{nm}\right\}$ and their variances $\left\{\delta\overline{C}^2_{nm}, \delta\overline{S}^2_{nm}\right\}$, respectively, A is the design matrix whose elements contain $\left\{R \cdot \overline{P}_{nm}(\cos\theta) \cdot \cos(m\lambda), R \cdot \overline{P}_{nm}(\cos\theta) \cdot \sin(m\lambda)\right\}$.

The combined individual signals at levels 6, 8, the residuals are exemplarily illustrated in first three plots of figure 6.19. The synthetic signal is obtained by summing all individually combined signals that are already included the field-transformation correction. This output signal of the MRA process is illustrated in the last plot (bottom-right corner) of figure 6.19. Note that the field-transformation correction is applied for all next approaches without repeating; i.e., the synthetic output signal is already included this correction term before the validation step.

The output signal requires the validation using the set of 85 GPS/leveling fitting points (c.f. section 6.2). The difference between the output signal

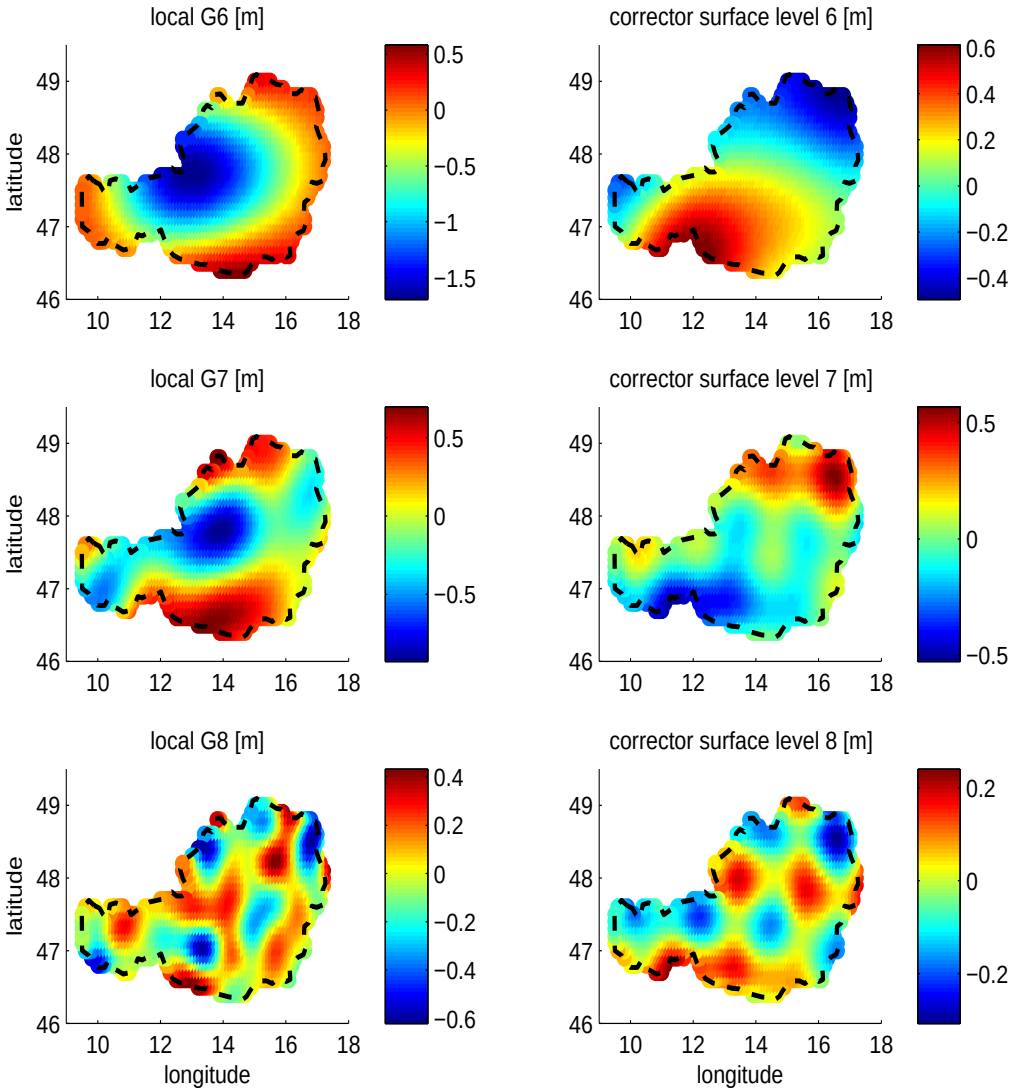

Figure 6.16: Top to bottom: local individual signals at levels 6, 7, 8 (left) and their field-transformation corrections (right)

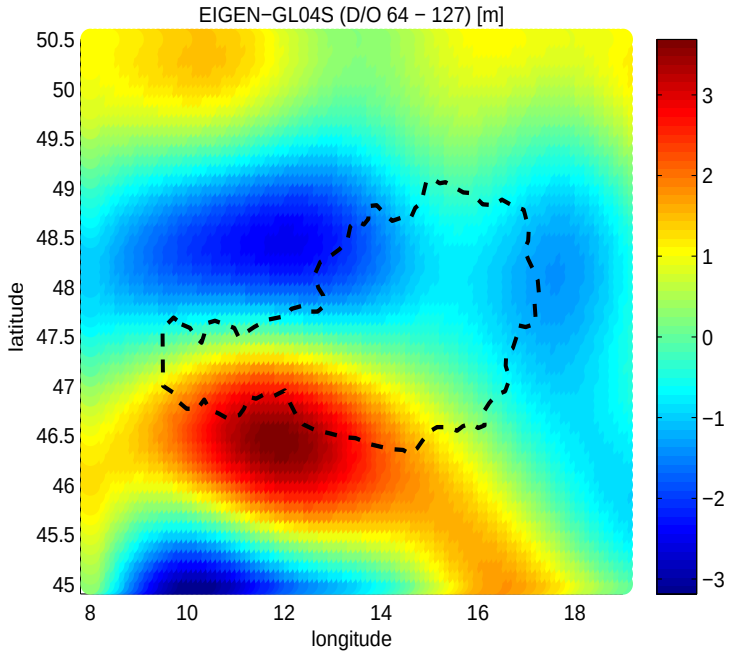

Figure 6.17: Global input data: geoidal undulations in meter (EIGEN-GL04S D/O 64 to 127)

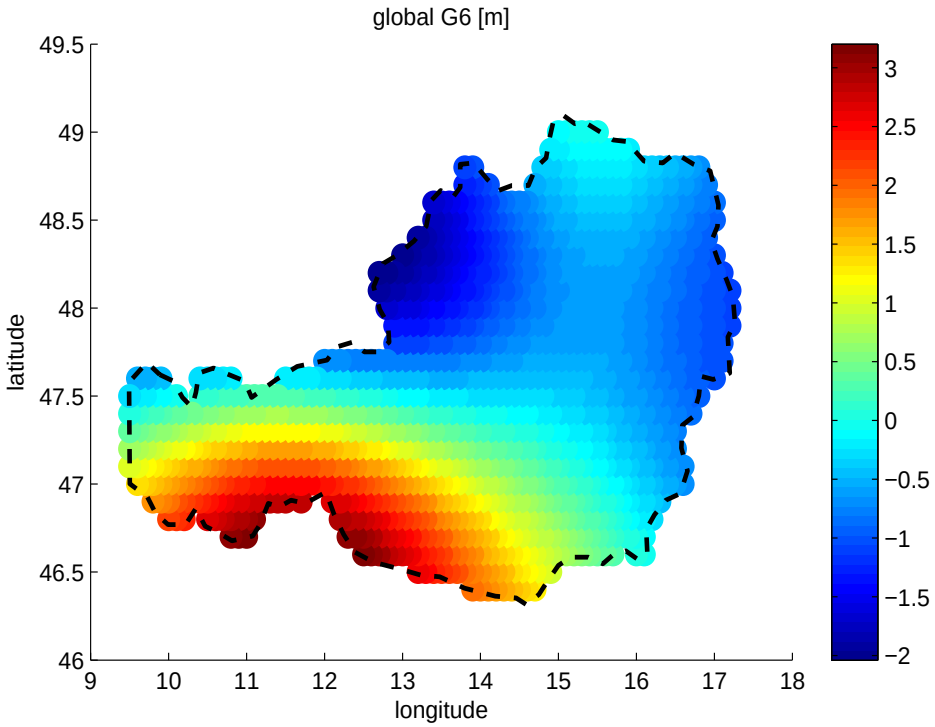

Figure 6.18: Globally detail signal at level 6

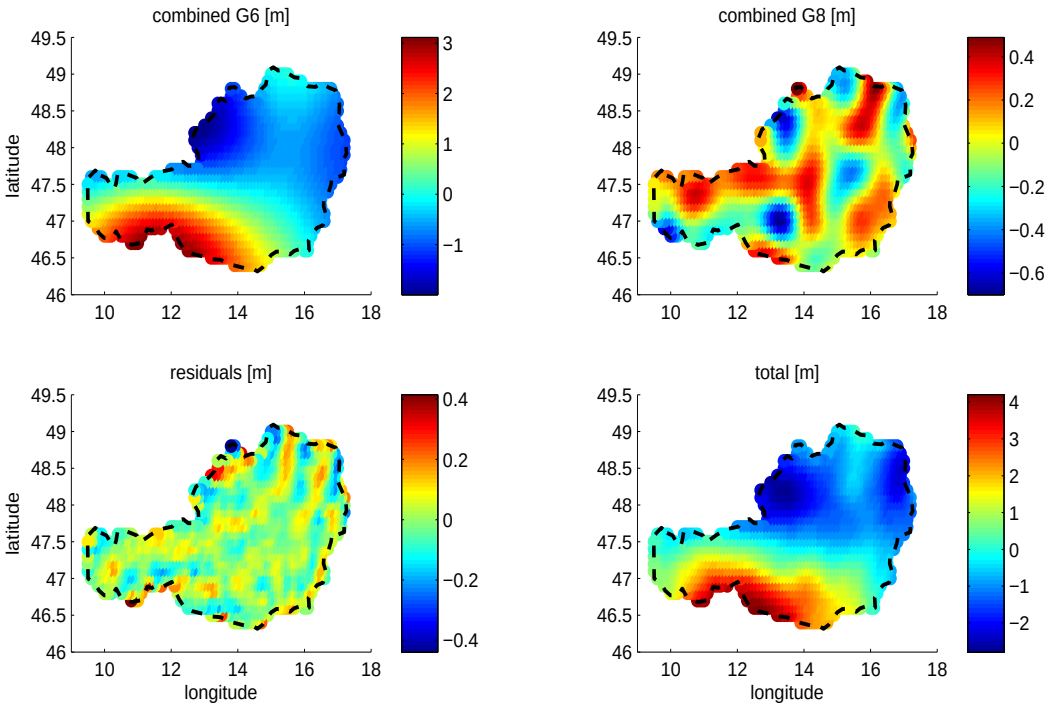

Figure 6.19: Approach 1: combined signals at level 6 (top-left), level 8 (top-right), the residuals (bottom-left), and the total signal (bottom-right)

and the fitting data set is illustrated in figure 6.20 (top). These values of differences are used to parameterize a 3^{rd} order polynomial, and in turn, the polynomial is used to estimate the fitting values for all output points (equations (6.1) and (6.3)). This fitting surface is displayed in the bottom of figure 6.20.

After applying the fitting values, the output is obtained. Note that the actual geoid solution is only obtained after restoring all reductions performed beforehand: the global reduction, the topographic-isostatic reduction, and the indirect effect. However, the output solutions in the context of these approaches do not include the reduction restores mentioned above, due to the fact that, the same reductions applied for gravity data are also applied for two subsets of GPS/leveling fitting and checking data. Therefore, the validation and evaluation steps can be carried out without the requirement to restore the reductions.

The output solution of approach 1 is plotted in the top of figure 6.21. It is accompanied by the error estimates plotted in the bottom of the same figure. This error model is estimated by applying the law of error propagation for all input data sources and through the computation process according to equations (6.5), (5.16), (5.15), (5.5), and (5.4) . Figure 6.21 points out that the error estimates are at the order of 3 to 5 cm in general but go down significantly toward the borders. These values only reflect the stochastic errors, for the actual accuracy, the evaluation step is required.

The evaluation which uses the set of 85 GPS/leveling checking points shows that the solution of this approach 1 differs from the checking data about 12 cm in root mean square (figure 6.22), wherein the largest values gather to the alpine area at the West. The twelve-centimeter error is much larger than the error estimation (just about 5 cm) which should be counted as the expected precision of the output (excluding the systematic bias) if all procedures work perfectly. This inconsistency expresses that there may exist a systematic error source within the MRA process which increases the error up to 12 cm. This remarkable value requires a reasonable explanation. Due to the fact that, firstly, MRA process works perfectly in the example of section 2.8 where the Δg-to-N transformation is performed at long wavelengths (D/O up to 10), and secondly, it also works well in the simulation at section

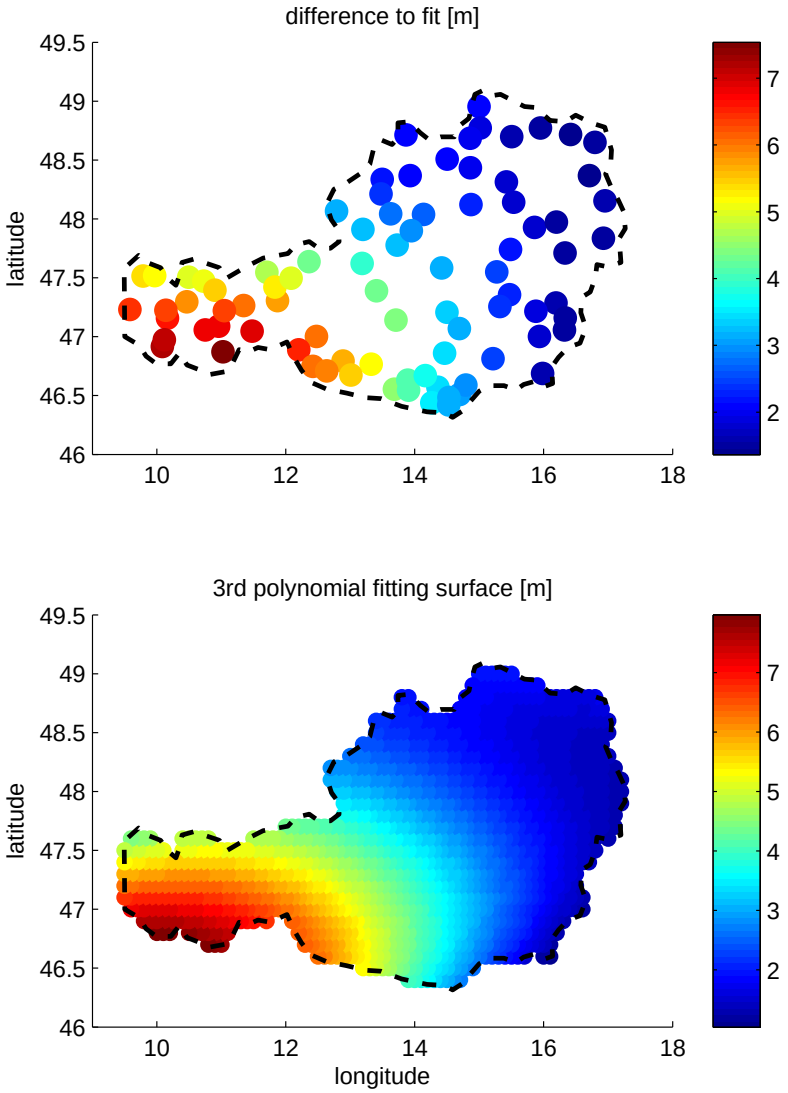

Figure 6.20: Approach 1: differences from 85 GPS/leveling fitting points (top) and the 3^{rd} order polynomial fitting surface (bottom)

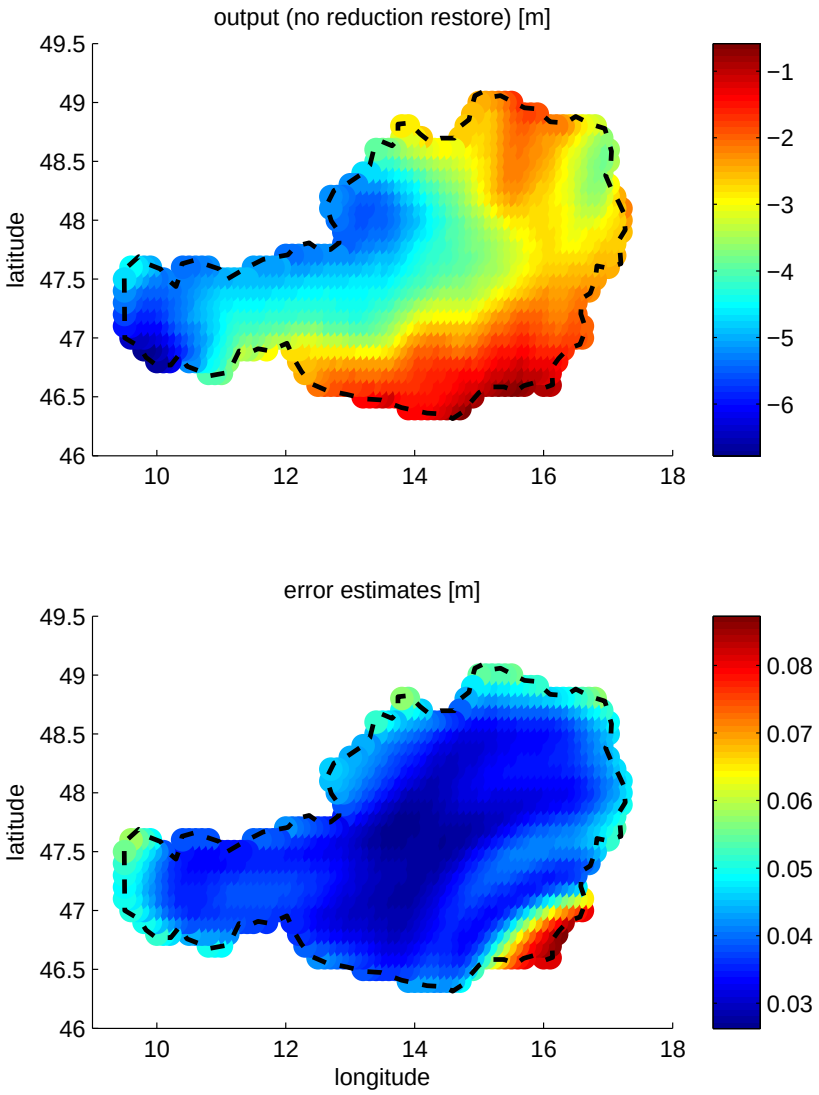

Figure 6.21: Approach 1: the output signal (top) and the error estimates (bottom)

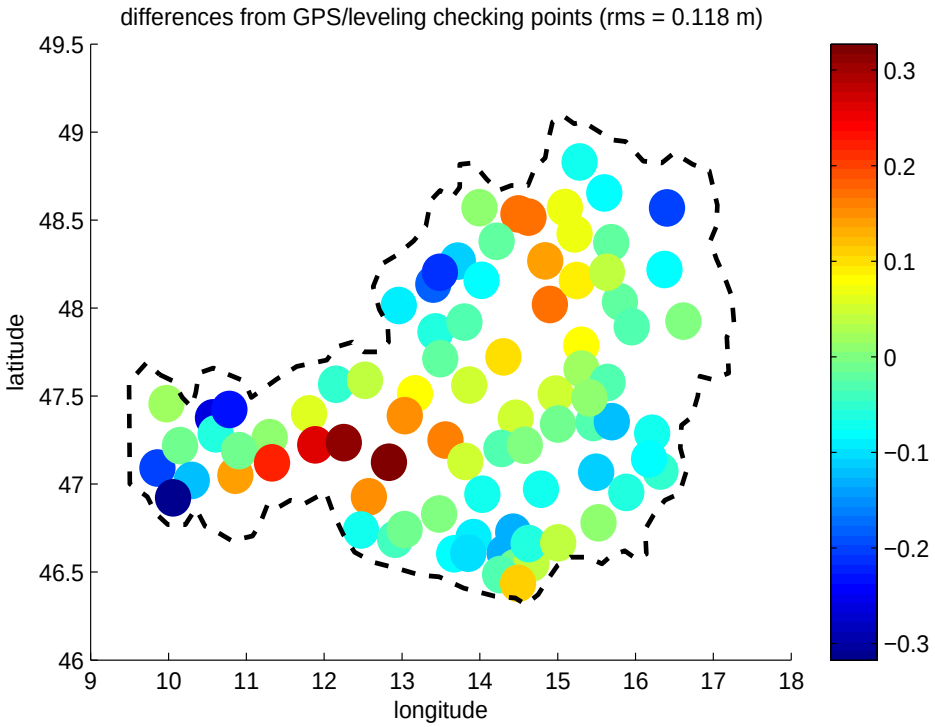

Figure 6.22: Approach 1: differences from 85 GPS/leveling checking points

6.2.1 where the gravity anomaly quantity Δg is reconstructed using 10 levels (the neglect of higher frequencies causes an error of 2.3 mGal by itself as pointed out in that simulation), the possible explanation is that the inadequate performance of the field transformation (in the scene of the MRA process) at short wavelengths causes the main part of this 12 cm error.

6.5 Approach 2

The GPS/leveling points are usually used for validating and evaluating the resulting geoid. Besides, they may also be used as an input data source. Due to the quantity of the observables, the set of GPS/leveling points is not dense enough for being an independent data source for MRA. It also cannot be a part of the local input data because of the data inconsistency (heights vs. gravity anomalies). So in the scene of this thesis, it is merged into the global data. Here is the problem. While the global input data are generated at the range of long-to-medium wavelength (harmonic D/O up to 127), the GPS/leveling points are the observables having a higher frequency characteristic (not limited by the D/O 127). This raises the question that how to treat them in the same basket; or in other words, which levels should be used to analyze them. If we analyze up to level 6, i.e. based on the harmonic D/O 127 of the global data, we cannot use the whole signals of the GPS/leveling data set (the short-wavelength components will be ignored). If we add higher levels (than 6) to use the information content of the signals of the GPS/leveling data set, the problem occurs with the global data when they cannot be represented properly at high levels. In this approach, the case of using 6 levels is carried out.

Now, the input data set of geoidal undulations includes the global model (EIGEN-GL04S D/O 64 to 127) and 170 GPS/leveling observations. Both are analyzed up to level 6. The individual signal at level 6 are illustrated in figure 6.23. In comparison with figure 6.18, figure 6.23 is similar, due to the fact that the GPS/leveling data only contribute a part of signals. The difference will become remarkable when the GPS/leveling information is used up to level 10 (approach 3).

The local data set of gravity anomalies is the same as in approach 1.

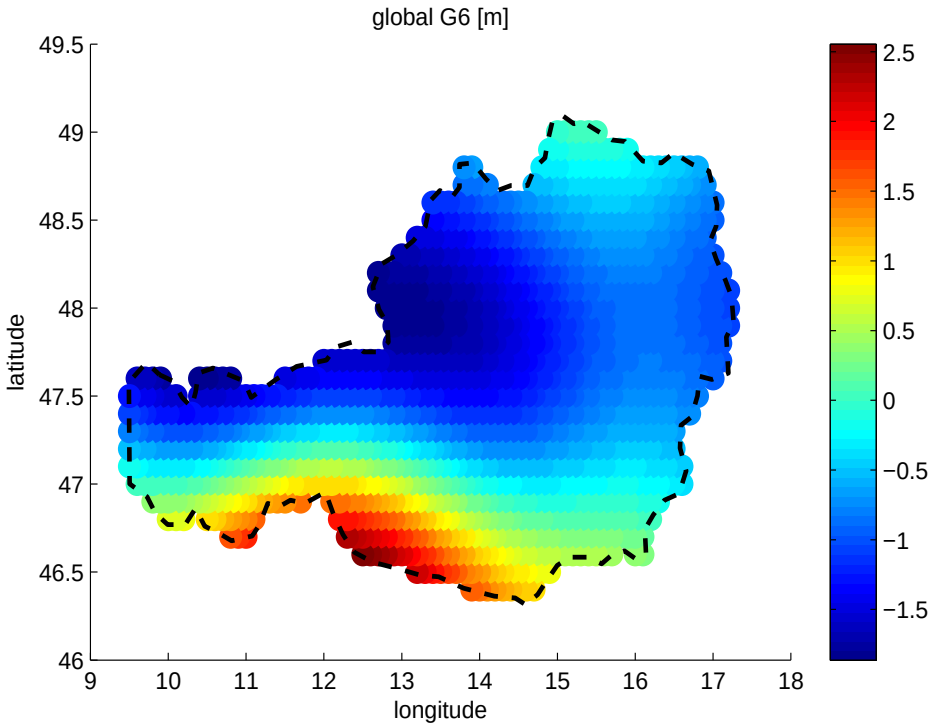

Figure 6.23: Approach 2: Globally detail signal at level 6

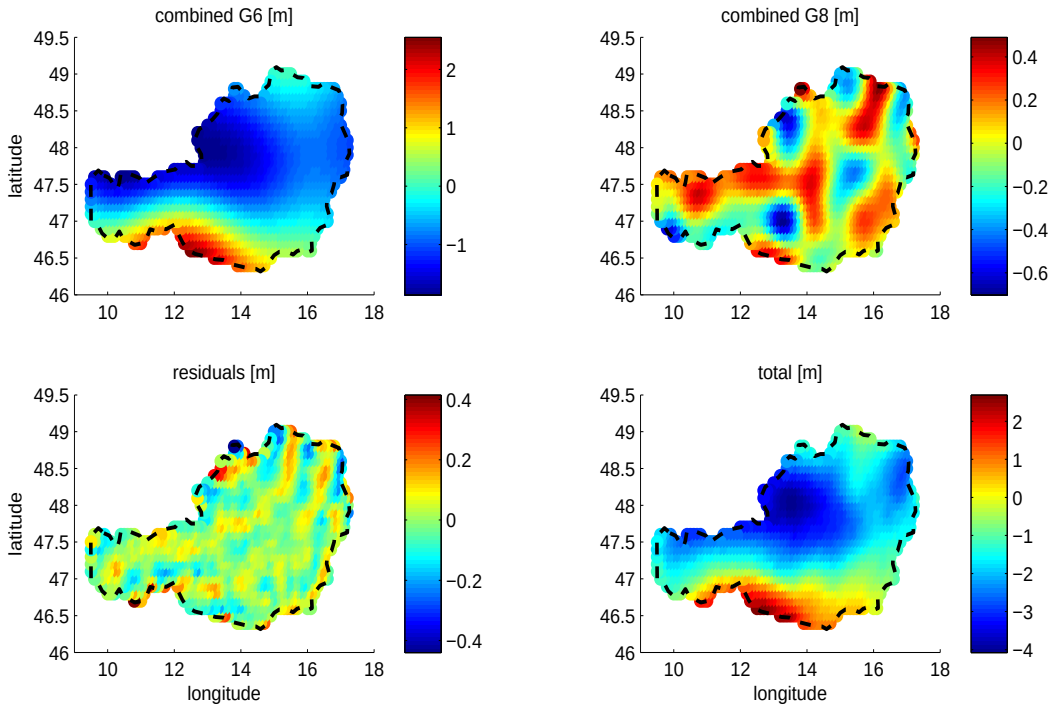

Figure 6.24: Approach 2: combined signals at level 6 (top-left), level 8 (top-right), the residuals (bottom-left), and the total signal (bottom-right)

The combined signals are obtained using the spectral-stochastic weighting method and are plotted in figure 6.24, exemplarily for level 6 (top-left), level 8 (top-right), and the residuals (bottom-left). The remaining plot (bottom-right) is the synthetic signal.

The validation is carried out in analogy to approach 1. Figure 6.25 illustrates the differences between the synthetic output signal and the set of 85 GPS/leveling fitting points (top). The bottom plot is the fitting surface generated from 85 differences above.

After the fitting step, the resulting solution is obtained and displayed in the top of figure 6.26. This geoid solution is complemented by the corresponding error estimates illustrated in the bottom plot. Similar to approach 1, the error model in this approach is also around 3 to 4 cm, except the suddenly changeful values on the South-East border.

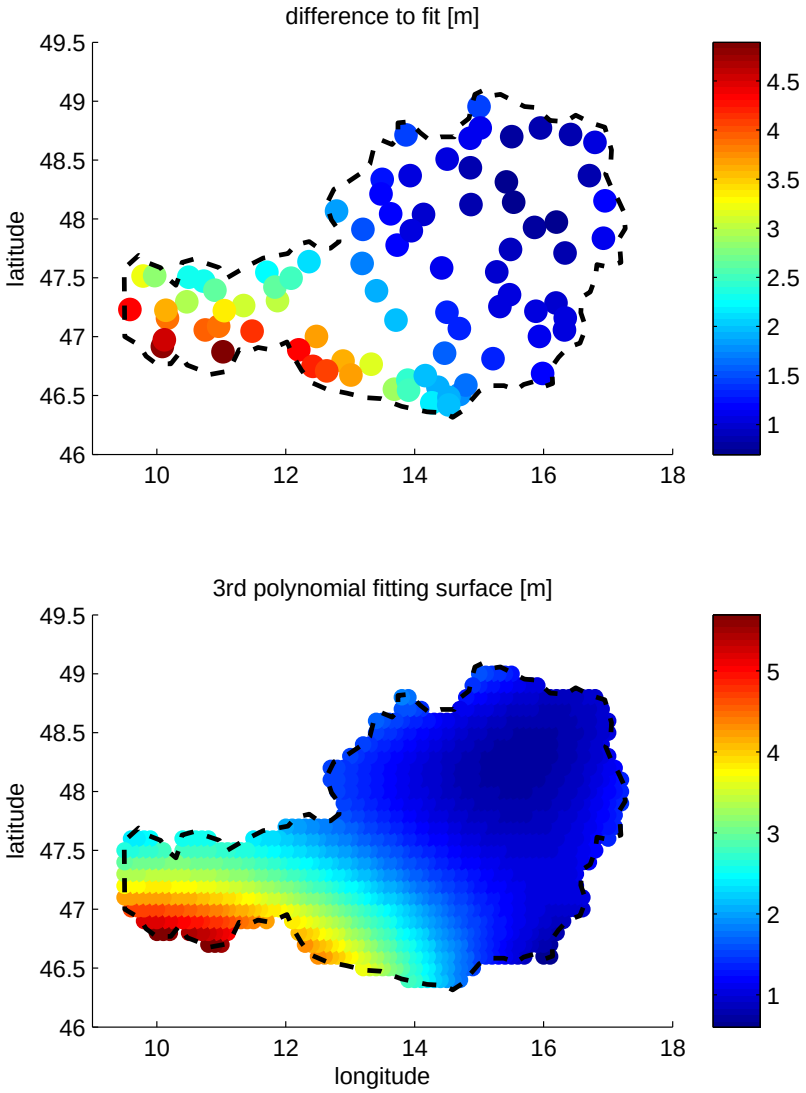

Figure 6.25: Approach 2: differences from 85 GPS/leveling fitting points (top) and the 3^{rd} order polynomial fitting surface (bottom)

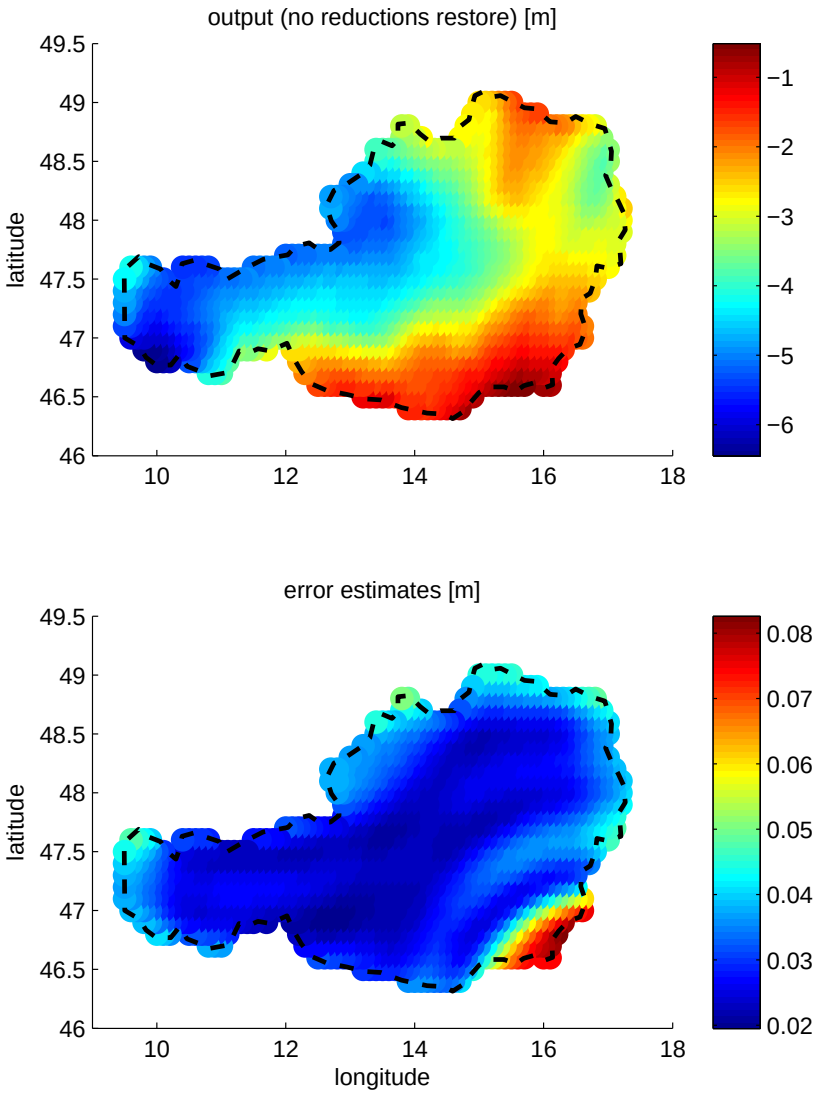

Figure 6.26: Approach 2: the output signal (top) and the error estimates (bottom)

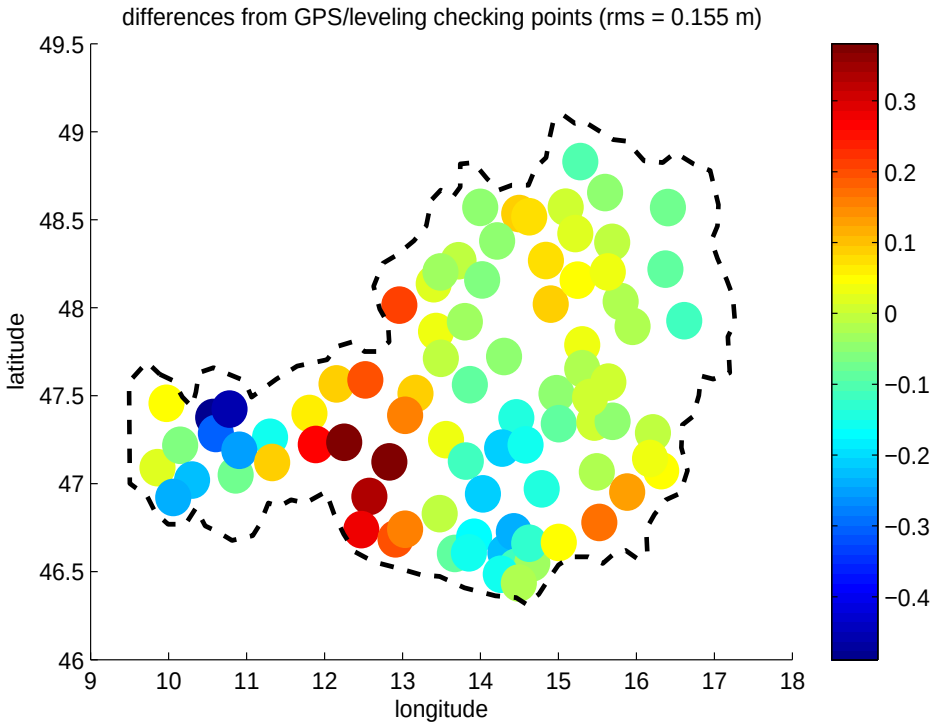

Figure 6.27: Approach 2: differences from 85 GPS/leveling checking points

The evaluation is carried out also using 85 GPS/leveling checking points. Figure 6.27 shows the differences between the final result and the checking data sets. The root mean square values of differences are about 16 cm. It looks like that the addition of GPS/leveling data does not improve the final result. In other words, only using the lower part of the spectrum of the GPS/leveling signal is not an adequate choose. An attempt to use also the higher frequency components of GPS/leveling data will be carried out in next approach.

6.6 Approach 3

As mentioned above, the use of GPS/leveling measurements as an input data source does not give an improvement due to the fact that we only take into account a small part (harmonic D/O 64 to 127) of information which

GPS/leveling data can provide. In this approach, an attempt to use higher frequency components of GPS/leveling data is performed. The global input data set (comprises global model and GPS/leveling data) is analyzed into 10 levels instead of 6 levels as in approach 2. Consequently, we can use GPS/leveling information up to harmonic D/O 2047, with the drawback that the modeled geoidal undulations with their harmonic D/O just up to 127 will be also analyzed up to (high) levels where they have no information. This is obviously an inadequate treatment for the long-wavelength global data, and the final error of this solution is very bad. However, this approach is still presented as a point of view in the attempts of using GPS/leveling measurements as the input data.

In this approach, the input data are absolutely the same as in approach 2 but the data set of geoidal undulations (including the global model EIGEN-GL04S and the GPS/leveling observations) is analyzed into 10 levels (up to harmonic D/O 2047 equivalently), same as for the local data. Thanks to higher levels used to analyze, we can employ the informative signals of the GPS/leveling data also in the high-frequency range. Figure 6.28 shows that the geoidal undulation signals (including GPS/leveling data) now provide not only the detail signal at level 6 (top) but also at higher levels exemplarily represented by level 8 (middle) and the residuals (bottom).

Now the combination is performed for all levels (6 to 10) using the spectral-stochastic weight. The synthetic output signal is displayed in figure 6.29. The validation is carried out in analogy to other approaches and illustrated in figure 6.30 where the top plot is the 85 differences from the GPS/leveling fitting data and the bottom one shows the fitting surface.

After fitting step, the final result of approach 3 is obtained (top plot of figure 6.31). The error estimates in the bottom plot shows that the stochastic error of this approach is around 3 to 4 cm, as same as the previous approaches. However, the evaluation step (figure 6.32) expresses that the actual differences from the checking data jump up to 40 cm. This points out that there must be a systematic problem in the process.

Now we back to the weighting issue of this approach. Every point at each level has a individual weight value thanks to the spectral-stochastic weighting method. In figure 6.33, the weight of local data of every point at levels 6

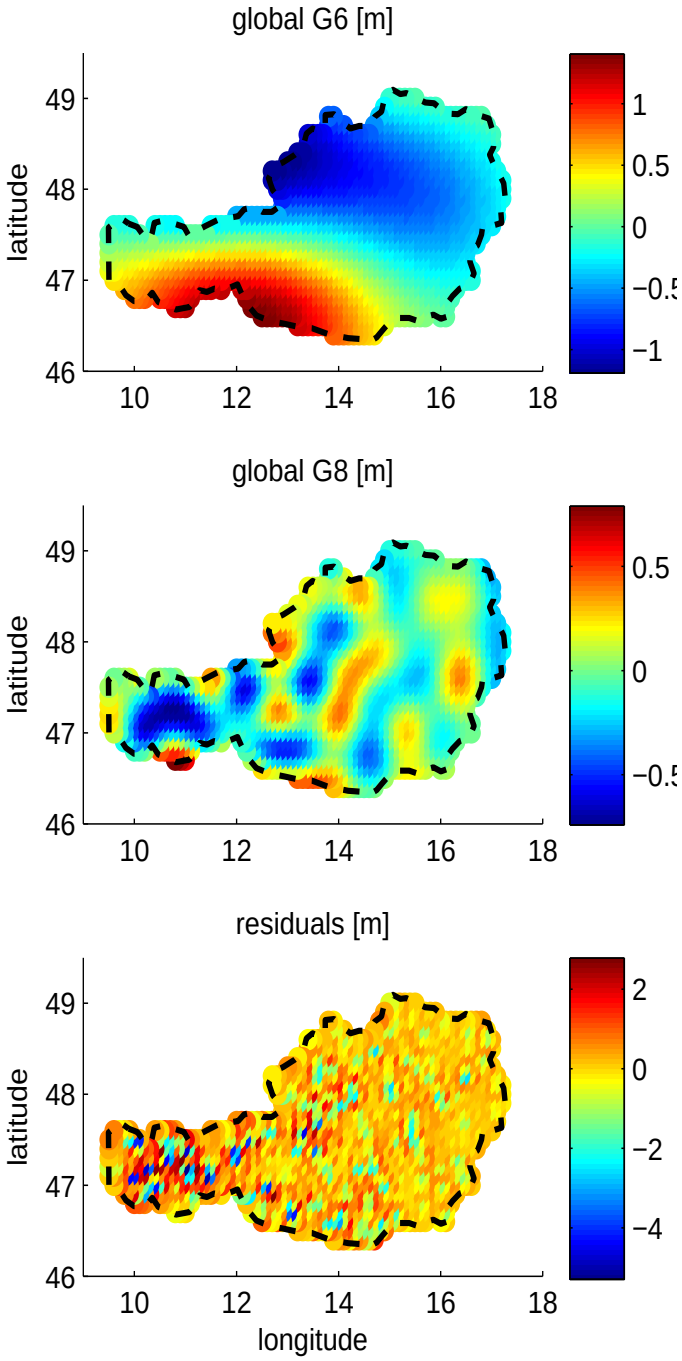

Figure 6.28: Approach 3: Globally detail signals at level 6 (top), level 8 (middle), and the residuals (bottom)

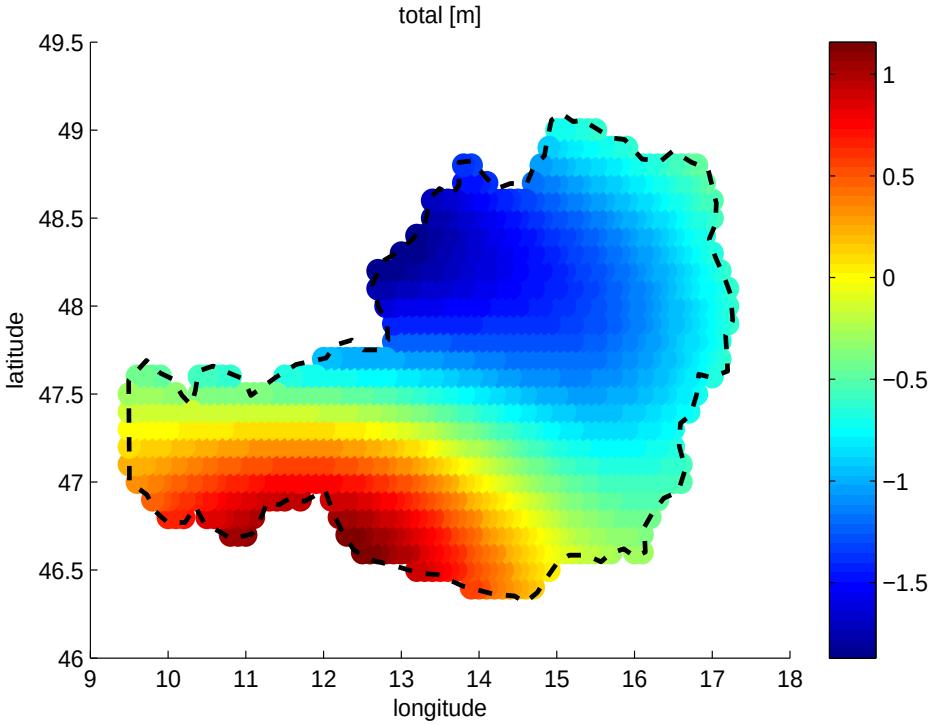

Figure 6.29: Approach 3: The synthetic signal

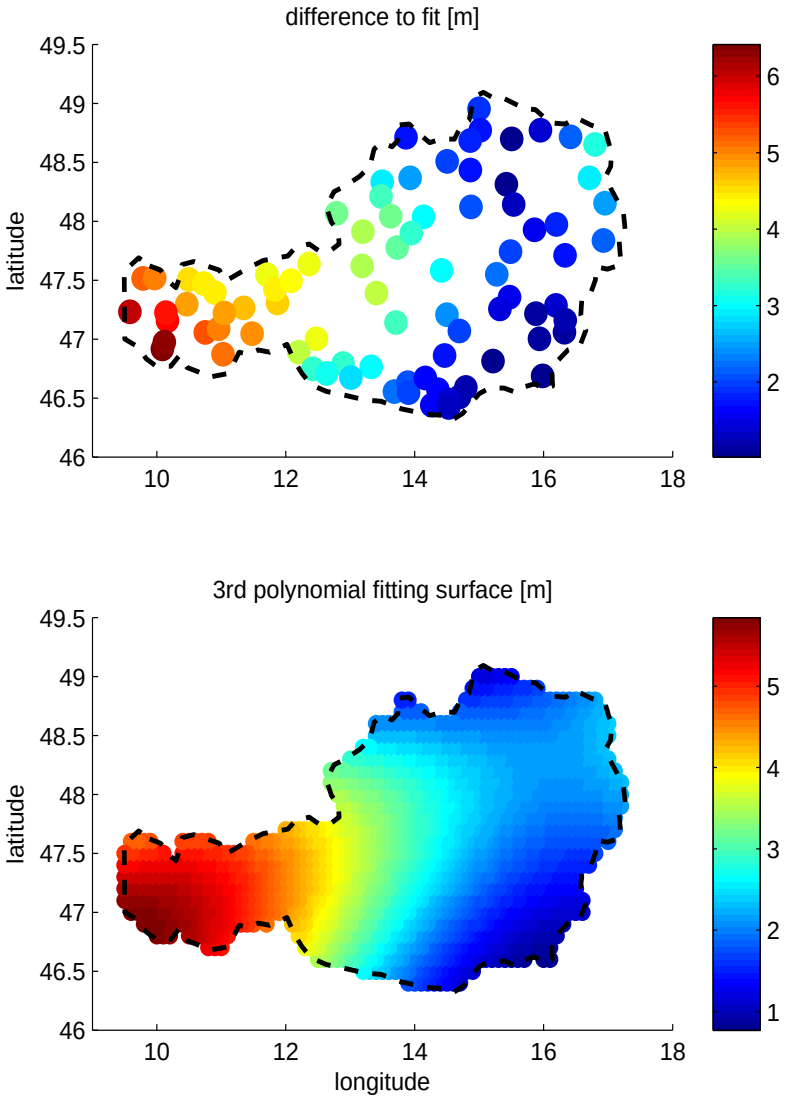

Figure 6.30: Approach 3: differences from 85 GPS/leveling fitting points (top) and the 3^{rd} order polynomial fitting surface (bottom)

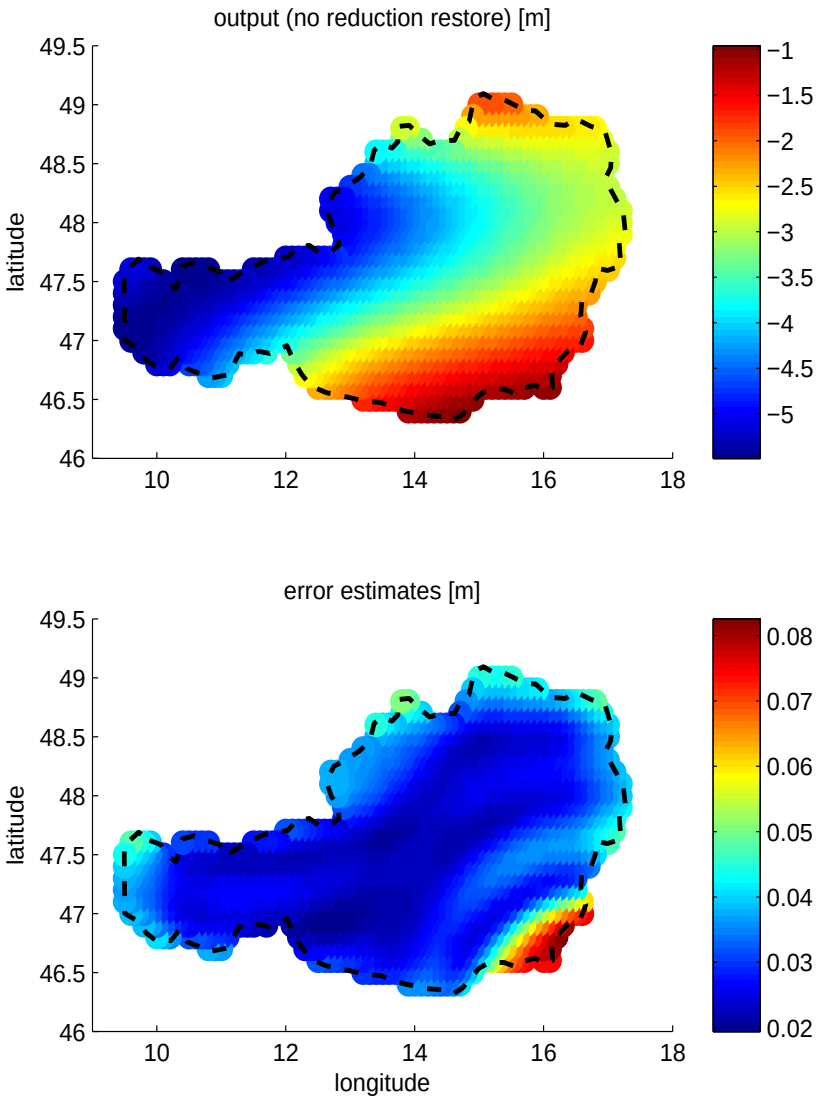

Figure 6.31: Approach 3: the output signal (top) and the error estimates (bottom)

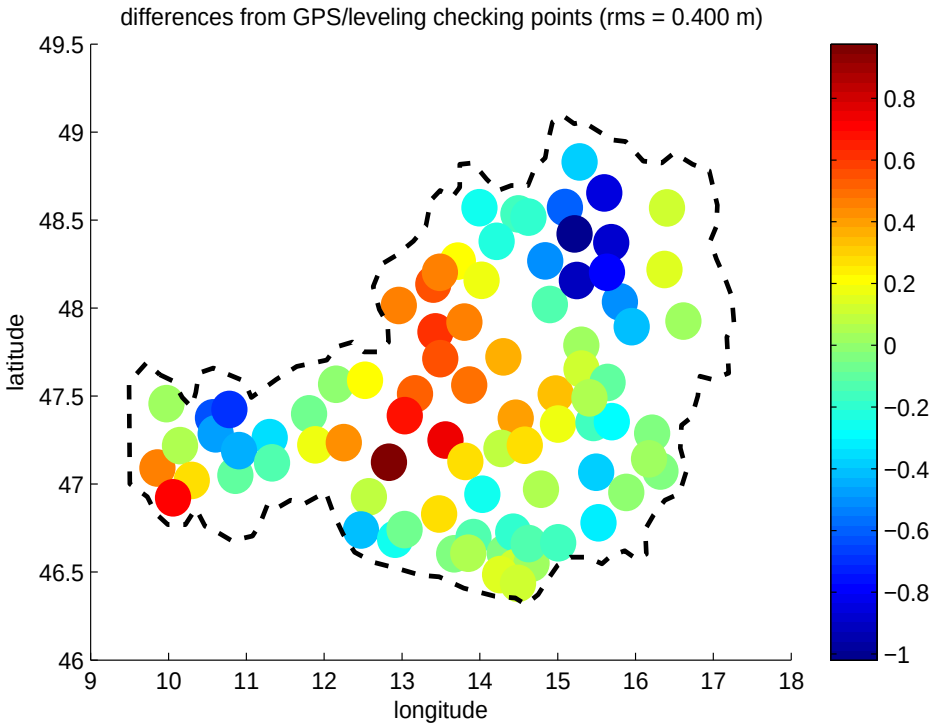

Figure 6.32: Approach 3: differences from 85 GPS/leveling checking points

to 10 is illustrated in the subplots 2 to 6, respectively. Moreover, for estimating the contribution of each component (global or local) of data, the so-called level weight is also computed and displayed in the first subplot. In one hand, the additional use of the higher frequency band of GPS/leveling signals (in comparison with approach 2) gives us more information. In the other hand, due to the much larger contribution of the GPS/leveling data, the weight values of global components also increase. The first plot in figure 6.33 indicates that the dominance of global components is up to level 8. This is computationally reasonable due to the high accuracy of the GPS/leveling data (assumed less than 1 cm), but not realistic in the scheme of the combination between the long-wavelength components of the global data and the short-wavelength component of the local one. In this case, the global data (including GPS/leveling data) are over-weighted and the computational weight matrix is inadequate to apply the combined spectral-stochastic weighting method for the MRA process. A non-weighting combination solution will be presented in the next approach as an alternative solution.

Comparing approaches 1 to 3 to each other, we may conclude that the inadequate inclusion of GPS/leveling measurements in the input data does not improve the final result in case neglecting high-frequency component of GPS/leveling data (approach 2), or even much worse in case ”stretching” long-wavelength component of modeled data into high levels where it has no information (approach 3). For a possible improvement, in the author's opinion, the GPS/leveling measurements should be merged into the much higher resolution modeled data (e.g. the global model EGM2008), and all of them are analyzed up to reasonably high levels. However, it should be considered that, EGM2008 is a composite model (i.e. including terrestrial data by itself), and that how to determine the optimal level used to analyze the mixed GPS/leveling and global modeled data needs to be investigated in detail.

6.7 Approach 4

As mentioned before, this approach is the non-weighting solution of approach 3, or in other words, the weights of the global components are as-

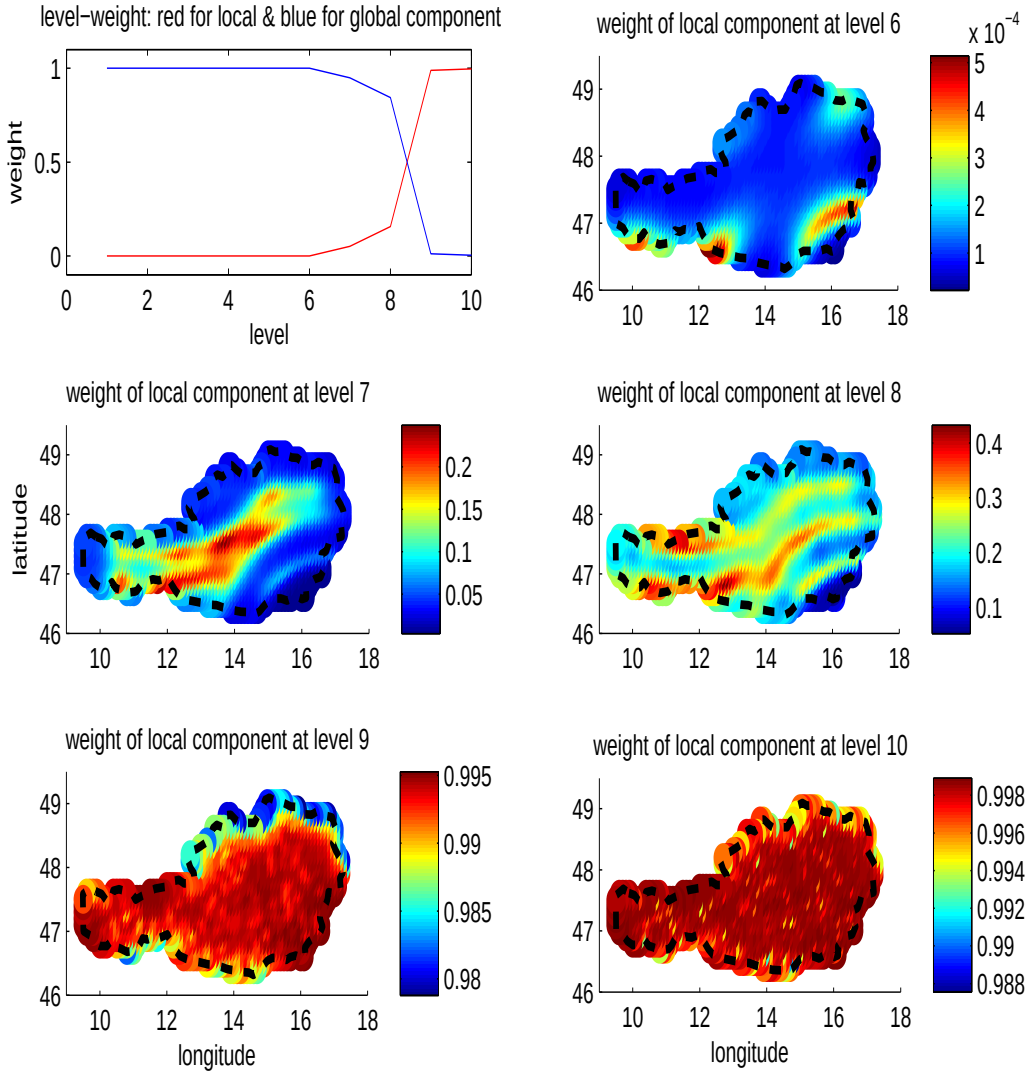

Figure 6.33: Approach 3: level weights of local (red) and global (blue) components (top-left); the rest: point weights of local component at levels 6, 7, 8, 9, 10 (left to right, top to bottom)

signed the value of one for the levels equal and less than 6, and zero for the other levels (zero and one for the local component correspondently). That means the solution here is simply to ignore the weighting matrix and apply the principle that the long-wavelength information is dedicated to the global component and the short-wavelength component is the domain of the local data. Here the border of the global signals is up to level 6, identify to the harmonic D/O 127 of the global geoidal undulation input computed from the model EIGEN-GL04S.

Figure 6.34, 6.35, and 6.36, respectively, illustrate for the validation, the solution, and the evaluation which are performed similarly to the previous approaches. While the error estimates (figure 6.35, bottom plot) are the same as other approaches, the actual error of 17 cm (figure 6.36) is much improved in comparison with the order of 40 cm in approach 3. Although now the contribution of global components is only at level 6 (and shown that it is better than the solution of approach 3), one should remember that the global data are analyzed up to level 10; and this is obviously inadequate for the global model (D/O 127). Therefore, the final result is only better than approach 3, but is still not a reasonable treatment for the issue of including GPS/leveling data in the input data. Summarizing approaches 2, 3, and 4, one can realize that all those attempts still do not appreciably treat the combined input data set (global model and GPS/leveling observations). In approach 2, we neglect the high-frequency component of GPS/leveling data (this data set is already topographic-isostatic reduced but its bandwidth is still far beyond level 6); in approach 3, we ”stretch” the global modeled data to 10 levels and use the global data up to level 10 to combine (with local data), which leads to the over-weight of global components; in approach 4, we use only level 6 of global data to combine, but still use 10 levels to analyze like approach 3. The result is that we obtain a much improved solution in comparison with approach 3 thanks to the elimination of the over-weighting calculation; however, the result is still worse than approaches 1 and 2 because the inadequate analysis for the long-wavelength global model still exists. A possible solution is to use a higher resolution global model which is more consistent with the (reduced) GPS/leveling data from the spectral point of view. The investigation for a practicable solution for this issue should be considered in detail in future

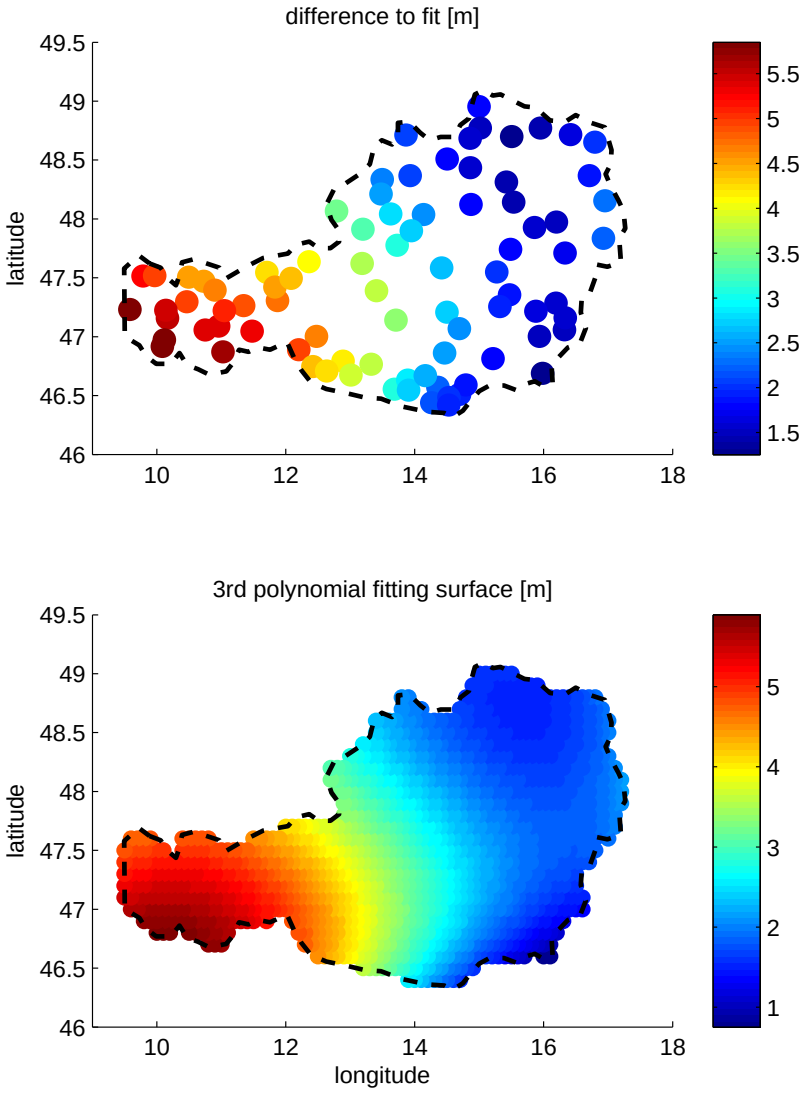

Figure 6.34: Approach 4: differences from 85 GPS/leveling fitting points (top) and the 3^{rd} order polynomial fitting surface (bottom)

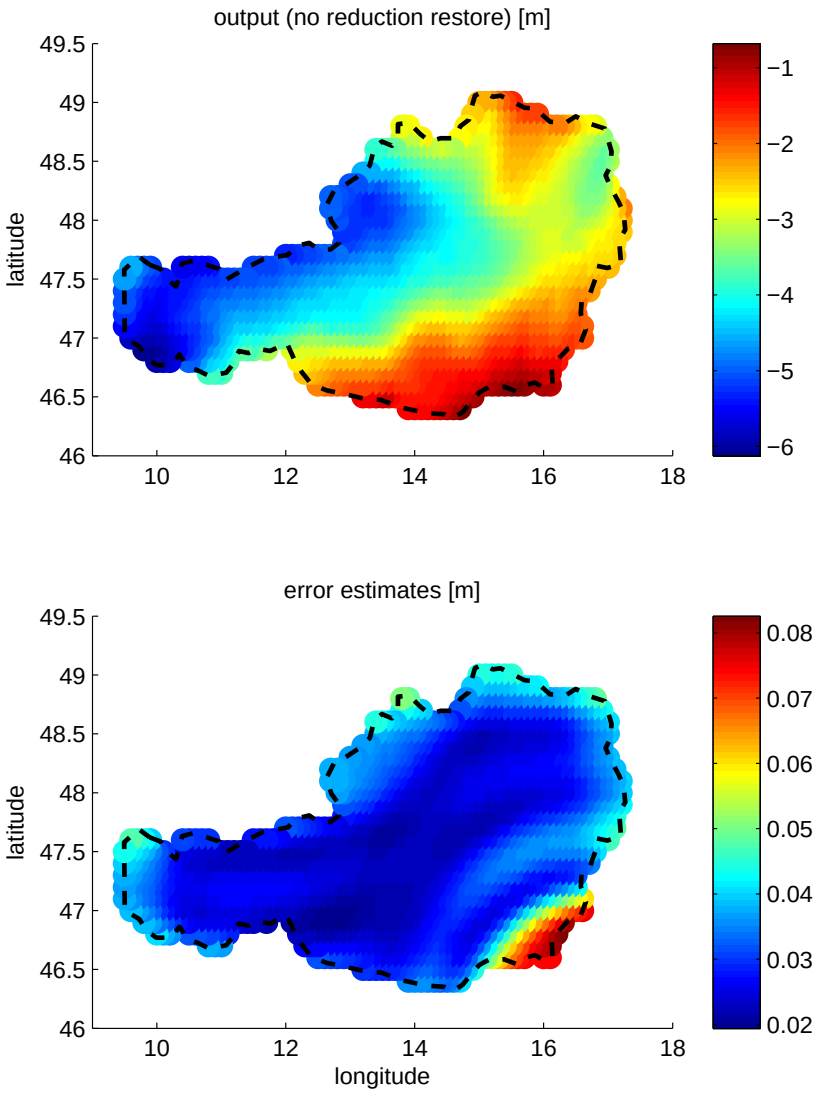

Figure 6.35: Approach 4: the output signal (top) and the error estimates (bottom)

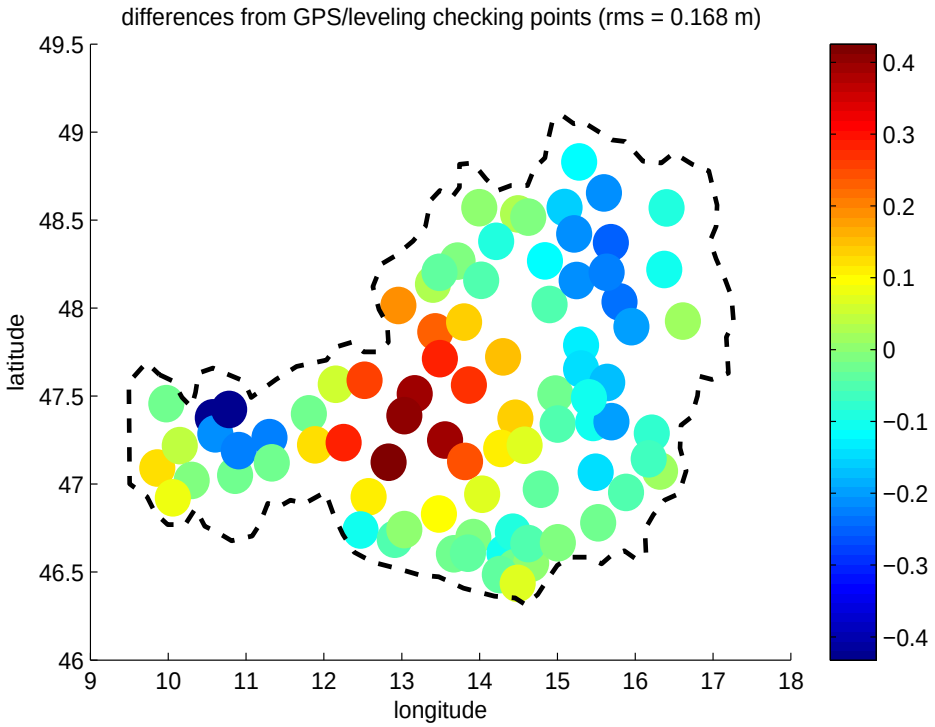

Figure 6.36: Approach 4: differences from 85 GPS/leveling checking points

studies.

6.8 SIMULATION FOR FULL SIGNALS

In principle, MRA can deal with full signals, i.e. non-reduced data. However, using non-reduced data to compute a geoid is not a correct solution due to disregarding masses outside the geoid. In this simulation, the main purpose is the investigation of the behavior of MRA with extremely high-frequency input signals, so the free-air data without topographic reductions are used. One should be aware that this is not a fully correct solution for the geoid determination, at least from a theoretical point of view.

Here, the combined solution using local gravity anomalies and global geoidal undulations is carried out, same as in approach 1. The essential difference between the two approaches is in the input data: there is no reduction here except the global reduction up to D/O 63 due to the limited size of the area.

Local and global input data used in this simulation are illustrated in figures 6.3 and 6.17, respectively. Compared with figure 6.15, figure 6.3 obviously indicates the high-frequency characteristic of non-reduced gravity anomaly data, especially in the mountainous area in south-west Austria.

These data sets are analyzed by the MRA process up to level 10 (harmonic D/O 2047 equivalently). This means that although the local input signals include extremely high frequencies, we just use the frequency range from D/O 64 to D/O 2047 (levels 6, 7, 8, 9, 10) with the local data (and from D/O 64 to D/O 127 with the global data). Note that this limitation means we neglect all signal components higher than harmonic D/O 2047. Apparently, the larger this limit value is, the more information of signal can be taken into account. And theoretically, it can be as high as we design it, as long as the conditions about data sufficiency and grid resolution are still satisfied (c.f. chapter 4 and section 6.2.1 of this chapter).

After several steps including the determination of scale vectors, the analysis, the synthesis, and the validation (figure 6.37), the final result and the error estimates are obtained (figure 6.38). The evaluation (figure 6.39) shows that this approach can give a solution with the error about 19 cm. It is ob-

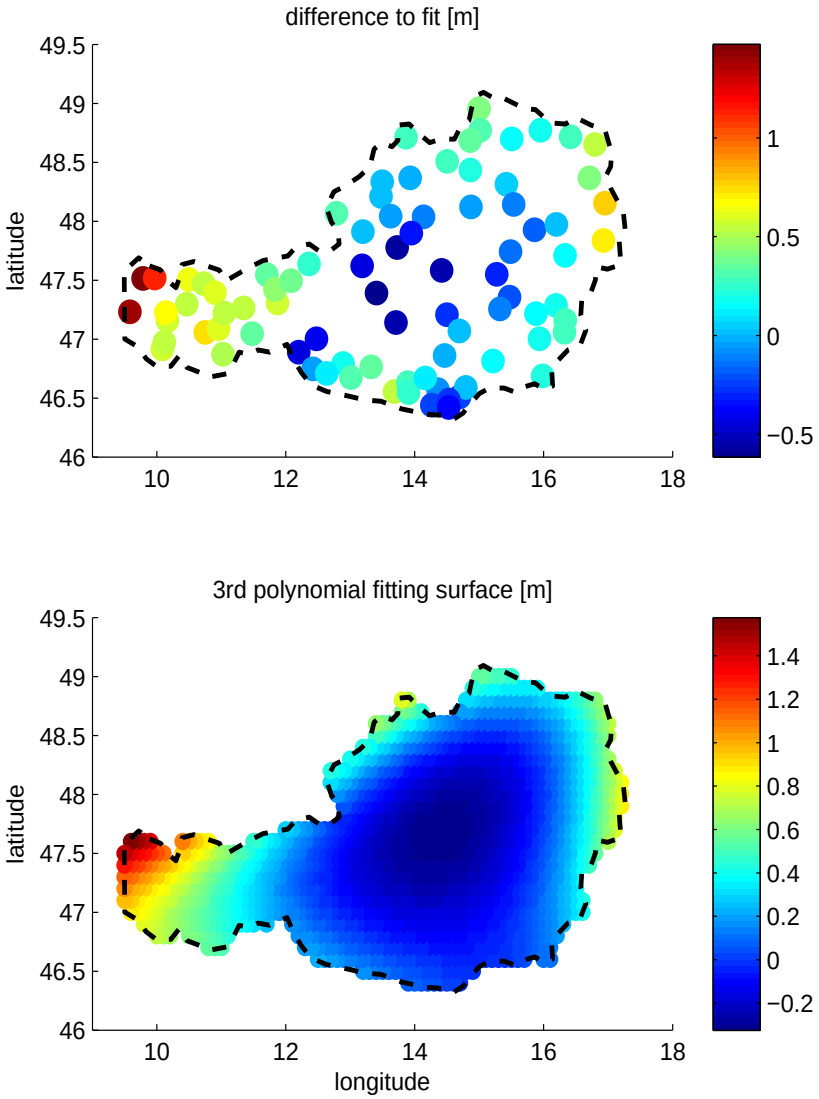

Figure 6.37: Approach 5: differences from 85 GPS/leveling fitting points (top) and the 3^{rd} order polynomial fitting surface (bottom)

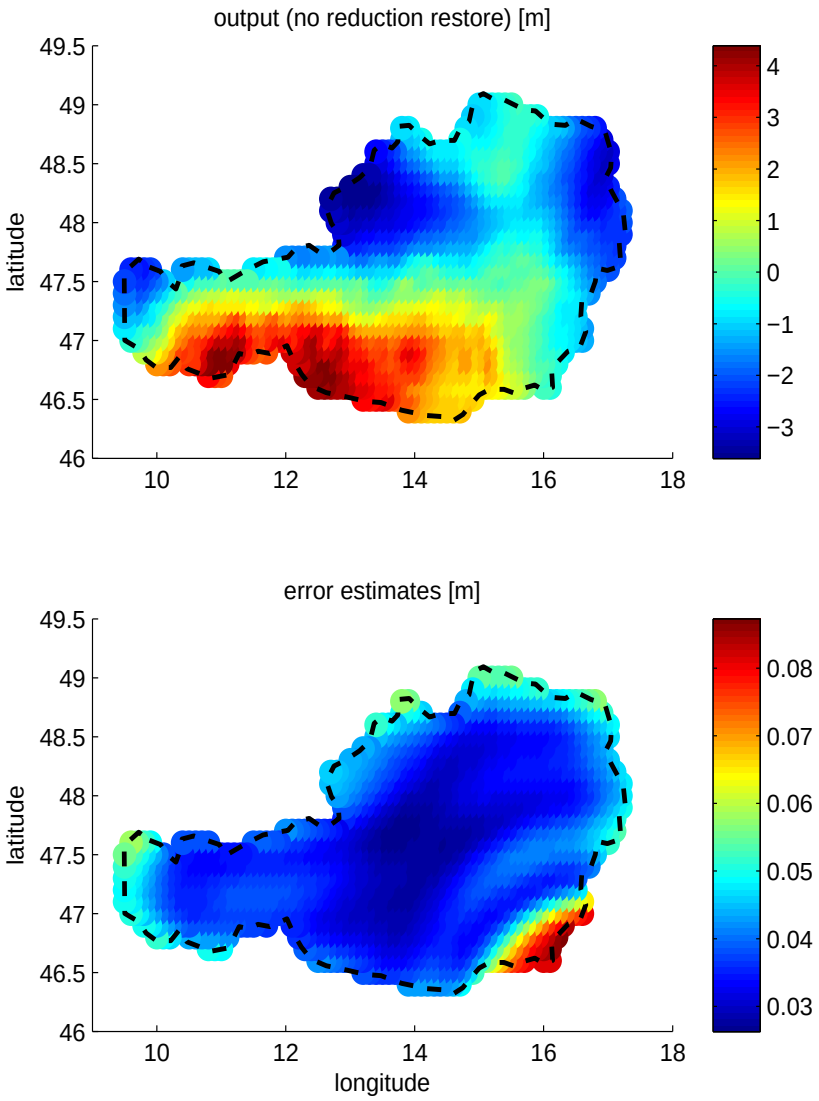

Figure 6.38: Approach 5: the output signal (top) and the error estimates (bottom)

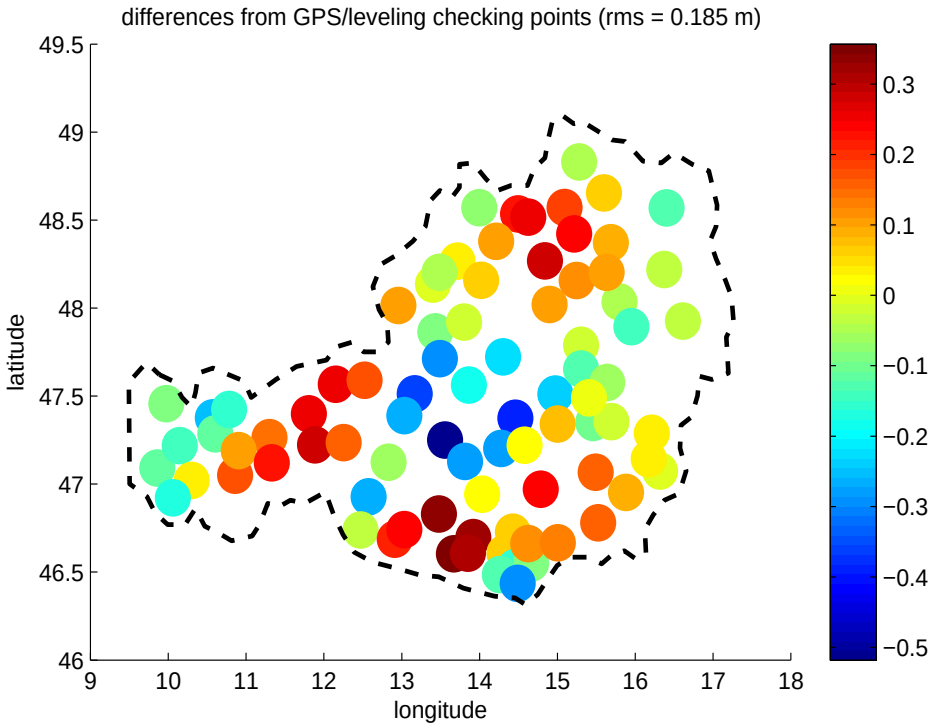

Figure 6.39: Approach 5: differences from 85 GPS/leveling checking points

viously not a good result, but indicates that the MRA process works with extremely high-frequency input signals.

The inconsistency between the output and the references may be attributed to the disregard of masses outside the geoid, the insufficiency of levels used to analyze (10 levels up to D/O 2047 compared with the extremely high-frequency input), and also the error of field transformation at short wavelengths (as in approaches above). The first issue requires an approach that can deal with the masses between the terrain surface and geoid, e.g. the geoid determination from free-air anomalies (in the Molodensky sense) which refer to ground level, through the quasi-geoid and the correction terms for the difference between geoidal undulations and height anomalies (Hofmann-Wellenhof and Moritz 2005). The second issue cannot be completely satisfied from the theoretical point of view due to the infinitely high-frequency characteristic of the terrestrial observables. In practice, the higher level, the better result; however, it strongly depends on the density of terrestrial observables and the computational effort one can manage. The third issue is the same problem for all approaches here. A solution for it may be a formulated harmonic function which has almost zero gravity anomaly values over the target area, and one can use its corresponding values of geoidal undulations as the compensator for the error of the Δg-to-N transformation (Prutkin and Klees 2008, c.f. section 6.2); or simpler, we may apply an appropriate threshold to the scaling process (represented by the matrix K_{rep}) for an expectation of reducing noises.

6.9 SUMMARY

An attempt for the regional geoid solution using the MRA process has been done. Five approaches in this chapter can be classified into three groups: approach 1 uses reduced input data excluding GPS/leveling measurements; approaches 2, 3, and 4 use reduced input data including GPS/leveling measurements; and a simulation (approach 5) use non-reduced data (c.f. table 6.4). They figure out that the MRA process works with real data (which were used in GEOnAUT), and even can deal with the full signals (i.e., non-reduced signals) of input data.

Table 6.5: Summary of results

Approach	Error estimates (cm)	Difference with GPS/leveling data (cm)	Difference with GEOnAUT (cm)
1	5.6	11.8	11.4
2	5.0	15.5	14.8
3	5.0	40.0	41.2
4	5.0	16.8	16.7
5	5.6	18.5	19.3

Table 6.5 summarizes the results. Column 2 points out that the error estimates of the MRA process is few centimeters. Approaches 2, 3, and 4 are a bit better than approaches 1 and 5 thanks to the contribution of the GPS/leveling data (5.0 cm vs. 5.6 cm). Figures 6.21, 6.26, 6.31, 6.35, 6.38 also show the distribution of the error estimates, which the worst values gather on the border (especially at the South-East), the remaining values are just around 3 or 4 cm.

While the estimated errors are computationally about few centimeters, the actual errors in evaluations show that the accuracy of MRA process in this thesis is limited at the order of decimeter. Column 3 of table 6.5 points out that even in the best case, i.e. the solution of approach 1, the error is 12 cm. It can be explained by the inadequate performance of the field transformation (in the scene of the MRA process) at short wavelengths due to the fact that, firstly, MRA process works perfectly in the example of section 2.8 where the Δg-to-N transformation is performed at long wavelengths (D/O up to 10), and secondly, it also works well in the simulation at section 6.2.1 where the gravity anomaly quantity Δg is reconstructed using 10 levels (the neglect of higher frequencies causes an error of 2.3 mGal by itself as pointed out in that simulation).

The attempt to use the GPS/leveling data as an input data source in approaches 2, 3, and 4 expresses that they can improve the estimated error

but not the actual error because of the inadequate inclusion of GPS/leveling measurements in the input data. In approach 2, the use of only low frequency part of GPS/leveling data does not give an improvement. In approach 3, an attempt to use higher frequency components of GPS/leveling data is performed. The global input data set (comprises global model and GPS/leveling data) is analyzed into 10 levels instead of 6 levels as in approach 2. Consequently, we can use GPS/leveling information up to harmonic D/O 2047, with the drawback that the modeled geoidal undulations with their harmonic D/O just up to 127 will be also analyzed up to (high) levels where they have no information. This is an inadequate treatment for the long-wavelength global data leading to the over-weighting problem for global components. To solve this problem, a non-weighting solution is performed in approach 4. The global data are still analyzed up to level 10 but only used 6 levels, i.e. the global model (D/O 127) are still stretching" into high levels where it has no information, but these signals (in high levels) are not used. In others words, the solution here is simply to ignore the weighting matrix and apply the principle that the long-wavelength information is dedicated to the global component and the short-wavelength component is the domain of the local data. However, the result is still not better than the solution without GPS/leveling data due to the fact that the unreasonable analysis still exist. In conclusion, the combination of the global model with GPS/leveling in the geoidal undulations of input data is still not completely reasonably treated due to the un-correspondence about the spectrum and density of data points of two data sources. For a possible improvement, in the author's opinion, the GPS/leveling measurements should be merged into the much higher resolution modeled data (e.g. the global model EGM2008), and all of them are analyzed up to reasonably high levels. However, it should be considered that, EGM2008 is a composite model (i.e. including terrestrial data by itself), and that how to determine the optimal level used to analyze the mixed GPS/leveling and global modeled data needs to be investigated in detail.

Approach 5 is an attempt to investigate the competence of MRA in dealing with extremely high frequencies when using non-reduced data. The error about 19 cm is not a good result but at least indicates that the MRA

process works with very high-frequency signals. The inconsistency between the output and the references may be attributed to the disregard of masses outside the geoid, the insufficiency of levels used to analyze (10 levels up to D/O 2047 compared with the extremely high-frequency input), and also the error of field transformation at short wavelengths (as in approaches above). The first issue requires an approach that can deal with the masses between the terrain surface and geoid, e.g. the geoid determination from free-air anomalies (in the Molodensky sense) which refer to ground level, through the quasi-geoid and the correction terms for the difference between geoidal undulations and height anomalies (Hofmann-Wellenhof and Moritz 2005). The second issue cannot be completely satisfied from the theoretical point of view due to the infinitely high-frequency characteristic of the terrestrial observables. In practice, the higher level, the better result; however, it strongly depends on the density of terrestrial observables and the computational effort one can manage. The third issue is the same problem for all approaches here. A solution for it may be a formulated harmonic function which has almost zero gravity anomaly values over the target area, and one can use its corresponding values of geoidal undulations as the compensator for the error of the Δg-to-N transformation (Prutkin and Klees 2008, c.f. section 6.2); or simpler, we may apply an appropriate threshold to the scaling process (represented by the matrix K_{rep}) for an expectation of reducing noises.

As mentioned before, the MRA process in this thesis uses the same data sources with project GEOnAUT which applies the LSC method to determine the Austrian geoid with the accuracy of 2 to 3 cm. So this is also a very good reference for all approaches in this thesis beside the evaluations using the data set of GPS/leveling checking points which are carried out in each approach. The last column of table 6.5 indicates that the differences between approaches and GEOnAUT are almost the same the evaluations using GPS/leveling checking data. Moreover, figure 6.40 gives a visual comparison between approaches and GEOnAUT.

Except approach 3 whose difference is very large, other ones including approaches 1, 2, 4 are compared with GEOnAUT before restoring reductions (left to right, top and middle line of figure 6.40), and approach 5, after restoring the global reduction, is compared with the final solution of GEOnAUT

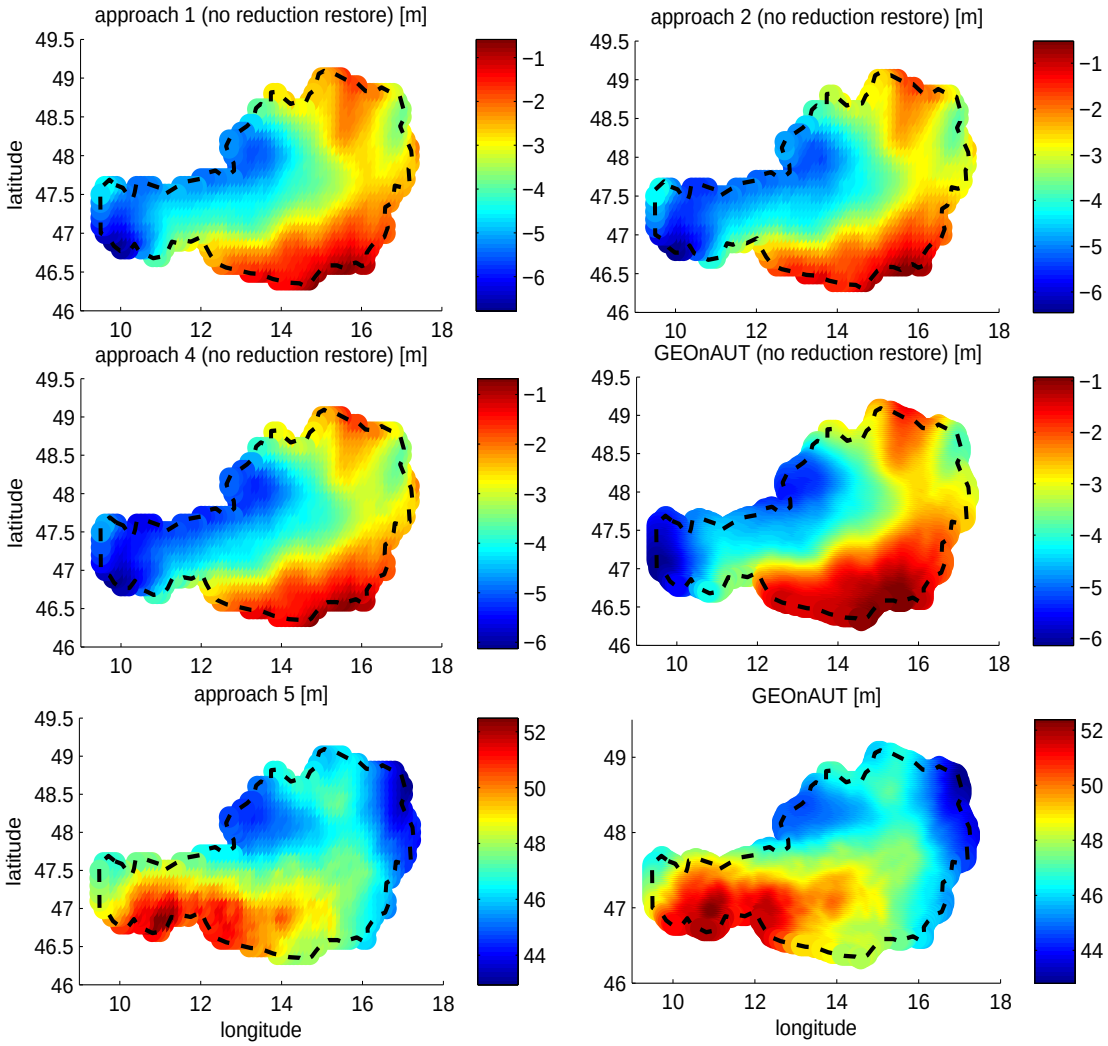

Figure 6.40: Left to right, top to bottom: approach 1, approach 2, approach 4, GEOnAUT without restore, approach 5, GEOnAUT

(bottom line of figure 6.40). In general, the differences almost cannot be graphically recognized. Numerically, they are expressed in the last column of table 6.5.

Both of the evaluation and the comparison with GEOnAUT give almost the same result indicating that the MRA process in this thesis is limited at the accuracy of decimeter, and, in the present state, is still not mature enough to being the alternative for the LSC method in the problem of centimeter-accuracy geoid determination. For improving the MRA result, some main issues should be considered, that include the field transformation in high frequencies, the proper treatment for input data sources having different data types and resolutions, and the use of higher levels which also depends on the density of input data. The possible solutions for these issues are mentioned in the frame of the discussion of the individual approaches in this chapter, and will be summarized in the outlook part of the next chapter.

CHAPTER 7

SUMMARY

For the purpose of (regional) combined gravity field modeling, the thesis presents a solution based on wavelets-MRA process using as the spherical base function a so-called unique reproducing kernel (chapter 2). This solution combines the global data (EGMs) and the terrestrial observations; i.e. makes benefit of the advantage of the global component in long wavelengths and the local component in short wavelengths; and a combination is performed in the buffer area between them. The combination uses the spectral-stochastic weighting method which itself is a combination of the spectral weight based on the data spectrum (or, in other words, the harmonic degrees and orders), and the stochastic weight based on the stochastic information of the input data. This combined weight guarantees the spectral principle that the main contribution of global data is in the low frequencies, and the high frequencies are dominated by the local observables, as well as the propagation of stochastic information for the final error estimation (chapter 5). In principle, a combined solution can be made for any type of input data sources; however, due to the limited availability of data, only two main types of data, the global geoidal undulations and the terrestrial gravity anomalies were used in the case study for the Austrian territory; besides, an attempt to take the GPS/leveling data into account as an input data source is also presented in chapter 6.

Beside the weighting method which is the main issue for the data com-

bination, the other key in the practical aspect is regularization. Tikhonov regularization including several methods for choosing the regularization parameter is presented in chapter 3. Among them, the quasi-optimality method is chosen for the implementation in chapter 6. Moreover, chapter 4 deals with the grid configuration; based on it, the choice for equiangular grids with appropriate resolutions is used in the numerical study.

After several simulations as well as the implementation using real data presented in this thesis, some conclusions can be extracted as below:

- The MRA process works with real data, and even can deal with the full signals (non-reduced data); the final result is complemented by the error estimates. The spectral-stochastic weighting scheme ensures the adequate contribution of global and local data in different frequency ranges as well as takes all stochastic information of input data into account.

- Tikhonov regularization is sufficient for the gravity field modeling here. The recommended method for the regularization parameter choice is the Quasi-optimality; besides, a multiple-parameter method called Generalized Bias Estimation (GBE) is also helpful.

- The equiangular grid still works well for the latitudes of Austria in the scene of the MRA process. The grid size and resolution have to satisfy for an adequate representation of the signal wavelengths as well as be large enough for solving the parameters of the scale coefficient vector.

- In the case study for Austria, five approaches in chapter 6 using reduced data excluding GPS/leveling measurements (approach 1), reduced data including GPS/leveling measurements (approaches 2, 3, and 4), and non-reduced data (approach 5) figure out that the MRA process in the present state of this thesis can provide a regional combined geoid solution with the accuracy of decimeter. It is not mature enough for a centimeter-accuracy regional geoid solution. The simplicity of this MRA process (in comparison with the standard method LSC) reduces the computational effort; however, it seems to be not fine enough for

a highly accuracy result, e.g. the field transformation may require a more precise treatment, especially at high-frequency ranges.

In conclusion, concerning the new aspect of this thesis, a data combination using the proposed spectral-stochastic weighting method in the scene of MRA is performed successfully. This MRA process is applied to real data of Austria for a geoid solution. In principle, the MRA process with a simple computation scheme works correctly, but requires improvements for a better result.

The essential improvement may be obtained by reducing the (high-frequency characteristic) error of the field transformation at short wavelengths. For this, a threshold applying to the kernel function to filter these high-frequency noises may be a simply practicable candidate. Besides, the number of levels used to analyze should be increased. This is strongly dependent on the density of terrestrial data and the computational effort one can handle. These issues should be the first consideration of future studies for a key improvement.

The next promising continuation likely is a full MRA process which takes all advantages of the multi-resolution representation into account. However, this will increase the computation steps (for multi base grids) as well as require an appropriate weighting scheme for uniting the multi-resolution representations to a unique output. In addition, one practical issue which can be investigated and improved is a solution for the problem of the inconsistent frequency ranges of input data sources. A satisfactory answer for this problem will be very practically helpful in the use of all data sources. One simple solution may be the use of higher resolution global model, such as EGM2008, or the results from the GOCE mission (c.f. section 6.6).

Besides, other additional issues also should be considered such as the investigation for other kernels (Blackman, Bernstein, etc.) which in principle are more flexible than the Shannon function used in this thesis. An other issue which is also very interesting (and mathematically demanding) is a formulated model for the field-transformation correction whose idea was introduced in sections 2.3 and 6.2.3.

REFERENCES

[1] Bauer F, Mathe P, Pereverzev S (2007) Local solutions to inverse problems in geodesy. J Geodesy 81: 39-51

[2] Bouman J (2000) Quality assessment of satellite-based global gravity field models. Publications on Geodesy 48, Netherlands Geodetic Commission, Delft

[3] Cui J (1995) Finite pointset methods on the sphere and their application in physical geodesy. PhD thesis, University of Kaiserslautern

[4] de Bruijne AJT, Haagmans RHN, de Min EJ (1997) A preliminary North Sea Geoid model GEONZ97. Rep MDGAP-9735, Directoraat-Generaal Rijkswaterstaat, Meetkundige Dienst, Delft

[5] Drinkwater MR, R. Floberhagen R, Haagmans R, Muzi D, Popescu A (2003) GOCE: ESA's first Earth Explorer Core mission. Space Science Series of ISSI 18: 419-432

[6] Driscoll JR, Healey DM (1994) Computing Fourier Transforms and Convolutions on the 2-Sphere. Advances in Applied Mathematics 15: 202-250.

[7] Eicker A (2008) Gravity field refinement by radial basis functions from in-situ satellite data. Dissertation, Bonn University

[8] ESA (1999) Gravity field and steady-state ocean circulation mission. Report for mission selection, SP-1233(1). European Space Agency Publications Division, Noordwijk

[9] Featherstone WE (2000) Refinement of a gravimetric geoid using GPS and levelling data. J Surv Eng 126: 27-56

[10] Fehlinger T, Freeden W, Mayer C, Schreiner M (2010) On the local multiscale determination of the Earths disturbing potential from discrete deflections of the vertical. Computational Geosciences 12: 473-490

[11] Fengler MJ, Freeden W, Gutting M (2004) Multiscale modeling from EIGEN-1S, EIGEN-2, EIGEN-GRACE01S, GGM01, UCPH2002-0.5, EGM96. 2nd International GOCE user workshop, Frascati, Italy

[12] Fengler MJ, Freeden W, Gutting M (2005) The spherical Bernstein wavelet. Schriften zur Funktionalanalysis und Geomathematik, 20, University of Kaiserslautern, Mathematics Department, Geomathematics Group

[13] Fengler MJ, Freeden W, Kohlhaas A, Michel V, Peters T (2007) Wavelet modelling of regional and temporal variations of the Earth's gravitational potential observed by GRACE. J Geodesy 81: 5-15

[14] Flechtner F (2005) AOD1B Product Description Document. Technical Report GRACE 327-750, Jet Propulsion Labratory

[15] Fotopoulos G (2005) Calibration of geoid error models via a combined adjustment of ellipsoidal, orthometric and gravimetric geoid height data. J Geodesy 79: 111-123

[16] Freeden W, Gervens T, Schreiner M (1998) Constructive approximation on the sphere (with applications to geomathematics). Clarendon Press, Oxford

[17] Freeden W (1999) Multiscale modelling of spaceborne geodata. Teubner, Stuttgart

[18] Freeden W, Groten E, Michel V, Arfa-Kaboodvand K (2003) Geopotential reconstruction, decomposition, fast computation, and noise cancellation by harmonic wavelets. Stud Geophys Geod 47: 37-72

[19] Freeden W, Michel D, Michel V (2004) Multiscale modeling of ocean circulation. 2nd International GOCE user workshop, Frascati, Italy

[20] Freeden W, Fehlinger T, Klug M, Mathar D, Wolf K (2009) Classical globally reflected gravity field determination in modern locally oriented multiscale framework. J Geodesy 83: 1171-1191

[21] Grebenitcharsky RS, Rangelova EV, Sideris MG (2005) Transformation between gravimetric and GPS/levelling-derived geoids using additional gravity information. J Geodynamics 39: 527-544

[22] Hansen P (1997) Regularization tools, a MATLAB package for analysis and solution of discrete ill-posed problems. Version 2.1 for MATLAB 5.0. Department of Mathematical Modeling, Technical University of Denmark

[23] Hansen P (1992) Analysis of discrete ill-posed problems by means of L-curve. SIAM Review 34(4): 561-580

[24] Hofmann-Wellenhof B, Moritz H (2005) Physical geodesy. Springer, Wien

[25] Holschneider M, Chambodut A, Mandea M (2003) From global to regional analysis of the magnetic field on the sphere using wavelet frames. Physics of the Earth and Planetary Interiors 135: 107-124

[26] Ivanov V (1962) Integral equation of the first kind and an approximate solution for the inverse problem of potential. Soviet Math Doklady 3: 210-212

[27] Jaeger R (1999) State of the art and present developments of a general concept for GPS-based height determination. In: Lilje M (ed) Proc of the symposium geodesy and surveying in the future the importance of heights, Sweden

[28] Keller W (Ed) (2004) Wavelets in Geodesy and Geodynamics. Walter de Gruyter, Berlin

[29] Kern M, Schwarz KP, Sneeuw N (2003) A study on the combination of satellite, airborne, and terrestrial gravity data. J Geodesy 77: 217-225

[30] Klees R, Ditmar P, Broersen P (2003) How to handle colored observation noise in large least-square problems. J Geodesy 76: 629-640

[31] Koch KR, Kusche J (2002) Regularization of geopotential determination from satellite data by variance components. J Geodesy 76: 259-268

[32] Kuehtreiber N (2002) High Precision Geoid Determination for Austria. Habilitation, Graz University of Technology, Graz

[33] Kusche J, Klees R (2002) Regularization of gravity field estimation from satellite gravity gradients. J Geodesy 76: 359-368

[34] Lemoine FG, Kenyon SC, Factor JK, Trimmer RG, Pavlis NK, Chinn DS, Cox CM, Klosko SM, Luthcke SB, Torrence MH, Wang YM, Williamson PG, Pavlis EC, Rapp RH, Olson TR (1998) The development of the Joint NASA GSFC and the National Imagery and Mapping Agency (NIMA) Geopotential Model EGM96. National Aeronautics and Space Administration, Goddard Space Flight Center, Maryland

[35] Luong BB (2009) Regularization methods and the application into MRA process. Conference for science and technology 11, HCM University of technology, Vietnam

[36] Lysaker DI, Omang OCD, Petterson BR, Solheim D (2007) Quasigeoid evaluation with improved levelled height data for Norway. J Geodesy 81: 617-627

[37] Mallat S (1998) A wavelet tour of signal processing (2nd edition). Academic Press, San Diego

[38] Marchenko AN (1998) Parameterization of the Earth's gravity field - Point and line singularities. Lvis Astronomical and Geodetic Society, Lvis

[39] Marquardt WD, Snee RD (1975) Ridge regression in practice. Am Stat 29: 3-20

[40] Moritz H (1989) Advanced physical geodesy (2. ed.). Wichmann, Karlsruhe

[41] Morozov V (1984) Methods for solving incorrectly posed problems. Springer New York, Berlin, Heidelberg

[42] Nahavandchi N, Soltanpour (2006) Improved determination of heights using a conversion surface by combining gravimetric quasi-geoid/geoid and GPS-levelling height differences. Stud Geophsy Geod 50: 165-180

[43] Pail R (2006) The Austrian Geoid 2007 (GEOnAUT), Midterm report. Graz University of Technology, Graz

[44] Pail R (2007) The Austrian Geoid 2007 (GEOnAUT), Final report. Graz University of Technology, Graz

[45] Pail R (2007) Geophysics and Geodynamics, Lecture note. Graz University of Technology, Graz

[46] Pail R, Kuehtreiber N, Wiesenhofer B, Hofmann-Wellenhof B, Of G, Steinbach O, Hoeggerl N, Imrek E, Ruess D, Ullrich C (2008) The Austrian Geoid 2007. VGI-Oesterr. Zeitschrift fur Vermessung und Geoinformation, 96, Heft 1/2008, 3-14

[47] Pavlis NK, Holmes SA, Kenyon SC, Factor JK (2008) An Earth Gravitational Model to degree 2160: EGM2008. EGU General Assembly 2008. Vienna, Austria, April 13-18, 2008

[48] Prutkin I, Klees R (2008) On the non-uniqueness of local quasi-geoids computed from terrestrial gravity anomalies. J Geodesy 82: 147-156

[49] Sanso F, Tscherning CC (2003) Fast spherical collocation: theory and examples. J Geodesy 77: 101-112

[50] Schaffrin B (2008) Minimum mean square error (MSE) adjustment and the optimal Tykhonov-Phillips regularization parameter via reproducing best invariant quadratic uniformly unbiased estimates (repro-BIQUUE). J Geodesy 82: 113-121

[51] Schmidt M, Kusche J, van Loon JP, Shum CK, Han SC, Fabert O (2005) Multiresolution representation of a regional geoid from satellite and terrestrial gravity data. In: Jekelis C, Bastos L and Fernandes J (Eds.), Gravity, Geoid and Space Missions. Springer, 167-172

[52] Schmidt M, Fengler M, Mayer-Guerr T, Eicker A, Kusche J, Sanchez L, Han SC (2007) Regional gravity modeling in terms of spherical base functions. J Geodesy 81: 17-38

[53] Sjoberg LE (2005) A discussion on the approximations made in the practical implementation of the remove-compute-restore technique in regional geoid modelling. J Geodesy 78: 645-653

[54] Tapley BD,Bettadpur S, Watkins M, Reigber C (2004) The gravity recovery and climate experiment: mission overview and early results. Geophys Res Lett 31

[55] Tikhonov AN, Arsenin VY (1977) Solutions of ill-posed problems. Wiley, Newyork

[56] Torge W (1989) Gravimetry. Walter de Gruyter, Berlin, New York

[57] Torge W (2001) Geodesy (3ed). Walter de Gruyter, Berlin, New York

[58] Tscherning CC, Rapp RH (1974) Closed covariance expressions for gravity anomalies, geoid undulations, and deflections of the vertical implied by anomaly degree variance models. Report, OSU, Ohio

[59] Wahba G (1990) Spline models for observational data. SIAM

[60] Wittwer T (2009) Regional gravity field modelling with radial basis functions. Publications on Geodesy 72, Netherlands Geodetic Commission, Delft

[61] Xu PL, Rummel R (1994) A generalized ridge regression method with applications in determination of potential fields. Manuscripta Geodetica 20: 8-20

[62] Xu P (1998) Truncated SDV methods for linear discrete ill-posed problems. Geophysical J Int 135: 505-514

[63] Xu P, Fukuda Y, Liu Y (2006) Multiple parameter regularization: numerical solutions and applications to the determination of geopotential from precise satellite orbits. J Geodesy 80: 17-27

[64] Xu P, Shen Y, Fukuda Y, Liu Y (2006) Variance component estimation in linear inverse ill-posed models. J Geodesy 80: 69-81

LIST OF FIGURES

LIST OF TABLES